UNIVERSITY OF OKLAHOMA
GRADUATE COLLEGE

DESIGN AND IMPLEMENTATION OF A NOVEL MULTICOPTER UNMANNED AIRCRAFT SYSTEM FOR QUANTITATIVE STUDIES OF THE ATMOSPHERE

A DISSERTATION
SUBMITTED TO THE GRADUATE FACULTY
in partial fulfillment of the requirements for the
Degree of
DOCTOR OF PHILOSOPHY

By

ANTONIO R. SEGALÉS ESPINOSA
Norman, Oklahoma
2022

DESIGN AND IMPLEMENTATION OF A NOVEL MULTICOPTER UNMANNED AIRCRAFT SYSTEM FOR QUANTITATIVE STUDIES OF THE ATMOSPHERE

A DISSERTATION APPROVED FOR THE
SCHOOL OF ELECTRICAL AND COMPUTER ENGINEERING

BY THE COMMITTEE CONSISTING OF

Dr. Robert D. Palmer, Co-Chair

Dr. Jorge L. Salazar-Cerreño, Co-chair

Dr. Caleb Fulton

Dr. Sebastian Torres

Dr. Greg McFarquhar

Dedicated to my parents, Antonio and Isabel, and to my beloved siblings.

Copyright Notice

The contents of two journal papers were reused extensively throughout this dissertation. The papers, for which I am the first author, have been slightly modified in structure to accommodate the dissertation format.

Parts of Chapters 1, 2, 3, and 4 were composed primarily of material extracted from [1] and [2] with additional or modified figures and analysis.

Acknowledgments

To begin, I would like to extend my gratitude to my advisors Dr. Phillip Chilson and Dr. Jorge Salazar-Cerreño for providing me with the chance to work on my doctorate among an interdisciplinary group of academics and scientists who are extremely inspirational. Their motivation, knowledge, and guidance helped me to solidify the foundations of my research and envision the desired solution for the weather community.

I would like to express my sincere gratitude to Dr. Robert Palmer for becoming my advisor in the last stage of my doctoral studies. Not only for his insights and comments to deepen my research but also for being my best support during difficult times in my professional life. I could not imagine finishing my work in time without his encouragement.

In addition, I like to extend my deepest gratitude to the other members of my doctoral committee for the selfless contribution of their time, support, and direction during the process of preparing and evaluating my work.

I gratefully acknowledge the funding and support received from the University of Oklahoma (OU) and the National Science Foundation. Special thanks to the great team of experts from CIWRO, NSSL, and ARRC of OU, who allowed me access to their facilities and equipment to make this work possible.

A very special thanks to my colleagues and, in particular, Dr. Brian Greene, Dr. Tyler Bell, Gustavo Britto Hupsel de Azevedo, William Doyle, Dr. Elizabeth Pillar-

Little, and Dr. Elizabeth Smith for their support throughout this journey. Working with them was truly an honor and full of memorable experiences.

Also, I am extremely thankful to my close friends, who have been my second home and family since the moment I started my doctoral studies. Special thanks to Dr. David Schvartzman, Jorge Duarte, Dr. Justyna Adamiak, Dr. Arturo Umeyama, Dr. Rodrigo Lebron, Dr. Javier Ortiz, Dr. José Diaz, Adrien Badré, Alejandra Williams, and Julio Rojas.

A big heartfelt thanks to my family for remotely supporting me and believing in me while I pursued my goals and ambitions. I would not have been able to complete what I had started without them.

Table of Contents

List of Figures

Abstract

The call for creating new innovative meteorological instruments to help fulfill observational gaps in the atmospheric sciences has been gaining strength in the past few years. This comes along with the urgent need to increase the understanding of fast-evolving atmospheric processes to subsequently provide accurate and reliable weather forecasts in a timely manner. The increased interest in obtaining atmospheric observations with higher spatio-temporal resolution pushed scientists to begin exploring and harnessing new leading-edge engineering technology. For instance, affordable and accessible Unmanned Aircraft Systems (UASs) technology emerged within this timeframe and has since evolved rapidly. Many researchers and institutions have agreed that UASs are promising technology candidates for targeted *in situ* weather sampling, which has the potential to meet the stringent meteorological measurement requirements. However, the current market has shifted and shaped UASs for other applications that may be unsuitable or suboptimal for weather sampling. Special considerations were examined in this study to conceptualize a specialized weather UAS (WxUAS) capable of collecting reliable thermodynamic and kinematic measurements. While also performing similarly to conventional weather instruments, such as radiosondes, Doppler wind lidars, and meteorological towers, as well as providing a complementary role whenever measurement limitations arise.

Therefore, given that the exploration of integrating weather instrumentation into UAS is rare, it is hypothesized that atmospheric measurements of a modified multicopter UAS that minimizes platform-induced errors can fill the thermodynamic and kinematic data gap in the planetary boundary layer (PBL). The proposed solution is a UAS-based *in situ* vertical profiler system, dubbed the CopterSonde, with necessary weather instrumentation, adequate sensor placement, and useful flight functions for optimal sampling of undisturbed air. This solution attempts to provide a holistic WxUAS design where the UAS itself was adapted to become not just a payload carrier but also part of the weather instrumentation system. Flow simulation studies backed with observations in the field were used to address sensor siting and mitigate sources of thermodynamic errors. Moreover, techniques for thermodynamic measurement correction, adaptable flight behavior, and 3D wind estimation were implemented using the experimental CopterSonde concept with results comparable to widely accepted conventional weather instruments. Additionally, the platform reliability was successfully demonstrated in different challenging environments, from freezing temperatures in Hailuoto, Finland, to high elevations in Colorado, USA. A robust concept of operation and decision-making algorithms were established to ensure safe flights during demanding field campaigns. As a result, the National Oceanic and Atmospheric Administration (NOAA) in the USA has recognized the CopterSonde as part of the approved UAS fleet for NOAA-related missions.

Overall, the engineering advances shown in this work helped to produce an optimized UAS capable of collecting targeted and reliable weather observations. Even though the CopterSonde is an experimental design, this work can be used as a guideline to define future standards for WxUAS development and deployment.

Chapter 1

Introduction

1.1 Motivation

There has been growing interest in the development of unmanned aircraft systems (UAS), also informally known as drones or remotely piloted aircraft systems (RPAS), for academic research and industrial applications. This is mainly due to the emergence of a new commercial sector focused on UAS applications driven by recent advances in the automation of robots, affordable construction materials, and new building techniques specifically for UAS. Consequently, it increased the quality and speed of UAS prototyping for a large number of applications. As a result, new opportunities have emerged to explore novel solutions in different fields such as agriculture, land surveying & surveillance, package delivery, and others [3]. These types of applications seem to be predominant in the UAS market, which, as a result, made manufacturers produce UAS designs optimized for such applications. Whereas UAS focused on weather applications was found to be extremely rare.

In the meteorology field, severe thunderstorms with hail and wind, tornadoes, extreme rainfall and floods, tropical storms, ice storms, heavy snowstorms, and blizzards cost billions of dollars every year to the U.S. economy alone [4–6]. Severe weather aggravated by climate change [7, 8] impacts biodiversity [9], food production [10, 11], supply chain [12], and public health [13], particularly for vulnerable populations [14]. To reduce negative repercussions on society and infrastructure, weather researchers have been insisting on and encouraging the development of novel methods of monitoring Earth's atmosphere [15]. For instance, the introduction of UAS for weather studies which many scholars believe is a suitable candidate technology to fill the existing in situ observational gap present in the lower atmosphere. Recent advances in UAS technology have enabled researchers to perform controlled and targeted atmospheric soundings, which helped create momentum in the community to initiate further developments and studies [16]. Moreover, the National Weather Service (NWS) released a strategic plan in 2019 encouraging weather scientists to begin harnessing new cutting-edge science, technology, and engineering to provide the best possible observations, forecasts, and warnings [17]. Even the National Severe Storm Laboratory (NSSL) has envisioned the integration of large amounts of weather data from multiple sources and scalable to future measurement techniques, a project known as Multiple Radar/Multiple Sensor (MRMS) [18, 19].

With the advent of weather data acquisition using UAS together with the newly established challenge in modern meteorology research, several recent collaborative field experiments have encouraged researchers and engineers to start characterizing and assessing UAS for measuring weather parameters and identify the challenges for improving weather measurements using UAS [20–23]. This initiative led to the development of many innovative UAS designs for weather sampling [24, 25], and to start envisioning future concepts of operations [26] and research communities [27, 28] with a focus on the application of UAS for meteorological studies. Despite presenting attractive and unique features, UAS must still undergo several studies and evaluations before their data get fully integrated and assimilated into the weather forecast models [21, 29, 30]. Moreover, the World Meteorological Organization (WMO) is planning a global demonstration campaign starting in early 2024 with the purpose of showing the current capabilities of UAS and measuring their capacity in contributing to meeting operational requirements, besides analyzing the impacts of UAS data in relevant weather applications and forecast systems [31].

Nowadays, developing a fully autonomous UAS that can operate with little to no human intervention seems to be the next big step in the field. However, the airspace over the United States is regulated by the Federal Aviation Administration (FAA), and their main mission is to deconflict the airspace and keep the airways safe for air travel [32]. Nonetheless, there is a strong interest from the industrial and scientific communities in collaborating with the FAA to provide safe solutions with appropriate risk mitigation for unattended UAS operations in the future [28].

1.2 Problem Statement

The National Academies has initiated and overseen two "Decadal Surveys" over the last 20 years with the goal of generating "recommendations from the environmental monitoring and Earth science and applications communities for an integrated and sustainable approach to the conduct of the U.S. government's civilian space-based Earth-system science programs." [33]. Among these recommendations, it was concluded that vertical profiles in the planetary boundary layer (PBL) of the Earth are inadequately observed in both space and time. The 2017–2027 Decadal Survey, released in January 2018, states "Earth science and derived Earth information have become an integral component of our daily lives, business successes, and society's capacity to thrive. Extending this societal progress requires that we focus on understanding and reliably predicting the many ways our planet is changing." [34]. This second Decadal Survey further reinforces the first one by recognizing boundary layer processes as key to improving weather and climate models.

The PBL is a dynamic region of the Earth's atmosphere that experiences rapid and significant changes in its thermodynamic and kinematic states. Understanding the atmospheric structures is key for improving numerical modeling, simulations, and weather forecasts [29]. However, a combination of fine-scale domain models and higher resolution observations in space and time must be achieved first to advance such understanding [21]. In 2019, the National Research Council stressed the importance of creating a nationwide mesoscale network to address the limitations in sampling the atmosphere [35]. The National Oceanic and Atmospheric Administration (NOAA) has also released a strategic plan in 2020 where it states the overarching goal is to provide accurate, reliable, and timely weather forecasts through the development and application of fully coupled prediction models [36].

A significant in situ observational gap exists in the lower atmosphere, particularly in the PBL [33, 37]. While ground-based weather instruments continue to fulfill scientific needs near the surface and provide data with good spatio-temporal resolution, it is not enough to correctly infer the state of the atmosphere aloft [15]. Radiosondes are used to complement ground-based measurements; however, these are launched only twice per day and spaced over hundreds of kilometers apart due to operating costs, given their lack of reusability. By contrast, UAS are reusable tools that may perform several vertical profiles in a single day, allowing for increased temporal resolution. It is known that radiosondes alone are far from ideal for resolving the fast mesoscale evolution and diurnal variability of the atmosphere [21]. Particularly for the prediction of convection initiation (CI) where the potential instability, moisture, wind shear, and other atmospheric parameters manifest large spatio-temporal variability [38]. Radar networks, Doppler lidars, and satellite observations help mitigate the data gap using remote sensing methods, but at the expense of a few limitations. In general, these

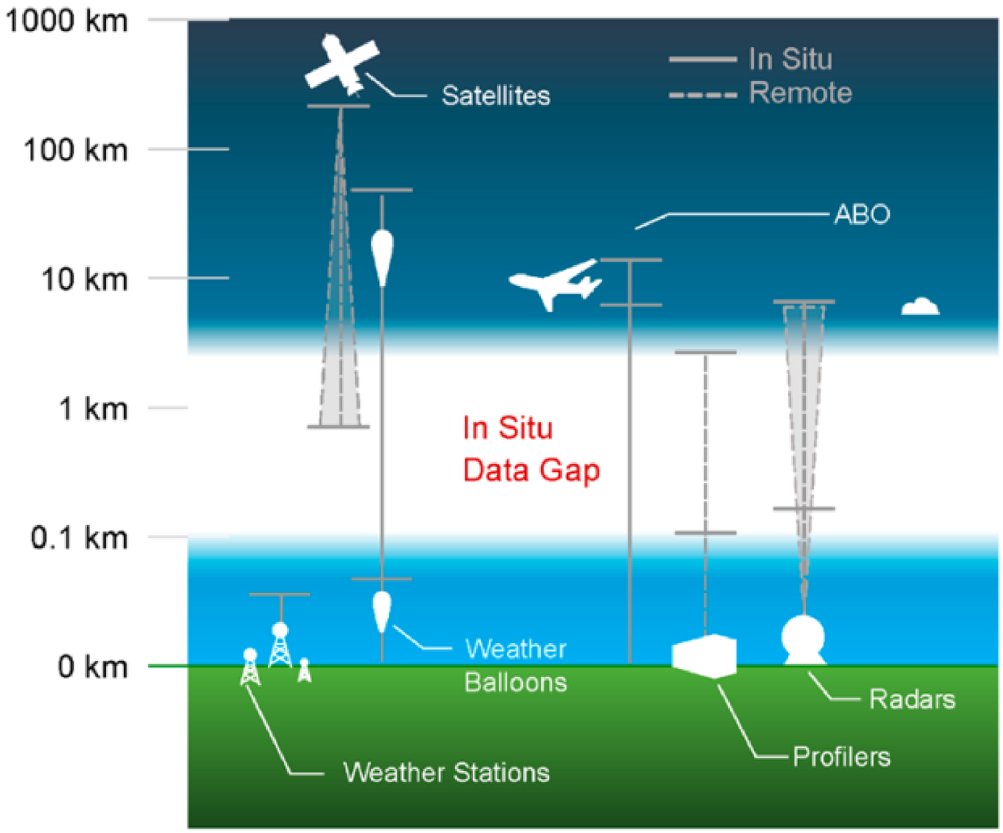

Figure 1.1: Schematic showing the in situ data gap present in the lower atmosphere. Conventional meteorological instruments are illustrated with their respective measurement type and range. ABO stands for Airborne Observations using manned aircraft. Image was taken from [29].

remote-sensing instruments require the presence of scatterers for the estimation of velocity and other limited thermodynamic information. Moreover, satellite observations of the atmosphere are hard to obtain at a few kilometers above the surface, often even getting blocked by the presence of clouds and, hence, data sampling becomes coarse [39]. Figure 1.1 shows a graphical representation of the observational gap together with the limitations of the aforementioned weather instruments.

To overcome these limitations and remain on the cutting edge, the NWS decided that the community must sustain and improve the observing system infrastructure with the implementation of new technologies and measurement techniques while keep exploiting the current instruments [17]. Therefore, several studies and reports have recommended that profiles of wind, temperature, and humidity should be obtained with higher temporal ($<$ 15 min) and spatial ($<$ 100 m in the vertical and $<$ 10 km in the horizontal) resolutions up to 3 km, or more, into the atmosphere in order to fill up the "observational data gap" [21, 37, 40]. Moreover, it is clearly stated in [41] that the full benefit of improved weather forecast models will not be achieved until higher-resolution meteorological observations become available, along with improvements in data assimilation.

Consequently, the meteorology community has started considering UAS as a possible candidate technology for solving the in situ observational gap and fulfilling the desired and more stringent measurement requirements. In particular, multicopter UAS offer certain advantages over other types of UAS, as discussed in Chapter 2. Their capacity for vertical take-off and landing, reusability, and adaptability makes them suitable for vertical profiles of the PBL and, thus, obtain weather variables at desired locations with reduced costs. However, the current UAS market has targeted the UAS design for other applications that may be suboptimal for weather sampling. The accuracy of the weather measurements is subject to several factors, many of them coming directly from the UAS itself [23, 42]. Therefore, the weather-purposed UAS must be substantially different from the standard UAS design to meet desired meteorological observation requirements and mitigate sources of weather measurement errors.

Therefore, this research hypothesizes that the UAS of the multicopter type optimized for atmospheric sampling is capable of filling in the observational gap with high-quality in-situ thermodynamic and kinematic measurements comparable to widely accepted conventional meteorological instruments.

1.3 Literature Review

The idea of unattended and autonomous machines can be associated with Nikola Tesla's works which are reflected in his proposals and patent *"Method of and apparatus for controlling mechanism of moving vessels or vehicles"* [43]. Tesla deserves credit not just for inventing the notion and concept of robots but also for predicting a future in which autonomous flying machines would have extraordinary impacts on commercial applications. Tesla even describes the potential uses for such concept in the following excerpt: *"Vessels or vehicles of any suitable kind may be used, as life, despatch, or pilot boats or the like, or for carrying letters packages, provisions, ... for establishing communication with inaccessible regions and exploring the conditions existing in the same, ... for many other scientific, engineering, or commercial purposes ..."*.

The first recorded attempts at using UAS for atmospheric research go back to the 1970s when Konrad introduced the idea of using hobby-level radio-controlled aircraft to measure weather parameters in convective days [44]. However, efforts to achieve this goal diminished at that time due to the bulky and heavy meteorological sensors, besides the non-existence of autopilot-assisted flights. Despite the extreme technological limitations of the time, their work was a significant step to demonstrate the feasibility of the concept, show the unique advantages over other conventional instruments, and lay down operating procedures using UAS.

Since then, new materials and fabrication technologies for weather sensors have started to surge, allowing for gradual miniaturization of sensors over time [45]. Along with advances in weather sensing, the development of UAS hinged on the confluence of critical technologies like flight propulsion, autopilot systems, and autonomous navigation. Consequently, the effort to create UAS with integrated atmospheric sensors has seen a resurgence in the 1990s [46]. Researchers worldwide have begun modifying

UAS to sample the atmosphere [47–49]. Each had different design characteristics depending on the application, but none truly described the reasons and considerations for their weather sensor placement onboard the UAV.

One of the first UAS designed for PBL measurements is the Small Unmanned Meteorological Observer (SUMO), an autonomous fixed-wing aircraft developed at the University of Bergen as a cost-effective atmospheric measurement system [25]. The SUMO was first deployed in 2007, during the FLOHOF field campaign in Iceland, producing comparable atmospheric measurement results to conventional radiosondes. The SUMO is also known to be one of the first open-source UAS to record weather and flight data through the autopilot. The main disadvantage of the SUMO is its highly demanding operational requirements, like the need for an ample, open, clear space for take-off and landing and skillful operators to fly the UAS. Nonetheless, the capabilities of the SUMO for estimating atmospheric parameters in the PBL were demonstrated to greatly support the importance of UAS in weather studies [22, 50, 51].

Several other weather UAS concepts for PBL measurements made their appearance afterward, with more focus on the integration of atmospheric sensors on board UAS and extensive studies with different configurations [24, 52–54]. This literature collection is evidence of the many prototypes created in the past few years, which contributed substantially to advancing the state of the art. Even though many of these works provide partial solutions to the demands discussed in the problem statement, many questions remain unanswered regarding the mitigation of platform-induced errors.

Commercially available UAS-based solutions exist today; Meteomatics AG is a company located in Switzerland that has been developing and offering the weather UAS “Meteodrone” since 2012 [55]. The company claims that Meteodrone achieved most of the meteorological measurement specifications required by the community, and they are en route to becoming global providers. However, the functionalities are limited to what the company offers, and access to the raw data may not be possible due to the manufacturer's trade secrets. This can end up hindering users in their studies, particularly for research.

Concerning the weather UAS products, there were several documented field campaigns where numerous participants from different Universities and research institutions collaborated in collecting data using various UAS in different weather conditions [20, 21, 56, 57]. The outcome of these large-scale experiments showed the potential benefits of using weather data collected with UAS. Especially for data assimilation into weather models and evaluating the impacts in weather forecasting [30].

1.4 Research Scope

After defining the motivation and problem statement and going over the current literature. It was found that there are a few aspects in the development of UAS-based weather instruments that still need proper solutions to better fulfill the atmospheric measurement requirements and fully exploit the UAS characteristics for optimal weather sampling. This leads to defining the main goals for this research as follows:

1. Develop a robust UAS-based observation system that minimizes platform errors for observations of thermodynamic fields in the planetary boundary layer.
2. Develop an affordable UAS-based wind field estimation technique that is not reliant on expensive, heavy, and cumbersome wind sensors.
3. Expose and analyze the performance of the weather UAS under a variety of weather conditions.

The preliminary stages of this research involve investigating enhancements to the standard UAS design that favors the acquisition of high-quality and reliable weather data. Modifications of the autopilot software and evaluations with simulations were performed to derive the best flight behaviors for weather sampling. Parallel to this, the investigation of the best possible location for the weather sensors onboard UAS, on top of the overall design of the UAS, was conducted using computer-aided design (CAD) and flow simulation software. The combination of these two analyses creates a framework that provides the means for evaluating the impact of potential sources of error, such as heat advection.

Following this, an extensive study on the dynamical model of the UAS body was performed to estimate three-dimensional (3D) wind fields based solely on aerodynamic properties and forces acting on the UAS body. This is done in post-processing through MATLAB scripts, and the algorithm's performance was validated with comparisons against Doppler wind lidar measurements.

After establishing the groundwork, the experimental platform underwent several iterations for design streamlining and improvements. After finalizing a design iteration, the prototype was evaluated and revised thoroughly during extensive field campaigns and presented to the community [58–60]. Preliminary results of flight tests and multiple field experiments with different weather conditions were provided as proof of concept. The final goal was to give the researchers a UAS platform that can deliver reliable, consistent, and rich weather products by taking advantage of the design flexibility of the open-source UAS and fully exploiting its characteristics.

Given that the proposed solution is based on an experimental prototype, there may be minor weaknesses that could not be fully addressed. Therefore, the last stage of this research attempts to provide a guide for future work. This includes discussions on limitations and additional strategies to improve the current weather UAS concept and operations.

1.5 Contribution

The main contribution of this work was the thorough study of a UAS-based meteorological instrument optimized for observing thermodynamic and kinematic weather parameters. Even though other UAS-based platforms for weather applications exist, the presented state-of-the-art weather UAS, dubbed the CopterSonde, has unique custom features specifically designed to exploit the UAS characteristics for acquiring reliable weather observations. The CopterSonde stands out from the rest thanks to the following individual contributions:

1. Engineering field:
    (a) The integration of weather sensor data and custom flight functions into the autopilot code opens opportunities for adaptive weather sampling.
    (b) The proposal of a localized and modular thermodynamic sensor compartment with a dedicated aspiration system.
    (c) The development of reliable 3D wind estimations tailored to the presented CopterSonde UAS design.
2. Meteorology field:
    (a) Introduction of mobile and in situ meteorological UAS instrument for deployment in multiple test sites.
    (b) Participation and support in multiple field campaigns exploiting the CopterSonde design.
    (c) Facilitation for weather researchers to explore a new paradigm and produce scientific contributions using weather UAS.

The overall combination of these contributions makes the CopterSonde UAS become a novel and holistic design for weather sampling. In other words, integrating weather sensing capabilities into the UAS is becoming seamless. Hence, the system can only produce the best possible results when working as a whole. The results of this work helped to create a scrutinized and exemplary UAS platform for weather sampling that meets desired requirements of the meteorology community.

1.6 Dissertation Overview

The work documented in this dissertation is divided as follows. Chapter 2 provides an insight into the theoretical background of the standard UAS. This includes a few design choices for multicopter UAS, such as autopilot systems, types, and geometries, as well as flight performance analysis and environmental limitations. The chapter also reviews the goals, requirements, and desired meteorological measurement specifications for UAS established by the meteorology community, which this work attempts to achieve. In addition, it also discusses a few basic theoretical concepts of the PBL to help understand the thermodynamic and kinematic products of the CopterSonde UAS. An introduction to the weather sensors used and their mathematical models are also presented.

Chapter 3 presents the conceptualization and design process of the CopterSonde UAS. It describes each of its components as well as some of the important decisions made to create a UAS focused on weather sampling. Consequently, optimal weather sensor placement considerations are discussed using results from flow simulation software and supported by observations in the field. Lastly, characterization of the CopterSonde in extreme flight conditions is presented, which led to establishing the design specification and limitations of the platform.

Chapter 4 introduces the weather-specific features developed specifically for the CopterSonde UAS. Techniques for thermodynamic measurement correction, adaptable flight behavior, and 3D wind estimation were tailored to the CopterSonde design and implemented. Thorough comparisons against conventional weather instrument measurements, like radiosonde, Doppler wind lidar, and meteorological tower, were conducted.

Chapter 5 shows the results of some field campaigns in which the CopterSonde was involved and where important enhancements and achievements were made. The chapter summarizes the CopterSonde performance in different field campaigns describing achievements and design flaws. A few studies are cited as evidence to show the scientific relevance of the CopterSonde during these experiments. A description of the general concept of operation of the CopterSonde UAS is also shown.

Finally, Chapter 6 summarizes the achievements made using the CopterSonde UAS since its creation and presents the final remarks and conclusions. A discussion of the foundation for future work closes this work.

Chapter 2

Foundational Background

To understand the problem and, subsequently, the proposed research scope presented in Chapter 1, a description of the concepts and principles involved in UAS design and meteorological sensor selection must be provided. This is particularly true when associated with meteorological applications such as thermodynamic measurements of the PBL. Therefore, this chapter summarizes the key principles needed to comprehend the topic better. The following section presents the basic design principles of UAVs, covering kinematics and dynamics for the multicopter architecture, and describes components to create a functional UAS. Subsequently, brief fundamentals of small thermo-hygrometer sensors are introduced for sensor characterization and measurement correction. Finally, a short description of the PBL where the proposed UAV was designed to operate.

2.1 Unmanned Aircraft System Overview

2.1.1 Clarification of Terminology

Recently, there have been several names found in the literature that are being used interchangeably to describe unmanned aviation and aircraft. The term “drones” has become a standard for flying robots or vehicles controlled remotely or by onboard autopilot systems. This term is commonly used in the industrial and defense markets and is a popular term among users worldwide.

However, Unmanned Aerial Vehicle (UAV), Unmanned Aircraft System (UAS), Remotely Piloted Aircraft (RPA), and Remotely Piloted Aircraft System (RPAS) are other technical terms typically used in the scientific literature. Throughout this dissertation, UAV and UAS are used as the preferred terms. It should also be stated that UAV and UAS have different meanings and should be clarified to avoid confusion. The term UAV implies a pilotless aircraft or, in other words, a flying machine without a human pilot or passengers on board. As a result, the term “unmanned” refers to the absence of humans who actively control the aircraft, where the control functions can be onboard or offboard. The term UAS was first introduced by the U.S. Department of Defense (DoD) and was quickly adopted by the Federal Aviation Agency (FAA) and the European Aviation Safety Agency (EASA). UAS indicates systems like ground control stations, communication networks, launch and recovery devices, and the UAV itself.

Given that this work is related to atmospheric studies, the terminology proposed by [61] has been adopted, which includes the word “weather” (Wx) as an adjective for UAS to discern other UAS from those explicitly meant for weather sampling. To be clear, the phrase UAV or WxUAV refers to the aircraft itself, and UAS or WxUAS refers to the whole system described above. It is also assumed that the term “weather” includes clear atmosphere.

2.1.2 Classification

As with any other aircraft, UAVs can be classified according to their design configuration, flight ceiling, degree of autonomy, type of payload, etc. Different entities, such as the DoD, FAA, and EASA, have their own classification tables that differ from each other. There is no unique convention about the classification and guidelines around these systems, but rather regulations that users must abide by depending on the UAV flights' location. Since this project was mainly carried out in the United States, the FAA regulations were adopted, which define a few UAV design parameters and flight planning procedures primarily intended for safety. The FAA's primary mission is to deconflict the airspace and keep the airways safe. Hence, it is imperative that UAS operations always comply with the FAA rules. When this document was written, the FAA Part 107 and Certificate of Authorization (COA) regulations, both issued by the FAA [62], have been complements to the engineering challenges of this project.

UAVs can be classified in several ways; however, one common separator is the structure of their lift-producing surfaces. UAVs are divided into fixed-wing and rotary-wing aircraft based on the most commonly used propulsion and flight methods. Fixed-wings UAVs, as the name implies, have wings that do not move and are attached to the body of the UAV. They typically have control surfaces that can rotate, such as ailerons and rudders, to produce a change of attitude and orientation. Under this arrangement, lift is created by the aircraft's forward thrust combined with the aerodynamic shape of the wing, which produces pressure differential and, hence, lifting force. For rotary-wing UAVs, the rotor blades rotate at high speed around the central mast, pushing air downwards and generating vertical lift to keep the aircraft airborne. Rotary-wing UAVs may have either a single rotor (helicopter) or multiple rotors (multicopter) generating thrust. One of the main advantages of multicopter UAVs is their simpler rotor mechanics. This significantly reduces the overall size, weight, and cost of the UAV. Unlike helicopters with bulky and complex pitch rotors using mechanical linkages, multicopters have fixed-pitch blades [63]. This allows them to control the flight by varying the relative speed of their rotor blades. From an economic standpoint, multicopters are more affordable and accessible technology compared to helicopters making multicopters more attractive for prototyping and research.

2.1.3 Building Blocks of a Multicopter

The many components of a multicopter UAS can be both basic and sophisticated. The multicopter UAS is often built using numerous modularized components that are generally highly compatible. On the other hand, it can also be a complicated process because each component is not completely independent since they link and interact with others in a complex fashion altering the behavior of the multicopter. Though there are several ways to construct a multicotper UAS, only a few configurations may be functional for a given application [64]. As illustrated in Figure 2.1, a typical UAS includes:

1. Autopilot system: The autopilot of a UAS is a combination of hardware and software that work together to stabilize and navigate the UAV with little to no intervention from human operators. In general, the autopilot code is run by a single microprocessor that handles and operates all data from sensors and command inputs to produce desired flight behaviors.
2. Sensors and Inertial Measurement Unit (IMU): The autopilot must get information about the state of the UAV to run the flight algorithms. The IMU combines the readings of onboard sensors like the global navigation satellite system (GNSS), accelerometers, and gyrometers, which then supplies the autopilot with best-possible estimates of the position and orientation of the UAV.
3. Payload: This is the load carried by the UAV, which, in general, is not crucial for flight functions but for the purpose of the application. Some commonly used payloads found in the UAS market are cameras and lidars.

4. Propulsion: This component is an essential part of the multicopter UAV for motion. It produces the necessary lifting thrust to keep the UAV aloft. It typically consists of propellers, actuators (or motors), drivers (or electronic speed controllers), and fuel cells (or batteries).

5. Airframe: The airframe houses all essential components that enable flight, including the body's frame and propulsion. It also gives support to the payload.

6. Ground control station (GCS): the GCS is used to generate flight plans, send commands to the UAV, and monitor the flight status of the UAV in real-time. It typically consists of computers, joysticks, and radios. These radios work at one or more frequencies and are used to communicate with the UAV and take control if necessary.

7. Communication System: this consists primarily of the wireless link between the UAV and the GCS. The UAV gathers telemetry data about the vehicle status, which is sent to the GCS. The GCS displays the received telemetry data and reports it to the human operator. Besides this, it can also send commands to the UAV.

8. Launch and Recovery System: Some UAS requires special methods and devices to launch them into the air and recover after the flight. These systems vary in complexity based on the desired level of autonomy and human intervention, including battery charging, UAV inspection, diagnosis, data distribution, etc.

Figure 2.1 provides a breakdown of the UAS structure into its basic building blocks. These are the minimum required components to build a functional UAS that can fulfill the desired application with some degree of autonomy [64].

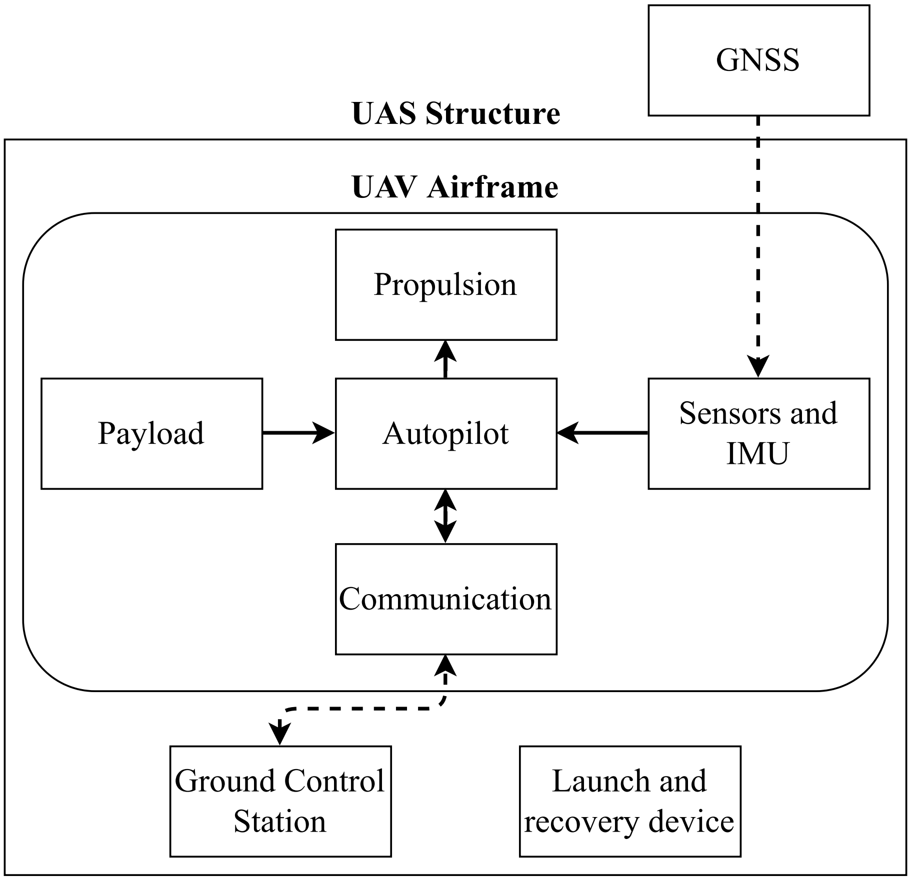

Figure 2.1: Diagram of UAS structure and basic building blocks. Each of these elements is crucial for the overall functionality and operation of the UAS. This combination also enables autonomous capabilities in outdoor conditions. The dash lines represent wireless links.

2.2 Fundamentals of the Atmosphere

To correctly undertake the engineering challenges of this project and address solutions to the atmospheric measurement needs, it is important to have some basic knowledge of the atmosphere. At its core, meteorology is Newtonian physics for the atmosphere, where Newton's second law governs motion, whereas heat obeys thermodynamic laws, while pressure and moisture concentration follow equilibrium and conservation laws, respectively. These known physical processes are used to describe the fluid mechanics of the atmosphere [65].

The atmosphere is a complex fluid system that generates chaotic motions and microphysical processes that are referred to as weather. This chaos and complexity are caused by the interactions between air masses and various physical processes at different Earth locations. For instance, temperature differences can cause winds to move around and create pressure differences that can affect the flow and, consequently, transport water vapor and other atmospheric constituents. These processes are known to be highly nonlinear, contributing to the complexity of the governing equations of the atmosphere. Despite the complexity of the atmosphere's behavior, there is still a significant understanding of its physical properties thanks to theoretical studies and empirical relationships found after extensive observations. Field observations are an important component in weather studies.

The Earth's atmosphere is divided into layers, each with its unique set of characteristics. By defining H as the geopotential height, these layers are classified as the troposphere (H $\leq \sim$11 km), stratosphere ($\sim$11 km $\leq$ H $\leq \sim$47 km), mesosphere ($\sim$47 km $\leq$ H $\leq \sim$85 km), and thermosphere ($\sim$85 km $\leq$ H) in this order starting from the ground and going up to the free atmosphere and interplanetary space [65]. These values are based on global averages, and local conditions can vary with latitude and weather conditions. Figure 2.2 depicts the different layers of the atmosphere based on the vertical temperature distribution. The temperature structure is an accepted way to differentiate each layer due to the noticeable temperature maximas and minimas that occur at the transition of each layer. The temperature maximas result from significant solar radiation absorption at those heights. Ozone absorbs ultraviolet light at the stratopause, visible light is absorbed in the ground, and most other radiation is captured in the thermosphere.

The troposphere is the Earth's innermost layer of the atmosphere, containing $\sim$80 % of the entire mass of the planetary atmosphere, $\sim$95 % of the total mass of water vapor

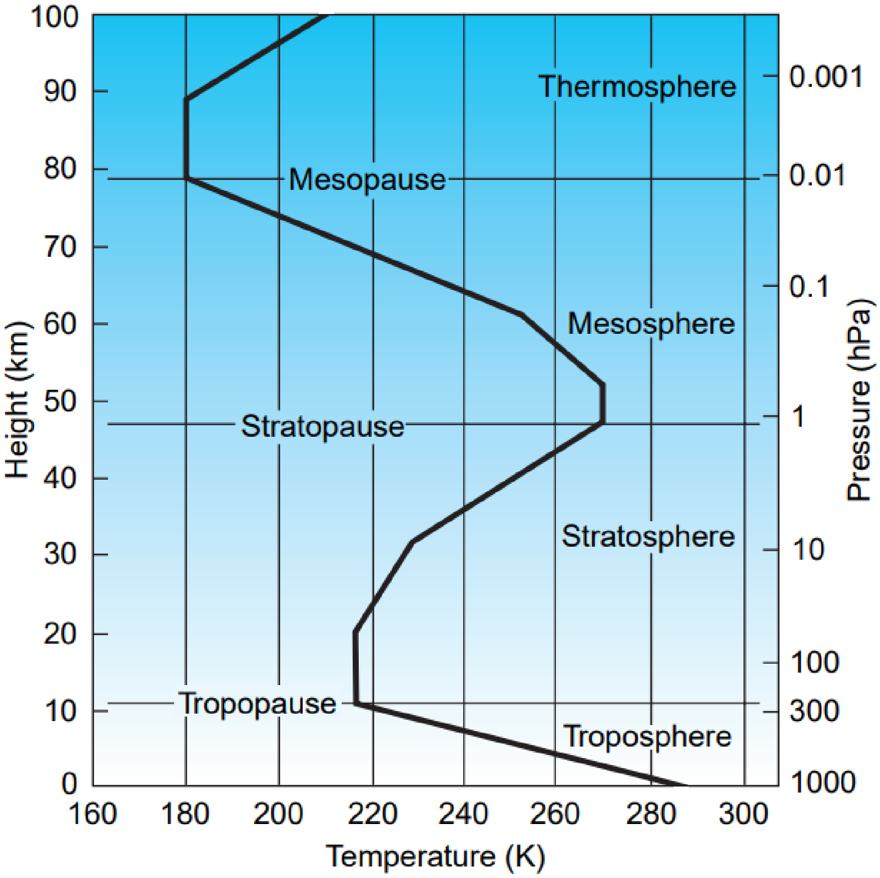

Figure 2.2: Plot of the different layers of the Earth's atmosphere based on the vertical distribution of temperature for typical weather conditions. Image was taken from [66].

and aerosols, and is where most weather developments occur that directly affect life on Earth. The name troposphere was derived from the Greek words tropos (rotation) and sphaira (sphere), hinting that rotational turbulence mixes the air, mainly caused by interactions of the Earth's surface. The troposphere is generally characterized by its decreasing temperature over height with a slope of $\sim$6.5 ^{o}C km^{-1}, commonly known as the moist adiabatic lapse rate. The troposphere also has shallow layers in which temperature rises with height instead (or negative lapse rate). Vertical mixing seems to be significantly restricted inside these so-called temperature "inversions," giving place to the formation of a sub-region of the troposphere known as the PBL.

2.2.1 Planetary Boundary Layer

The atmosphere begins at Earth's surface, the bottom boundary that affects the air immediately above it. The planetary boundary layer is defined as the region of the atmosphere in which interactions with the surface are the main influence on atmospheric properties. The contact between the surface and the air is extremely turbulent, allowing the air to rapidly absorb properties of the surface underneath it. In fact, the boundary layer can experience changes within 30 min or less. Depending on the season and the location on the Earth, the PBL thickness may vary from tens of meters to 4 km or more, and, in general, it occupies the lowest $\sim$20 % of the troposphere [65, 66].

Over a diurnal cycle, the PBL processes can evolve rapidly, mainly driven by solar radiation heating the surface of the Earth and modulated by the rotation of the Earth. This natural mechanism generates intense thermodynamic variations in the lower atmosphere and, consequently, creates a variety of atmospheric structures. The conceptual model of the PBL depicted in Figure 2.3 is a particular case that shows the different subregions of the PBL: mixed layer (ML), capping inversion (CI), stable boundary layer (SBL), entrainment zone (EZ), and residual layer (RL) [26]. The free atmosphere (FA) can be considered decoupled from the PBL because the effects of the Earth's surface friction on the air motion are negligible in this region. A sequence of distinguishable structures or states of the idealized PBL is illustrated and labeled (A-E). The initial state is (A), which forms at night and has a stable boundary layer and well-mixed residual layer. Soon after sunrise, the Earth's surface warms up, and, as a result, it creates and feeds the ML. The PBL then transitions from the state (B) to state (C) in a matter of a few hours. As the ML continues to grow, the SBL rises and shrinks, generating the EZ. However, the short-lived EZ disappears extremely fast, and the RL merges with the ML, which marks the transition to state (D). The PBL stays as a well-mixed layer for the remaining of the day. At sunset, solar radiation diminishes, and the Earth's surface begins to cool down, generating the conditions for the development of the SBL. This marks the end of the diurnal cycle at state (E).

The description of the diurnal cycle helps to visualize the many interactions and intricacies of the PBL processes, which develop quickly throughout the day. Moreover, longer timescale variations associated with changing weather patterns are superimposed on these diurnal cycles. For example, the PBL becomes unstable due to the displacement of cold air mass over warmer regions as a result of a cold front or heat convection from the ground. These weather phenomena are called frontal and thermal inversions (FTI), respectively. Regarding storm formation, the PBL supplies a significant portion of the moisture, instability, low-level wind shear, and force required to create severe storms with tornadoes, hail, lightning, and high winds. When contemplating the likelihood of convection initiation, forecasters constantly examine moisture advection, and moisture gradient trends [67]. The storms' outflows inside the PBL may govern the severity and duration of severe storms or even create new storms. Observing and understanding these factors is essential for improving forecasts of severe and high-impact weather. However, as mentioned in the previous chapter, the PBL properties evolve rapidly, which makes it difficult to capture its dynamics with existing meteorological instruments. Therefore, to fully characterize the PBL, it is necessary that measurements of the atmospheric parameters have sufficient temporal and spatial resolution to capture the rapid development of the structures [26].

2.2.2 Basic Turbulence Theory

The atmosphere is in a perpetual state of horizontal and vertical motions while constantly evolving day and night. This constant motion in the atmosphere produces nat-

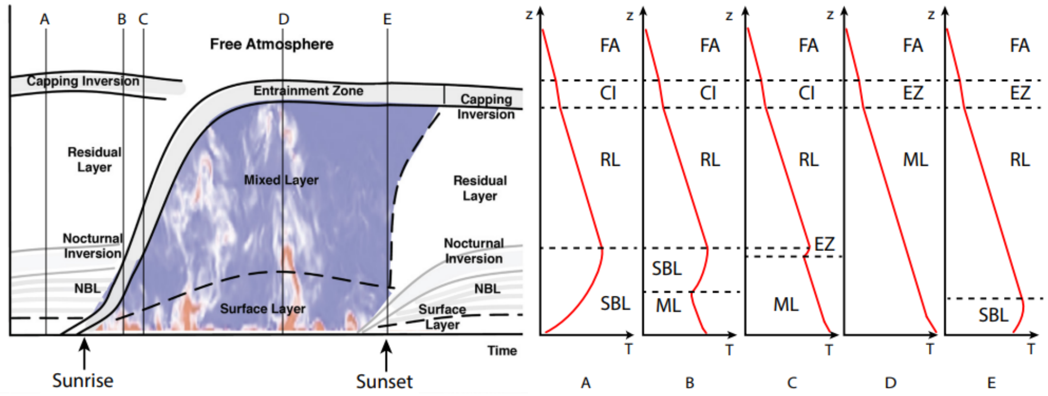

Figure 2.3: Schematic illustrating the different sub-regions of the idealized PBL during a diurnal cycle (left). Idealized vertical soundings of temperature at five different times within the cycle, each presenting discernible structures (right). Image was taken from [26].

ural thermodynamic variations that usually have a high degree of complexity in time and space [68, 69]. However, interesting turbulence patterns were discovered throughout the history of atmospheric sciences, which led to the formulation of methods to describe these complex variations statistically. For instance, the energy cascade theory formulated by Kolmogorov is a classic example [70]. This technique can be used to estimate the turbulence energy distribution of thermodynamic and kinematic parameters over a range of spatial scales under locally isotropic conditions.

One technique is Kolmogorov's turbulence spectra (KTS), which was adopted in this study as another way of validating results besides the measurement comparisons with conventional meteorological instruments. The KTS requires particular atmospheric conditions so that the assumptions hold true. Therefore, for the demonstrations of this study, the selection of PBL conditions was narrowed down to one particular case: a well-mixed convective boundary layer (CBL) during windy conditions. The CBL has special atmospheric conditions for evaluating weather sensors on UAVs because of several theoretical assumptions that can be made when running experiments

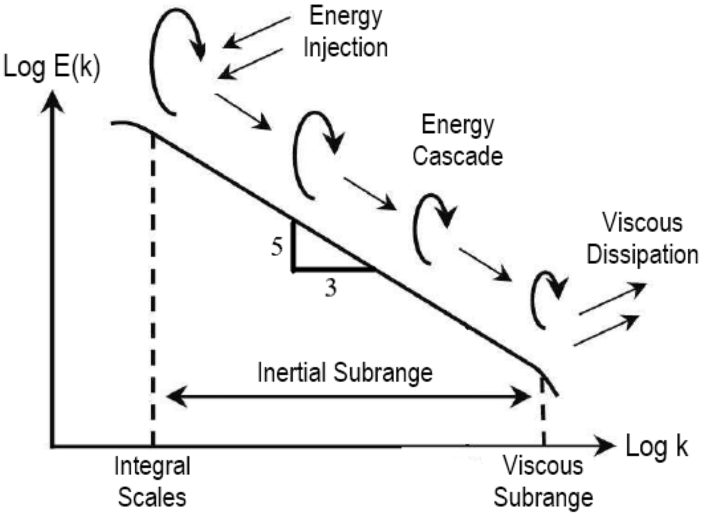

Figure 2.4: Illustration of Kolmogorov's energy cascade process. The large-scale motion of air masses injects energy into the atmosphere, which then breaks down into turbulent eddies transferring energy to a smaller scale. The cascade ends when small eddies reach the viscous region, dissipating the energy into heat.

and simulations.

The CBL condition is ideal for studying small-scale turbulence and the high-frequency response of the sensors by means of the power spectrum and the structure-function analysis. In one of the most extensive experiments conducted by [71], it was shown that in a turbulent atmosphere with a high Reynolds number R_e, in the order of $R_e > 10^6$, the energy cascade decreases with a -5/3 slope in a logarithmic scale and then tails off downwards in the viscous dissipation region (Figure 2.4). The approximate relation between the turbulence energy Φ_T of temperature and the spatial wavenumber k of the temperature signal is given by [72]:

$$\Phi_T(k_1) \approx 0.25 C_T^2 k^{-5/3}, \tag{2.1}$$

where C_T is the structure-function parameter for temperature. The humidity also has a similar expression as Equation (2.1) but with a different proportionality constant.

Assuming the volume of air sampled by the UAS is locally isotropic, the thermo-hygrometers should observe a pattern where the spectra approximate the -5/3 slope line. Assuming that the frequency content of the turbulent eddies is larger than the frequency range of the sensor, then any deviation in the measurement spectra is considered to be influenced by undesired sensor dynamics or external perturbations.

Moreover, the ratio between large and small spatial scales is approximately given by $l/\eta = Re^{3/4}$ [73]. Consequently, the large separation of scales allows for the inertial subrange (ISR) of turbulent fluctuations to extend for hundreds of meters in length, which would be quite difficult to capture with a UAS within a reasonable time. A workaround to this issue is to assume horizontally homogeneous CBL conditions. Consequently, turbulence can be assumed to be "frozen" as it travels across a stationary UAV at a constant speed. This assumption is the so-called Taylor's hypothesis of the frozen-field, and it is of great use in calculating the structure-function parameters by converting temporal measurements into spatial measurements.

The definition of the structure-function can be found in the literature [74–76]. The physical interpretation of structure-function is the distribution of turbulent energy over different spatial scales, and it is mathematically defined as a two-point spatial correlation as follows:

$$D_T^2(\mathbf{r}) = \overline{(T(\mathbf{x}) - T(\mathbf{x}+\mathbf{r}))^2} = C_T^2 r^{\frac{2}{3}}, \tag{2.2}$$

where the overbar represents ensemble averaging, $\mathbf{x}$ is the position vector in meters, and $\mathbf{r}$ is the separation distance between two samples in space, also called distance lag. If the distance lag $\mathbf{r}$ is within the ISR, then the structure-function is reduced to the rightmost expression of Equation (2.2). In the ISR region, the structure-function follows a 2/3 slope line law in a logarithmic scale. The computation of the structure-function is straightforward and has relatively fewer theoretical assumptions than the conventional spectral analysis [74]. The presented KTS theory and structure-function analysis were used as an extra validation step of the thermo-hygrometer observations and technique discussed in Chapter 4.

2.3 Weather Sensors Principle and Modeling - Specific Example

The performance optimization of thermo-hygrometers starts with the available manufacturing technologies [45]. Nowadays, the fabrication of sensors is driven by low-cost circuits, new sensing materials, advances in miniaturization techniques, and modern simulations. Even though a great part of the sensor's performance can be optimized at a hardware level, they still come with limitations. Post-processing algorithms can partially overcome these limitations in performance, modeling techniques and digital signal processing being the most popular. For instance, [77] showed encouraging first results using a simple first-order differential equation to restore signals from a thermocouple and even describing calibration procedures. [78] used non-linear differential equations based on the Stein-Hart equation for negative temperature coefficients (NTC) thermistors [79]. Their equations consisted of a lumped formulation for temperature, which included other factors like thermal radiation and power dissipation. Despite its high accuracy, the complexity of the model makes it impractical for real-time implementation, especially on microcontrollers with low computational resources, like some used for autopilots. Moreover, another study has shown that having a good solar radiation shield around thermo-hygrometers and adequate sensor placement on the UAV can greatly prevent thermal energy from contaminating the air being sampled [42]. Therefore, assuming that the external sources of contamination were mitigated, the following sections provide basic knowledge to start exploring methods for sensor measurement correction.

Table 2.1: Technical specifications of the thermodynamic sensors used in this work according to their respective manufacturers [80–82].

Sensor	iMet-XF bead thermistor	HYT-271	MS5611
Type	Temperature	Rel. humidity	Absolute pressure
Sensing element	Bead thermistor	Capacitor film	MEMS[2]
Dimensions	0.4 mm ⌀	5×10×2 mm	5×3×1 mm
Weight	10 gr	7 gr	–
Range	-90–50 °C	0–100 %	10–1200 mb
Response time[1]	≤ 2 s	≤ 5 s	≤ 8.22 ms
Resolution	0.01 °C	0.1 %	0.065–0.012 mb
Accuracy[1]	±0.3 °C	±0.1 %	±1.5 mb
Sampling rate	10 Hz	10 Hz	10 Hz
Protocol	I^2C	I^2C	SPI

[1] at 5 m s^{-1} airflow across and Standard Ambient Temperature and Pressure (SATP).
[2] Micro Electro-Mechanical System.

2.3.1 Description of Thermo-Hygrometer Sensors

There was no engineering selection process for this work for the thermo-hygrometer sensors. Due to legacy decisions and cost constraints, a set of bead thermistors from InterMet (iMet) [80] systems and HYT-271 capacitive humidity sensor from Innovative Sensor Technology (IST) [81] were provided as a payload requirement for the development of the WxUAS. Table 2.1 shows a summary of the specifications for each sensor, including the pressure sensor used, which comes with the autopilot board. A useful feature of the iMet bead thermistor and HYT-271 humidity sensor is their capability to stream digital data through a communication protocol known as the inter-integrated circuit (I2C). The I2C protocol is a popular data transfer method among digital microcontrollers, and it enables communication with peripherals on a single data bus. This is advantageous when the end goal is to have a more integrated and holistic system, which will be discussed in the following chapter.

Despite the absence of a formal sensor selection process, these types of sensors are considered payload friendly for small UAS, given their compact size and lightweight characteristics. Commonly used temperature and humidity sensors for UAS are mainly variants of the bead thermistor type and capacitive type sensors [20, 22].

2.3.2 Thermo-hygrometer Dynamical Model

The key assumption of the models presented in this Section is that temperature and humidity differences inside the sensing element are comparable to the differences between the element's surface and the fluid in direct contact. This means that the internal geometries of the sensing element can play a significant role in the transient response of the sensor and, thus, are considered a cause of slow sensor dynamics.

Both temperature and humidity sensors work under similar principles. Basically, the heat flux (diffusion) inside the sensor's material will lead to a thermal (water vapor concentration) equilibrium with the surrounding medium after a finite time. In fact, the differential equation that describes a great part of their behavior has the same form for both sensors, which is given by [83]:

$$\frac{\partial U}{\partial t} = k \left(\frac{\partial^2 U}{\partial x^2} + \frac{\partial^2 U}{\partial y^2} + \frac{\partial^2 U}{\partial z^2} \right). \tag{2.3}$$

This is called the heat equation for the case of temperature and the diffusion equation for the case of water vapor concentration. Numerous parameters have an influence on the response time of a sensor, such as the geometry of the sensing element, the inherent thermal/water diffusivity of the sensing element, the thickness of the protective layers, and even the ambient temperature and humidity itself [45]. Equation (2.3) encompasses most of these characteristics and factors and can be effectively used as a model to compensate for errors.

In the simulation of solid bodies, the finite difference method is a commonly used numerical solution for differential equations involving geometries. Finite difference equations are powerful tools that can be used to create mathematical models and describe the behavior of physical systems. The method uses an approximation to the total derivative given by the slope of a finite interval around a given point. Additionally, assumptions must be made to reduce the complexity of the model and work within a linear regime. The dynamics of the sensor can be further studied after deriving the mathematical model. It can be used to trace back and restore the original signal that produced the sensor measurements as long as the inverse of the model exists and is stable [84].

Forward Model of Temperature Sensor

The shape and dimensions of the chosen iMet-XF bead thermistor are shown in Figure 2.5. The probe's tip was assumed to be spherical with a radius $R = 0.4$ mm, ignoring the electrical wires. Given that heat fluxes can propagate in any direction around the sensor, the problem becomes three-dimensional in space. The spherical symmetry helps to reduce the degree of complexity of the model significantly, and the equations simplify to a one-dimensional case along the radius [85]. It was also assumed that heat energy only propagates radially, being the positive direction from the surface of the sphere, in contact with the air, to the core where the sensing element is located. Therefore, the problem can be seen as a heat transfer problem with spatial temperature gradients inside the thermistor. Applying these assumptions to Equation (2.3) and expressing the result in spherical coordinates, then the differential equation for the bead thermistor is given by:

$$\frac{\partial T(r,t)}{\partial t} = \alpha \left(\frac{\partial^2 T}{\partial r^2} + \frac{2}{r}\frac{\partial T}{\partial r} \right); \ 0 \leq r \leq R, \ t \geq 0, \tag{2.4}$$

where the internal temperature T is a function of time t and space r, which is the radial distance from the center to a given point within the sphere, and α is the thermal diffusivity of the material. In order to implement computational algorithms, Equation (2.4) must be transformed to a discrete system by dividing the sphere into N layers with thickness $\Delta r = R/N$. Then, finite difference method, as defined in Section 2.3.1, was applied to the spatial derivatives of Equation (2.4), knowing that the boundary conditions are given by $T(R,t) = T_{air}$ and $T(0,t)$. The latter condition is a singularity that was resolved by applying the L'Hopital rule. Finally, solving for the temporal derivatives, the following system of finite difference equations in space was obtained:

$$\frac{\partial T}{\partial t} = \beta\left(-2T_N + \frac{N-1}{N}T_{N-1}\right) + \beta\frac{N+1}{N}T_{air} \qquad r = R, \tag{2.5}$$

$$\frac{\partial T}{\partial t} = \beta\left(\frac{i+1}{i}T_{i+1} - 2T_i + \frac{i-1}{i}T_{i-1}\right) \qquad 0 < i\Delta r < R,\ i = 2, ..., N-1 \tag{2.6}$$

$$\frac{\partial T}{\partial t} = 3\beta\left(T_2 - T_1\right) \qquad r = 0, \tag{2.7}$$

where $\beta = \alpha/\Delta r^2$. The resultant set of equations is a linear time-invariant (LTI) system that can be transformed into the state-space representation of the form:

$$\frac{\partial x}{\partial t} = Ax + Bu \tag{2.8}$$

$$y = Cx + Du, \tag{2.9}$$

where x is the state variable vector (each element representing the temperature at each layer), u is the input signal (the temperature at the surface), and y is the output signal

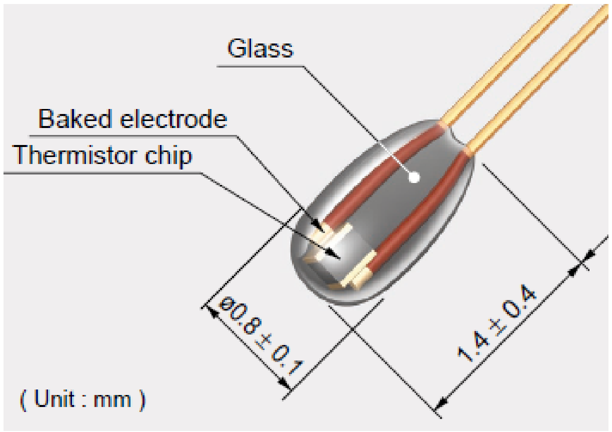

Figure 2.5: Close-up of the iMet-XF bead thermistor with dimensions and composition. This the sensing element of the temperature sensor installed on the proposed WxUAS. Image provided by International Met (InterMet) Systems.

(temperature measurement at the core). The elements of the matrices A and B were obtained by examining the finite difference equations.

Forward Model of Humidity Sensor

In the case of the HYT-271 capacitive humidity sensor, the dynamics are mainly produced by the diffusion of water vapor from the surface in contact with the air into the sensing element made of a polymer. Figure 2.6 shows the sensing element configuration and the boundary conditions around it. In contrast with the bead thermistor, the capacitive sensor can be treated as a one-dimensional problem since the water vapor only exists above the surface of the sensing element, and it propagates in the direction normal to the surface (inwards is positive).

Horizontal water vapor concentration gradients were considered negligible given that the thickness of the polymer is small enough to prevent horizontal propagation [84]. Similar to the bead thermistor case, the differential equation for the capacitive humidity sensor was derived from Equation (2.3) expressed in one-dimensional Cartesian

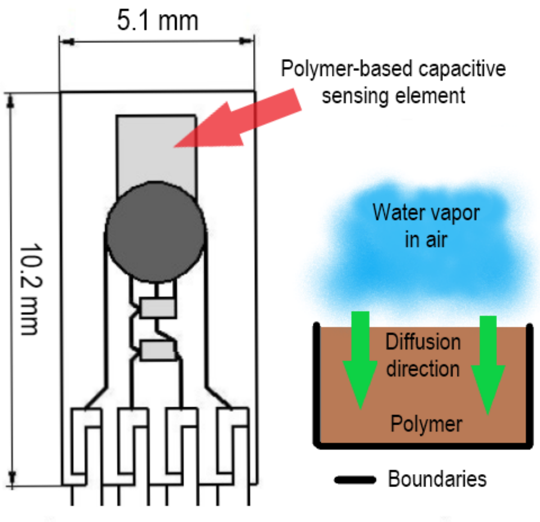

Figure 2.6: Close-up of the IST HYT-271 capacitive sensor with dimensions (left) and sensing element configuration (right). The left image was taken from the IST HYT-271 datasheet.

coordinates:

$$\frac{\partial c(x,t)}{\partial t} = D\frac{\partial^2 c}{\partial x^2};\ 0 \leq x \leq L,\ t \geq 0, \tag{2.10}$$

where c is the water vapor concentration in parts per million volume (ppmv), D is the diffusivity coefficient of the water vapor in the polymer, and L is the thickness of the polymer. Applying finite difference to Equation (2.10) and following similar procedures as shown in the bead thermistor case, the system of finite difference equations for the capacitive humidity sensor is:

$$\frac{\partial c}{\partial t} = \lambda\left(-2c_N + c_{N-1}\right) + \lambda c_{air} \qquad x = L, \tag{2.11}$$

$$\frac{\partial c}{\partial t} = \lambda\left(c_{i+1} - 2c_i + c_{i-1}\right) \qquad 0 < i\Delta x < L,\ i = 2, ..., N-1 \tag{2.12}$$

$$\frac{\partial c}{\partial t} = \lambda\left(c_2 - c_1\right) \qquad x = 0, \tag{2.13}$$

where $\lambda = D/\Delta x$. Again, the resulting system of equations is an LTI system that can be transformed into state-space representation. The matrices A and B were determined by inspection of the resultant set of finite difference Equations (2.11–2.13).

The finite difference model only takes water vapor concentration as the input signal, whereas the output of the humidity sensor is relative humidity expressed as a percentage. Therefore, the relative humidity must be converted to water vapor concentration before using the model. The following equations for the conversion were taken from [86]:

$$c = 10^4 H \frac{P_s}{P_a}, \tag{2.14}$$

$$p_{sat} = p_a \exp(13.3185t - 1.9760t^2 - 0.6445t^3 - 0.1299t^4), \tag{2.15}$$

$$t = 1 - \frac{373.15}{T_{air}}, \tag{2.16}$$

where H is the relative humidity in percentage, p_{sat} is saturation vapor pressure in millibars, $p_a = 1013.25$ mb is the standard atmospheric pressure, T_{air} is the temperature of the surrounding air in Kelvin. The numerical error is less than 0.5 $\%$ within a temperature range of -50 °C and 50 °C.

2.4 Chapter Summary

The call for creating innovative techniques for sampling the atmosphere at high spatio-temporal resolution has been increasing in recent years. However, performing *in situ* atmospheric measurements is a complex problem that spans comprehensive aspects such as sensor characterization, design of the instrument, and the understanding of atmospheric processes. A method gradually gaining traction is using UAS as a platform to carry atmospheric sensors at desired locations for targeted sampling. This work attempts to bring design enhancements to the conventional UAS and specialize it for accurate atmospheric measurements. UAS definitions, thermo-hygrometer models, and basic knowledge of the PBL were presented in this chapter to show the intricacies of each subject. Establishing these fundamental concepts should provide links for a better understanding of the aspects involving atmospheric measurements useful for the subsequent chapters.

Chapter 3

Multicopter UAS Design for Atmospheric Sampling

In this work, the conceptualization and initial design of the WxUAS resulted from a much larger and more ambitious project attempted by the Center for Autonomous Sensing and Sampling (CASS) of the University of Oklahoma (OU) from 2016 to 2021. This larger project was referred to as the “3D Mesonet” and revolved around the idea of expanding thermodynamic and kinematic measurements of the atmosphere above the Earth’s surface [26]. The ability to capture vertical wind, temperature, and moisture profiles in the lower troposphere with high spatial and temporal resolution has long been a desirable feature of operational observing systems worldwide.

Consequently, the proposed solution was to use WxUAS with the capacity of sampling the vertical structure of the PBL and, possibly, the rest of the troposphere as well. In other words, 2D surface measurements from existing tower-based sensors would be augmented with profile data from instrumented UAVs launched from a network of ground stations capable of supporting these activities. As a result, this innovative technology promises to fill data gaps in the PBL that conventional instruments cannot easily or economically achieve. It would also detect mesoscale properties unseen before that are inherent in weather systems. These sounding or profile data may be used to investigate thermal stratification as well as atmospheric static and dynamic stability, all of which influence storm genesis and maintenance [29].

In this chapter, the main topic of discussion is the design process, the implementation of custom features, and component selection and arrangement to create an appropriate UAV for thermodynamic and kinematic profiling. The latest developments of an innovative multicopter UAV, henceforth referred to as the CopterSonde, are presented. Flow simulation results and real measurement comparisons against conventional weather instruments were used to show evidence of the data quality produced by the proposed WxUAV design. The flight performance of the UAV is also discussed based on the design calculations and results from stress flights performed in outdoor scenarios.

3.1 The CopterSonde Conceptualization

The overall operating concept for the 3D Mesonet imposed specific design constraints on the WxUAV to be employed. Flights should be carried out autonomously or semi-autonomously, with as little human intervention as possible. Since the focus is on atmospheric soundings, the CopterSonde must execute a vertical ascent and descent in a straight line. Therefore, the CopterSonde should include vertical take-off and landing (VTOL) capabilities, which was accomplished by utilizing a rotary-wing UAV.

Additionally, the CopterSonde design has been driven by meteorological sampling requirements. These meteorological sampling requirements include the type of measurement and the accuracy of the observations. The 3D Mesonet project was mainly intended to characterize the thermodynamic and kinematic state of the lower atmosphere. The desired atmospheric parameters were pressure, temperature, humidity, and wind, with high spatio-temporal resolution compared to other similar instruments, such as radiosondes. Therefore, the CopterSonde must be able to carry the weight of additional sensor packages for atmospheric sampling in a modular fashion.

Regarding the desired maximum altitude above ground level (AGL) to be attained using the CopterSonde, part of the 3D Mesonet project was to do preliminary studies to examine the potential improvement and impacts that a WxUAS network could have on Numerical Weather Predictions (NWP) [26]. For this, an Observation System Simulation Experiment (OSSE) was performed over the state of Oklahoma, assuming that 110 WxUAS stations were distributed and conducting atmospheric soundings with a desired flight cadence and maximum altitude. Four study cases, each of them with WxUAV flights up to 120 m, 1 km, 2 km, and 3 km AGL, respectively, were compared against the no-WxUAS flight study case. The study concluded that the addition of WxUAV flights up to 1 km was adequate to reliably resolve the vertical structure of the PBL, and flights up to 3 km were preferred when focusing on severe storm predictions [87].

For reference, Table 3.1 summarizes the desired variables to be observed using the CopterSonde with their respective target accuracy and operating ranges. It has to be mentioned that many of these desired goals were agreed upon by an informal consensus of atmospheric scientists, National Weather Service (NWS) staff, and other experts in the subject [21, 26]. The specifications of the thermo-hygrometers provided in this work already claim that such sensors almost fully meet the above-desired requirements (see Table 2.1 for comparison), provided that they are working within appropriate operating conditions. On that account, a goal of the CopterSonde design is to keep the onboard thermo-hygrometers working within a nominal regime and prevent unwanted sources of data contamination from interfering with the sensor measurements. Before even conceiving the first CopterSonde prototype, it was known that these problems could arise. Therefore, it was necessary to explore ways to provide adequate ventilation to the sensors, minimize the effects of solar radiation exposure, and make sure that the sensors were not being impacted by the effects of the UAV itself. However, not all

Table 3.1: Desired meteorological measurement specifications and operating range used as a reference for the CopterSonde design. Many of these desired targets were agreed upon by an informal consensus of atmospheric scientists, National Weather Service (NWS) staff, and other experts in the subject [21, 26].

Meteorological variables and accuracies

Parameter	Measurement accuracy
Temperature	± 0.2 °C
Relative humidity	± 5.0 %
Wind speed	± 0.5 m s^{-1}
Wind direction	± 5.0° azimuth
Sensor time response	$<$ 5 s (preferably $<$ 1 s)

Operational and environmental conditions

Parameter	Range
Temperature	-30 – 40 °C
Relative humidity	0 – 100 %
Max wind speed	0 – 35 m s^{-1}
Max altitude AGL	$\geq$ 1000 m

of these problems could be addressed immediately at the beginning of this work due to the initial low resources, lack of adequate facilities, and the high demand for quick solutions so that CASS could join and participate in scheduled field campaigns. Consequently, the CopterSonde design approach was initially taken in a provisional manner, where the first few field campaigns were primarily for identifying engineering challenges, testing solutions by trial and error, sharing experiences with other institutions, and making improvements based on empirical observations. From this point forward, the skills and techniques for design and construction significantly improved throughout the CopterSonde development years, which led to the formation of a robust engineering workflow.

Even though the initial research and development approaches were mainly attempts without much scientific support while also trying to find inspiration from existing solutions at the time [24, 25, 55], there were efforts in investigating some fundamental questions related to the integration of thermo-hygrometers into UAVs. Finding an adequate location for the weather sensors on the UAV was and remains one of the most debated topics among experts in the subject [23, 53, 88]. In an effort to help to address the problem, simple experiments to learn about the effects of the UAV on weather sensors were conducted at the Advanced Radar Research Center (ARRC) of the University of Oklahoma [89]. The tests were carried out in a reasonably homogeneous chamber to find optimal locations for the thermodynamic sensors clear of systematic biases. The sensors were gradually displaced under the rotor wash of a mounted multicopter UAV, as shown in Figure 3.1. This study concluded that when trying to monitor the ambient temperature with a standard multicopter UAV, there is no particular location under the propellers that guarantees contamination-free measurements. These types of platforms are prone to changing their own surrounding environments in unpredictable ways.

This led to a period of brainstorming and thinking about feasible solutions and roadmaps that could lead to improvements in the quality of the measurements using a multicopter UAV. In order to satisfy short-term and long-term goals, it was decided to take two different paths. For reasons explained above, the short-term solution involved assembling a UAS that could be mission-ready in a short time. This meant opting for a standard multicopter UAV design with a symmetrical distribution of weather sensors around the UAV. This design was known as the CopterSonde-1 shown in Figure 3.2 and was first fabricated in early 2017 using an ad hoc design structure. On the other hand, the long-term solution consisted of a richer list of desirable custom features on the UAV to meet the overarching goals of this work and start moving towards a fully integrated airborne weather instrument system.

For the long-term solution, a combination of desired interrelated features was envisioned primarily for reducing platform errors on thermodynamic observations of the atmosphere. The main one being the implementation of a wind tracking algorithm for

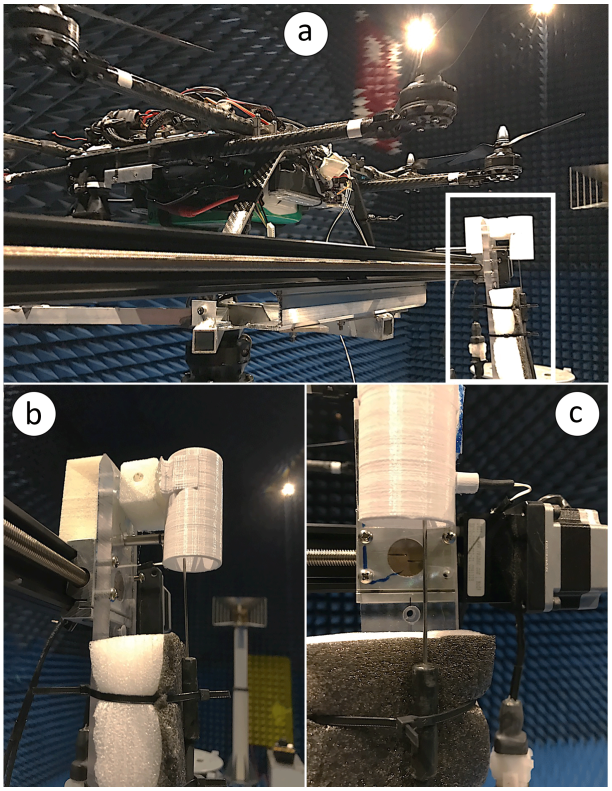

Figure 3.1: Experimental setup for evaluating temperature sensor location on a UAV. The test was conducted inside the anechoic chamber of the ARRC. (a) Position of the linear actuator arm below the rotors of the multicopter UAV mounted on a pedestal. The temperature probe is shown inside the white box. (b) Close-up side view of the temperature probe. (c) Close-up front view of the temperature probe and the actuator. Images were taken from [89].

the CopterSonde dubbed the wind vane flight mode (WVFM). This method would allow the CopterSonde to quickly estimate wind direction and continuously turn itself into the wind. The resultant orientation was initially thought of as a way to favor sampling undisturbed air, given that the sensors are placed at the most downwind section of the UAV body, which will be demonstrated further in the chapter. Consequently, this envisioning of features gave a first idea of arranging the internal components of the next CopterSonde iterations as shown in Figure 3.3. The elongated airframe facilitated positioning the UAS electronics behind the payload and effectively hide them

Figure 3.2: CopterSonde-1 concept made in early 2017. An octocopter UAV with temperature and humidity sensors distributed in a symmetrical arrangement around the UAV. The sensors were housed and protected inside plastic tubes and mounted on the UAV's arms below the rotors.

from the wind. The idea of having the payload located at the most downwind section of the CopterSonde would result in undisturbed air flowing across the weather sensors. Directly behind the sensors is the autopilot system for ease of wiring and connections, followed by the battery, which is the heaviest component in the CopterSonde. The battery was conveniently placed close to the center of mass of the CopterSonde, allowing for increased maneuverability and overall flight performance. Lastly, the communication system was placed on the other end of the airframe, far away from the electronics, in order to reduce potential RF interference.

The full list of additional features for the long-term solution is as follows:

1. Modular and interchangeable payload compartment for ease of calibration and maintenance purposes.

2. Solar shield and ventilation system to force air across the sensors and mitigate measurement errors caused by solar radiation and sensor self-heating, respectively.
3. Custom wireless data stream to the GCS for live monitoring of weather parameters and distribution of products.
4. Decision-making and adaptive behavior capabilities based on sensed environmental conditions to eliminate human errors and move toward a fully automated system.

Moreover, the shape of the enclosure (or shell) of the subsequent CopterSonde revisions drastically changed compared to the CopterSonde-1. The new shell design takes advantage of the aerodynamic benefits made possible by using the WVFM. To give the reader an idea of how the resultant UAV platform looks like, Figure 3.4 shows a close-up of the latest CopterSonde model produced in early 2022, dubbed the CopterSonde-3D.

Lastly, given that the CopterSonde must reach high altitudes to achieve the science goals, this also means that it must share the airspace with other crewed aircraft. The FAA must unavoidably intervene in this situation and set rules to deconflict air traffic and prevent accidents. Consequently, in addition to the above-mentioned requirements, the CopterSonde must carry navigation and anti-collision lights, communication links, and aircraft avoidance capabilities to fulfill current and future FAA rules. Nonetheless, predicting the amount of risk mitigation necessary to satisfy the FAA is challenging because regulations governing access to and operations in the National Airspace System (NAS) are constantly changing (see Appendix B).

With the presented context, the following sections are dedicated to describing the engineering solutions applied to the most recent CopterSonde model, the CopterSonde-

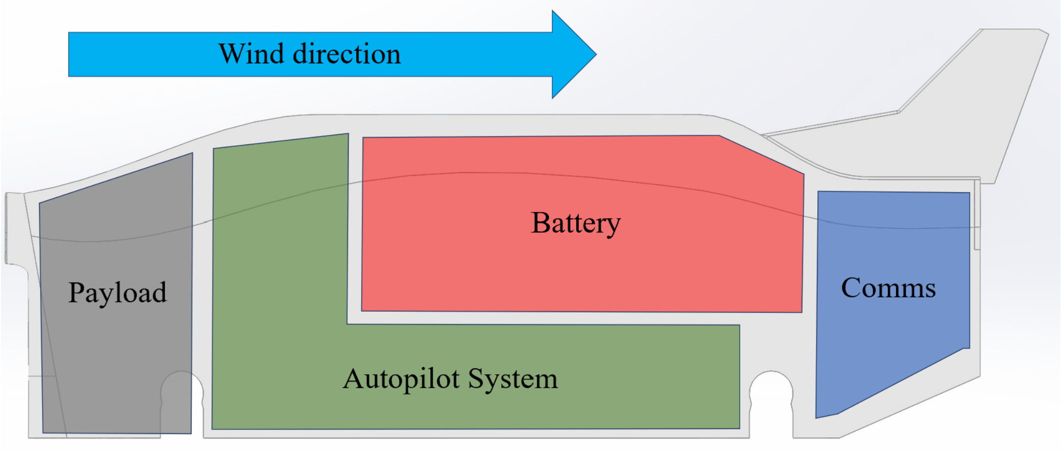

Figure 3.3: Illustration of the desired component distribution onboard the CopterSonde under the assumption that the system automatically orients itself into the wind by using a custom wind tracking function. The payload was located at the most downwind section of the CopterSonde, followed by the autopilot system for ease of connection. The battery was conveniently placed close to the center of gravity of the platform to increase maneuverability. The communication system was placed far away from the electronics to reduce potential RF interference.

3D. The proposed solutions aim to comply with the desired atmospheric measurement requirements and design constraints. From this point, the CopterSonde-1 is considered an unmodified standard UAS design re-purposed for weather sampling and used as a reference for comparisons in this study.

3.2 Autopilot System

The CopterSonde-3D is equipped with a Pixhawk CubeOrange autopilot board developed and manufactured by CubePilot company located in Moolap, Australia [90]. The Pixhawk is an open-hardware project that provides users with a readily available, economical, and high-end autopilot board solution for academic, hobby, and industrial communities. It contains a powerful ARM® STM32H7 Cortex®-M7 micro-controller capable of executing complex flight operations, including autonomous missions. Besides having a powerful microcontroller, it also comes with a redundancy of IMUs

Figure 3.4: CopterSonde-3D concept made in early 2022. A quadcopter UAV specifically designed to collect high-quality thermodynamic observations of the atmosphere. Its peculiar shape is due to the unique arrangement of internal components to improve airflow aspiration across the atmospheric sensors thanks to the addition of a wind vane function to the flight control system.

housed in a small form factor with a built-in temperature control system using heating resistors. This is ideal since the CopterSonde must be able to fly within a large temperature range without losing performance. The CubeOrange supports several communication protocols commonly found in off-the-shelf peripheral devices like I2C, SPI, UART, and CAN protocols. This way, the CubeOrange has access to a wide range of compatible devices that can be used for flight assistance or other desired applications. From the wide selection of compatible peripherals, the following list describes the chosen hardware for autopilot assistance. Although the listed components belong to the latest CopterSonde-3D design, this combination of components (ignoring the make and model) is a common factor among all the CopterSonde revisions. Therefore, it is considered to be the baseline for attitude control, flight stabilization, and navigation support of the CopterSonde.

1. Here3 Global Navigation Satellite System (GNSS) unit: The GNSS unit is a necessary component for outdoor flight navigation. It estimates and tracks the global positioning of the UAV using different satellite constellations (GPS, GLONASS, Beidou, etc.). The accuracy varies from 1 m to 3 m depending on the atmospheric and space weather conditions. However, if desired, the Here3 GNSS is capable of estimating position in the order of a few centimeters. This can be enabled using supplementary ground-base GNSS for real-time kinematic (RTK) corrections. The Here3 GNSS unit also comes with a magnetic compass that measures the heading of the CopterSonde with respect to True North.

2. Lightware LW20/C range finder: The range finder is placed on the CopterSonde, pointing downwards, continuously measuring the distance to the ground. This component helps the autopilot to estimate altitude with higher accuracy in the order of a few centimeters up to 120 m. Besides assisting the autopilot in detecting the ground for autonomous take-off and landing, it allows for precise altitude lock when required. For instance, the range finder prevents the CopterSonde from experiencing unwanted altitude variations when hovering by a meteorological tower.

3. RFD900X telemetry radio (915 MHz): this long-range ISM band radio modem can hold a stable link up to 5 km in ideal weather conditions using the default antennas. The autopilot uses the radio modem to exchange flight parameters and commands with its paired radio located at the GCS.

4. FrSky RX4R radio control (2.4 GHz): this small-size radio receiver is used to

fully control the UAV through the operator's inputs. The extra communication channel provides link redundancy to the UAS. The FrSky radio is paired with a hand-held radio with joysticks, switches, and a monitor that allows the operator to manually maneuver the UAV, switch flight modes, and monitor flight parameters.

5. mRo Zero power module: the main power distribution board for all the devices onboard the CopterSonde. It can precisely measure voltage and current through its hall effect sensor for power consumption estimation.
6. Buzzer: the speaker produces audible errors, warnings, and other information about the status of the UAV to immediately alert the operators during flight operations.

Figure 3.5 shows the hardware arrangement of the CopterSonde-3D with their respective connections to the Pixhawk CubeOrange microcontroller.

The Pixhawk CubeOrange board runs the ArduPilot autopilot code [91], which is one of the most popular free software autopilot packages that can be modified and redistributed under the terms of the GNU General Public License version 3 (GPLv3). This means anyone is free to use all of the provided code and tools available online on the ArduPilot Github repository without authorization or involvement from the ArduPilot team. However, it is the responsibility of anyone using the code to inform the end-user that open-source software was used, and the source must be provided. Therefore, in accordance with ArduPilot's GPLv3 license, the code source history and release made during the development of the CopterSonde series are accessible to the users in [92]. Besides this, given that the ArduPilot repository is managed by a code hosting platform for version control and collaboration (GitHub), this means that the official releases from ArduPilot can be easily tracked and merged to the cloned code on CASS's repository.

This feature allows developers to continue harnessing the power of the ArduPilot code for future integration and optimizations for any desired application.

The motivation behind the decision to modify an existing open-source autopilot code was the flexibility of incorporating additional desired features and not depending on proprietary codes from companies, which do not usually follow the same research lines and are prone to become discontinued. By having full access to the UAS's autopilot code and being able to modify it as desired, it facilitates the integration of custom functions and extra data handling through a single processing unit. Consequently, it enabled the confluence of weather data with flight data allowing for the creation of algorithms that exploit the merging of new information. For instance, the development of adaptive flight behaviors such as onboard wind estimation to command the autopilot to turn the UAV into the wind. Also, separate data loggers are no longer needed for weather sensors, as the CubeOrange autopilot board has sufficient computing power to accommodate the extra data and transmit it to the GCS. This also came with the benefit of weight reduction, which is crucial for improving flight performance and endurance.

The post-CopterSonde-1 models exploited the open-source capabilities of the Pixhawk and ArduPilot the most, which led to the final CopterSonde-3D revision after successive code improvements and the addition of custom features. On the other hand, the CopterSonde-1's autopilot code was not modified whatsoever, and it used the original ArduPilot code instead. As opposed to the CopterSonde-3D, the data from the weather sensors were recorded using an external data logger and broadcast to the GCS with a separate radio transmitter.

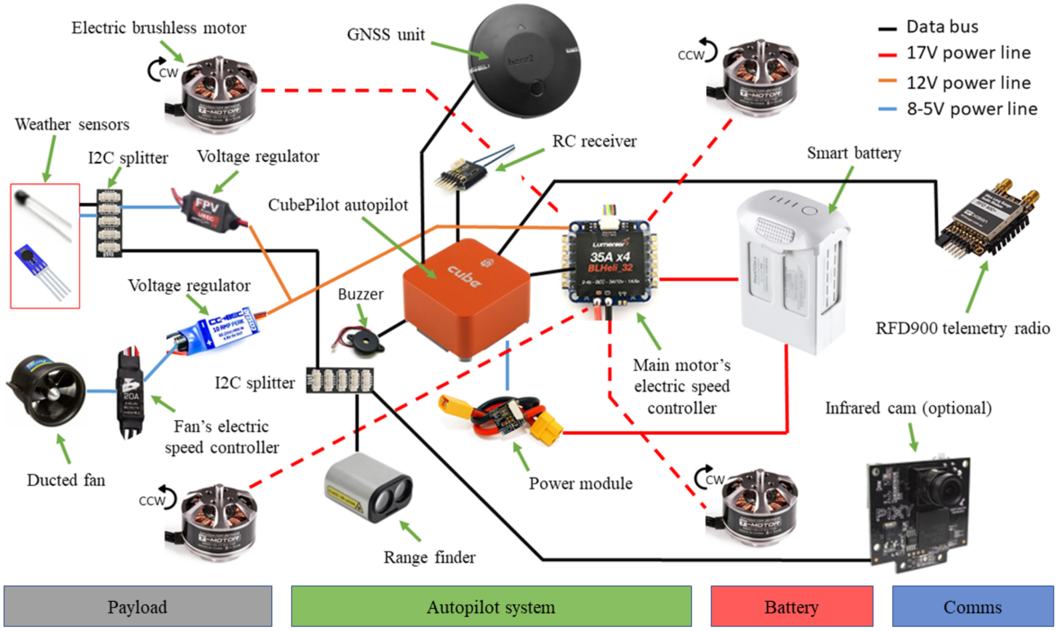

Figure 3.5: Schematic of the electronic components onboard the CopterSonde-3D. It shows how the different devices are connected and powered. The location of the components follows the proposed concept shown in Figure 3.3.

3.2.1 Custom Feature Integration and Benchtesting

Even though the Pixhawk and peripherals have communication protocols in common, the original ArduPilot code does not have the code libraries to read the meteorological sensors used in this work, nor the features that were thought could help enhance weather sampling. Therefore, the ArduPilot code had to undergo modifications to incorporate custom sensor drivers and functions to adapt it to the desired weather sampling application. Nonetheless, code modification is not a trivial process, and extreme care must be taken when manipulating functions and algorithms related to the flight system of the UAS. On top of this, running and testing experimental code directly on the intended hardware is a dangerous task, particularly when the hardware is a flying device. In general, UAVs carry great momentum and gravitational potential when flying, and hence, crashing the UAV can result in severe airframe damage. This could, consequently, trigger tedious and expensive repairs, which is not economically sustainable in the long term.

To avoid these scenarios, ArduPilot's software-in-the-loop (SITL) simulator was used for code debugging and testing. SITL allows developers to run a build of the autopilot code using ordinary C++ compilers on a computer, producing a native executable where the developer can visualize the expected behavior of the UAV with the new functions. The sensor data in SITL originates from a built-in flight dynamics model with adjustable parameters to approximately match those of the real UAV. SITL also comes with a very simple atmospheric environment simulation to visualize the effects of wind and turbulence on the virtual UAV. In addition, SITL provides access to a large set of development tools available for C++ programming, including interactive debuggers, static analyzers, and dynamic analysis tools [91]. This simplified the development and testing of custom ArduPilot features without running extensive tests in the field.

The introduction of SITL simulation environment and related programming tools was a tipping point in the development of the CopterSonde that drastically changed post-CopterSonde-1 design process. As a result, this allowed for the subsequent CopterSonde iterations to be thoroughly planned in advance and gradually trend away from the ad hoc design structure. From this point onward, it was not necessary to fully produce and assemble the UAV hardware beforehand, as was the case with the CopterSonde-1. Instead, SITL helped verify that the desired software function was feasible before adopting the new hardware concept. After the evaluations using SITL, the new hardware/software combination was tested in the field to determine its overall effectiveness and identify real-world problems to be addressed in the following design iteration. Figure 3.6 shows a diagram of the steps taken to integrate custom hardware and software into the CopterSonde.

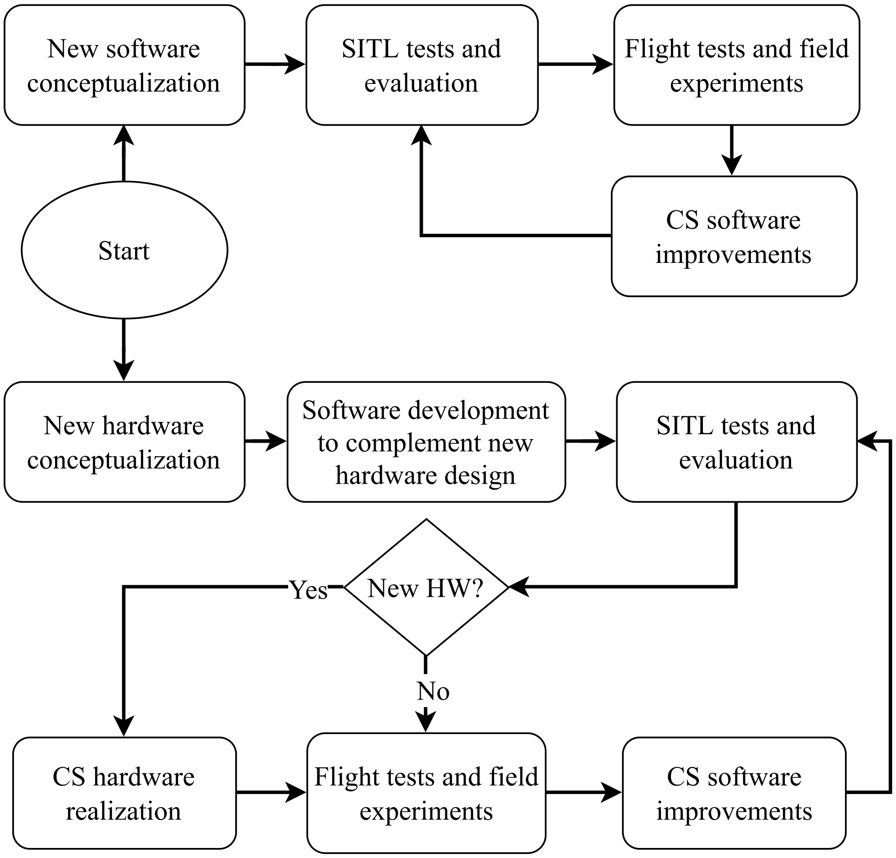

Figure 3.6: CopterSonde engineering design workflow that was formed after the CopterSonde-1 generation and adopted for new hardware and code integration with subsequent iteration loops.

3.2.2 Code Integration Examples

The current version of the CASS-ArduPilot code executed by the latest CopterSonde-3D can be found in [92], where the reader can learn about the full history of code modifications and releases. Custom code functions were added on top of the original ArduPilot code and tested following the integration process described in the previous section (Figure 3.6). The additional functions are itemized below with their motivation and description as follows.

Weather sensor integration: C++ code libraries were incorporated into the autopilot code to read the iMet-XF bead thermistors and IST HYT-271 humidity sensors. The datasheet of each sensor comes with a detailed description of the binary language used to exchange information over I2C communication protocol. As a result, the CopterSonde is capable of handling the extra data from the weather sensors and storing it in the onboard SD card along with the flight data. A total of eight I2C addresses or slots were reserved for this type of weather sensor in case of future expansions. Tests were conducted to determine if the additional peripherals would impact the computational performance of the Pixhawk; however, the built-in task manager in ArduPilot showed no noticeable increase in system load.

Custom sensor message for wireless streaming: Given that the autopilot software is internally handling the weather data, it is advantageous to also include it in the data stream that is sent to the GCS through the onboard telemetry radio. ArduPilot encodes the message packets using the Micro Air Vehicle Link (MAVLink); a light messaging protocol specifically meant for long-range UAS operations. A custom message definition was added to the list of MAVLink messages in ArduPilot (Table 3.2) with special fields to tag the type and size of the measurement being sent. This means that the proposed message definition can be re-used several times to transmit different types of sensor measurements without conflict. This enabled remote monitoring of weather sensor data in real-time while in flight.

Wind vane flight mode: A wind vane function was not available as part of the original ArduPilot autopilot when the CopterSonde was first used in 2017. However, it was known from the beginning that this was a crucial function in order to get the CopterSonde hardware concept working within the desired operating window. Therefore, a custom wind tracker, the WVFM, was developed and implemented on the ArduPilot code. The method works by taking and filtering a few elements of the attitude's rotation matrix to produce a “tilt” vector from which the wind speed and direction can be computed. A more detailed mathematical derivation of the WVFM can be found in

Table 3.2: Custom MAVLink message definition in XML language that was added to the wireless data stream of the CopterSonde. It has two special fields to identify the size and type of measurement being sent. Therefore, this message definition can be used for several types of sensors simultaneously.

```
<!-- CASS Mavlink Message -->
   <message id="227" name="CASS_SENSOR_RAW">
     <description>Contains raw sensor data for CASS
        application.</description>
     <field type="uint32_t" name="time_boot_ms">Timestamp (
        milliseconds since system boot)</field>
     <field type="uint8_t" name="app_datatype">Data type
        indicating what data is being sent. 0 = iMet temp, 1
         = RH, 2 = temps from RH, 3 = wind data</field>
     <field type="uint8_t" name="app_datalength">Length of
        raw data array</field>
     <field type="float[5]" name="values">Raw data</field>
   </message>
```

the following chapter. For the WVFM to work correctly, the CopterSonde must stay horizontally stationary while compensating for wind by leaning towards it. This guarantees that the tilt vector is produced only by the effects of wind and not by intentional displacements of the CopterSonde. Therefore, the CopterSonde is limited to vertical profiling or hovering flights.

High wind failsafe: It is not convenient to rely solely on the operator to judge the severity of winds affecting the CopterSonde. This is because the CopterSonde will be flying at high altitudes where the wind may be significantly different than where the human operator is located. Based on the telemetry data, different operators may perceive the effects of wind on the CopterSonde differently. Therefore, having the capacity to estimate wind speed internally, a logical function was included on the autopilot to constantly assess wind conditions around the platform. If the threshold is breached, the CopterSonde will immediately alert the operator about it, abort the flight, and initiate the landing sequence. If desired, the operator can override the failsafe and continue with the mission.

Battery charge level and range failsafe: Although the Pixhawk and ArduPilot come with hardware and functions to estimate the energy drawn from the battery, it does not have a way to determine if the remaining energy is enough to return home safely and land. Moreover, the range estimation depends on the wind conditions since the CopterSonde must use more power to compensate for wind. Again, this represents a difficult task for the operator to calculate, judge, and take action in a timely manner. For this reason, the range estimation has been automatized by introducing a method to compute the energy needed to descend and land the CopterSonde from a given height safely. The method takes into account the wind profile measured throughout the vertical sounding, and it triggers the failsafe once it reaches a defined threshold. The threshold was determined by trial and error after several flight tests in extreme wind conditions.

Automatic waypoint mission generator: Knowing that the desired main flight path for the CopterSonde is a vertical profile (or straight vertical line), it was convenient to make the process of generating the waypoint mission automatic. At the flip of a switch from the GCS, the CopterSonde registers its current location and uses it to create a waypoint directly over the platform at an altitude previously defined by the operator. This user-friendly method prevents the operator from spending valuable time manually creating the mission and potentially introducing human errors.

Smart fan for sensor aspiration: Given that the chosen weather sensors must have constant air flowing across them, there is a high risk that their delicate structures get damaged by dust and debris. In general, the CopterSonde encounters small particles floating in the air close to the ground that were blown off by propeller wash or wind. A small code to control the sensor fan was added to the autopilot code as a solution to this. It toggles the fan's power at defined heights after take-off and before landing, reducing the chances of permanently damaging the sensors and increasing their lifespan.

3.3 CopterSonde Airframe

3.3.1 Frame Selection

In 2017, propulsion redundancy was a priority in the design of the CopterSonde-1 because there was doubt about the quality and reliability of the chosen off-the-shelf electronics. For this reason, the CopterSonde-1 took the shape of an easy-to-assemble "hashtag" octocopter UAV which has the ability to stay in the air even with one motor failure. The CopterSonde-1 frame is not commercially available, and it was made entirely in-house by CASS engineers using carbon fiber rods and plates fastened together with aluminum clamps. The CopterSonde-1 had a total of eight rotors, each one attached to one end of the hashtag frame. The hashtag-shaped airframe facilitated the mounting of a flat plate in the center of the frame, where the battery, sensors, and autopilot system were placed in a symmetrical and centralized manner. The electronics were covered and protected with a pyramid-shaped aluminum enclosure. The CopterSonde-1 was extremely large and bulky compared to the size and weight of its payload. The CopterSonde-1 spent most of its propulsion power on staying aloft, and, therefore, it had to use large and expensive batteries to compensate for the loss of flight time. Table 3.3 sums up the specifications of the CopterSonde-1 airframe, and Figure 3.7 shows the top, front, and isometric views of the computer-aided design (CAD) model.

On the contrary, a different airframe design approach was taken for the CopterSonde-3D, where simplicity and economy formed part of the priorities. As time passed, new and more reliable components hit the UAS market, which led to removing redundant hardware from the CopterSonde. During the selection of the new airframe in late 2017, the CASS team was preparing for a field campaign in Hailuoto, Finland. This imposed a strict requirement for the size of the new CopterSonde so that it could be fitted inside a container for air travel. Besides this, a highly modular airframe was

Table 3.3: Technical specifications of CopterSonde-1 (CS1) airframe. The CopterSonde-1 frame is not commercially available, and it was made entirely in-house by CASS engineers using carbon fiber rods and plates fastened together with aluminum clamps. The CopterSonde-1 had a total of eight rotors, each one attached to one end of the hashtag structure.

CS1 airframe	
Type	Rotary-wing octocopter UAV
Materials	Aluminum and Carbon fiber
Layout configuration	Hashtag
Dimensions	710×710×250 mm
All-up weight	7 kg
Payload weight	450 gr

also thought convenient to allow for design scalability for future iterations. For this reason, the commercially available Lynxmotion HQuad500 (LHQ500) quadcopter airframe [93] was selected (Figure 3.8). The default LHQ500 setup was meant for long-range flights able to carry a small action camera, like a GoPro Hero camera, with a small gimbal stabilizer system. This camera payload is similar in weight to the weather sensor payload used in the CopterSonde-1. Therefore, the weather sensor package developed for the CopterSonde-1 falls within the weight tolerance of the LHQ500, making it a suitable airframe candidate. Similar to the CopterSonde-1, the LHQ500 consists of carbon fiber rods, fiberglass plates, and aluminum clamps. However, the LHQ500 is an elongated H-shape airframe that comes with three different plate heights. This gives more room to arrange the hardware and comply with the initial desired electronic distribution requirements (see Figure 3.3 for reference). Table 3.4 shows a summary of the airframe specifications of the CopterSonde-3D.

A few structural modifications were made to the LHQ500 airframe to accommodate some of the electronics. Besides purchasing commercially available parts, CASS had access to 3D printers using polylactic acid (PLA) material to produce custom parts. These additional parts were designed using SolidWorks® CAD software. The texture

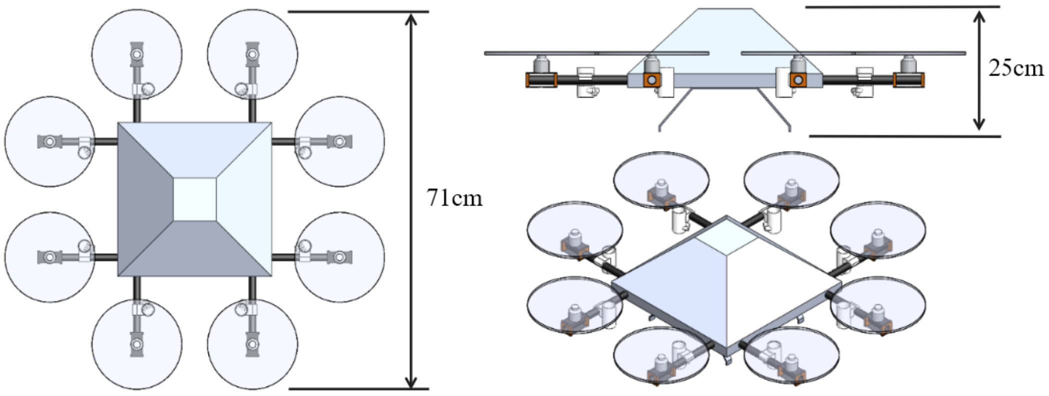

Figure 3.7: Top view (left), front view (top-right), and isometric view (bottom-right) of the CAD model of the CopterSonde-1 showing the hashtag octocopter layout with dimensions. The symmetric distribution of the weather sensors is visible around the main body as little white tubes below the rotors. Model and images were generated using SolidWorks® from Dassault Systèmes Corporation.

quality and strength of the 3D-printed parts were acceptable for fast prototyping, but it is not typically seen in UAS with industrial-grade standards. Figure 3.9 shows the structural modifications, including the fabricated 3D-printed parts. Originally, the main battery goes in between the top and middle plate of the LHQ500, and it is installed by sliding it horizontally. However, the 3D Mesonet project required the CopterSonde-3D's battery to be installed and removed vertically from the top. This is because the 3D Mesonet included the construction of an automated UAV launch box with a built-in crane for battery swapping. Therefore, a hole was made in the top and middle plates of the LHQ500 airframe to fit the battery vertically. A 3D-printed base was made to hold the battery from the bottom, which is also where the battery connects to the power distribution system. Given that such holes may weaken the structure, the middle plate was reinforced by adding an extra 3D-printed layer. Lastly, 3D-printed mount support for the range finder was made to keep the range finder in a fixed position pointing downwards.

Figure 3.8: Lynxmotion HQuad500 (LHQ500) is a commercially available quadcopter airframe that was selected for the main structure of CopterSonde revisions. The LHQ500 consists of carbon fiber rods, aluminum clamps, and 3 different height levels of fiberglass plates that are highly customizable [93].

3.3.2 Design and Construction of the Shell

In general, the most wanted weather observations are during harsh atmospheric conditions, which are usually associated with precipitation, high wind, and freezing temperatures. This means that the CopterSonde must be able to endure and withstand challenging environments as much as possible while flying. The primary shield protecting the internals of the CopterSonde against extreme weather conditions is the shell. The shell of the CopterSonde covers the main body of the airframe leaving only the arms and rotors exposed to the environment. In general, the most worrying hazards are water drops and flying particles hitting the CopterSonde from the top and sides. This is well protected by the shell; however, the shell does not cover the bottom of the platform. This leaves the bottom and internals of the CopterSonde exposed to advecting moisture from the air and ground. A solution was to coat the electronics with a silicone film to prevent moisture from potentially short-circuiting the board.

As described earlier in this chapter, the CopterSonde-1 had a shell shaped like a pyramid and made of aluminum. Aluminum was chosen because folding a flat sheet

Table 3.4: Technical specifications of CopterSonde-3D (CS3D) airframe. The commercially-available LHQ500 quadcopter airframe [93] was selected. The LHQ500 is an elongated H-shape airframe made of carbon fiber rods, fiberglass plates, and aluminum clamps.

CS3D airframe	
Type	Rotary-wing quadcopter UAV
Materials	Aluminum, carbon fiber, PLA
Layout configuration	H-shape
Dimensions	300×390×152 mm
All-up weight	2 kg
Payload weight	205 gr

into a pyramid was not a complicated task. However, this added unnecessary weight to the CopterSonde-1, knowing that other lighter materials could be used. On the other hand, the CopterSonde-3D has a more elaborated shell design (Figure 3.10), and its fabrication was possible thanks to the acquisition of 3D printers and CAD software. Digital 3D models of the shell and flow simulations were produced using SolidWorks® CAD software. Taking advantage of the WVFM function, the CopterSonde-3D shell was designed to have less resistance to the air when pointing into the wind. This allowed the CopterSonde-3D to achieve higher speeds while also reducing power consumption. The vertical fin on the CopterSonde-3D is there to increase the side surface. As a result, the resistance to the air on the side of the CopterSonde-3D is greater, increasing the sensitivity of the WVFM for better response.

The CopterSonde-3D shell was made modular and versatile, particularly the payload section. The payload has its own detachable compartment capable of operating independently from the main body of the CopterSonde-3D. This feature is particularly useful for calibration and maintenance purposes. As a consequence, the CopterSonde-3D shell was divided into two pieces: the front shell and the back shell, as shown in Figure 3.11. The back shell supports the vertical fin and holds the battery using latches.

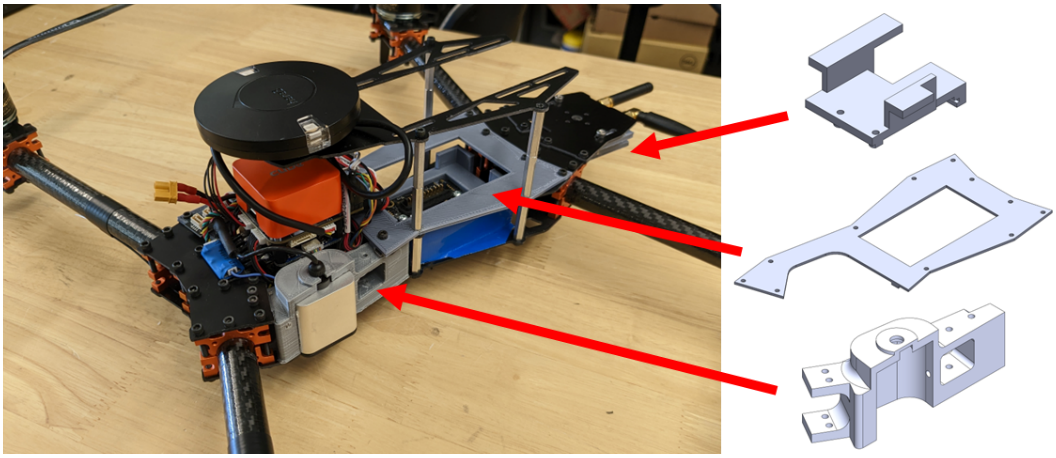

Figure 3.9: Illustration of the modifications made on the LHQ500 airframe to accommodate all the necessary electronics of the CopterSonde-3D, including the fabricated 3D-printed parts shown on the right side. From top to bottom, the parts shown here are the telemetry radio mount, reinforcement plate, and lidar mount. The shown parts are not to scale.

Whereas the sensor compartment is located in the front shell of the CopterSonde-3D. The front shell is exchangeable, which gives the option of having a variety of front shells with different sensor configurations for a broad range of experiments. The construction and testing of a different front shell and sensor package have not been done, but it is feasible as long as the payload weight and size are similar to the original front shell. The dimensions of the compartment are approximately 100×95×70 mm and can carry a maximum payload weight of 205 gr and a minimum of 90 gr (not including the shell). The CopterSonde's center of gravity (CG) without the whole shell is slightly rear-shifted with respect to its center. Under the minimum payload weight configuration, the CG is located at the center of the CopterSonde-3D, whereas the CG is slightly forward under the maximum payload weight configuration. None of these configurations seem to compromise the CopterSonde-3D's stability or performance to any noticeable degree.

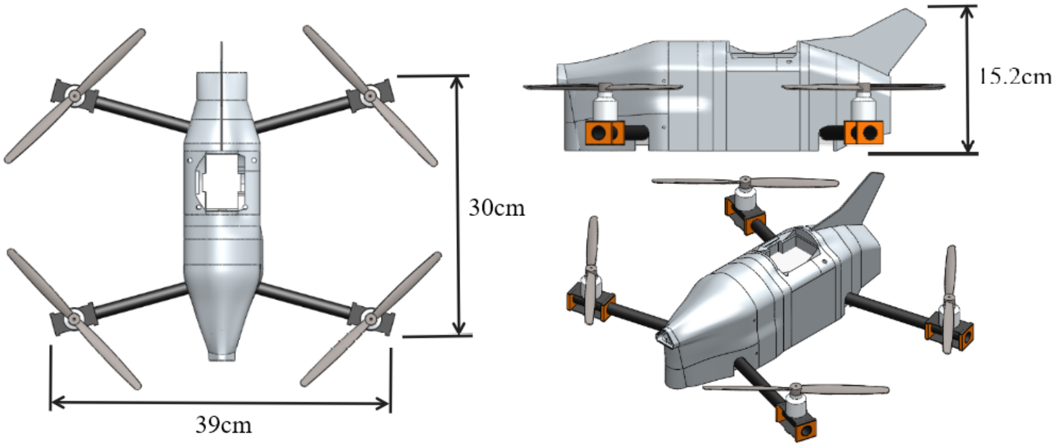

Figure 3.10: Top view (left), front view (top-right), and isometric view (bottom-right) of the CAD model of the CopterSonde-3D with dimensions. Model and images generated using SolidWorks® from Dassault Systèmes Corporation.

3.4 Propulsion System

The propulsion system of the CopterSonde consists of propellers, electric brushless motors, electronic speed controllers (ESC), and a power source. Different combinations of these elements produce a wide variety of configurations that involves a trade-off primarily between flight speed and flight endurance. These two qualities were necessary to be maximized on the CopterSonde, given that it needed to reach high altitudes while enduring high winds. However, it was decided to lean more towards top speed to give the CopterSonde-3D sufficient power headroom when fighting against extreme wind gusts.

In general, the design of the propulsion system starts with the propeller selection using the desired airframe configuration and other estimated specifications as constraints. Propellers are mechanical devices that convert rotational motion into linear force or thrust. Multicopter propellers produce lift for the aircraft by spinning and producing airflow, resulting in a pressure differential between the propeller's top and bottom surfaces. This accelerates the mass of air in one direction, creating lift that counteracts the

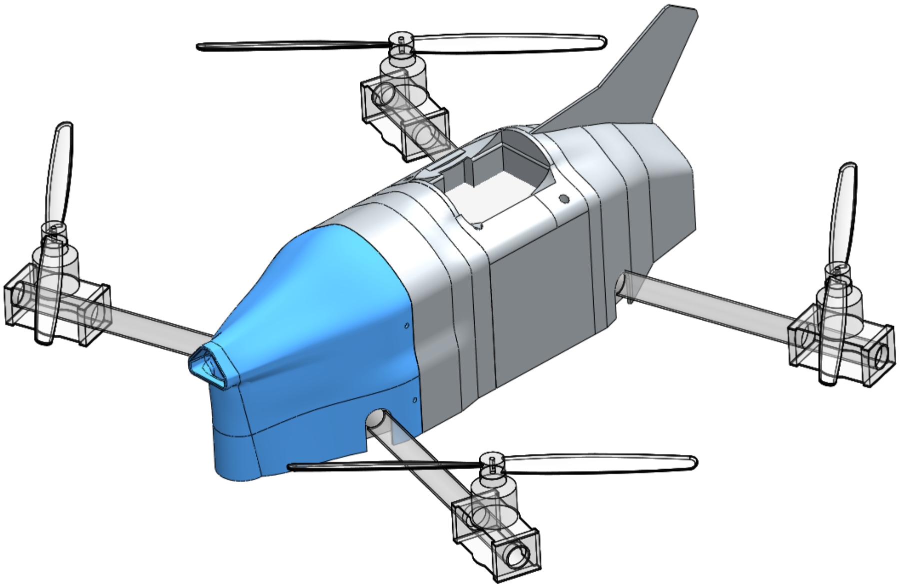

Figure 3.11: View of the CopterSonde-3D highlighting the 3D printed front shell (solid blue) where the weather sensor package is located, and the back shell (solid gray) that holds the battery and vertical fin. The arms were made transparent in the image to distinguish them from the shell.

force of gravity. There are three main design parameters for the selection of propellers which are as follows:

1. Blade configuration: This refers to the number of individual blades on the propeller and their shape. A higher number of blades usually correlates to higher thrust, but it also comes with higher aerodynamic drag and power consumption. If the propeller has dimension constraints, increasing the number of blades is an alternative to increasing the diameter. The shape of the propeller is all about extracting maximum efficiency, and there is a wide variety of concepts in the market. The most commonly known are APC, T-style, Slow-Flyer, Tapered, Bullnose, and others.

2. Propeller diameter: This is the diameter of the circumference swept by the tip of the propeller with the center on the hub of the propeller. A larger diameter means

a larger circumference area and, thus, a larger air volume is displaced. Disk loading is a way to measure the lift thrust efficiency equal to the ratio between the UAV weight and the circumference area. However, the maximum diameter is limited by the physical dimensions of the UAV and the motor's specifications.

3. Propeller pitch: The pitch is the propeller's theoretical traveling distance in one complete revolution, measured in inches. High pitch increases top speed, but excessive pitch can stall the propeller and lose performance. Low pitch increases efficiency and, thus, flight endurance at the expense of top speed. For multicopters, in general, the propeller pitch is fixed, and it cannot be changed during flight. Propellers are generally balanced and tested during the manufacturing stage for a specific operating range.

The electric brushless motors are the only actuator and moving part in the CopterSonde. The general design rule is to choose a motor capable of keeping the propeller within its optimal operating range without overheating under extreme loads. The ESC controls the voltage supplied from the battery to the motor to adjust the speed of the propeller. The right signal is given to the ESC by the drone's flight controller, which depends on inputs from either the human pilot's controller or the autopilot, as well as information from an IMU, GPS, range finder, and other peripherals. The ESC uses pulse width modulation to transmit the desired power to the motors, and thus, it must be able to do it synchronously based on the speed of the motor. Although the ESC can adjust the timing automatically, the range of compatible motors is limited, and care must be taken when selecting them. If the ESC is not selected correctly, it can become a power bottleneck and limit the overall performance of the rotor. Lastly, the battery is a critical component that must have a high energy density, low weight, and be capable of delivering high power to the motors when required. The main parameters of

Figure 3.12: Flight performance and efficiency predictions of the CopterSonde-3D using the online Ecalc calculator tool. Each gauge indicates the predicted operating range for the given parameter, where the colors represent levels of risk. Green is ideal, yellow is acceptable, and red is inadequate and may produce unwanted results. Image was taken from Ecalc [94].

the battery are cell chemistry, nominal voltage, energy capacity, and C rate. The C rate is a measure of the maximum continuous electrical current that the battery can safely supply.

In the UAS market exists a large number of propellers with pre-defined combinations of these design parameters from which the users can choose. The manufacturer usually provides a table of performance data showing the thrust and torque produced by the propeller at different speeds [95]. Furthermore, there is an online multi-platform UAV calculator, known as Ecalc, that has an extensive list of propulsion components that can be found in the UAS market [94]. The developers of Ecalc claim that its accuracy is ±15 % in estimating the propulsion performance of the desired combination of elements. It outputs estimations of power consumption, temperature, and thrust efficiency for typical scenarios like hovering, forward, and ascent flight. Besides selecting the desired propulsion combination, Ecalc requires a few other input parameters that must be known beforehand, such as all-up weight, motor layout, and dimensions. However, these parameters are usually unknown when designing a UAV for the first time. In particular, it is difficult to make an initial guess of the all-up weight because different propulsion, payload, and other custom arrangements may change it significantly.

Therefore, the expected performance of the first CopterSonde design was actually unknown until it was constructed. The subsequent CopterSonde designs had more prior information for the performance estimation based on what was learned from previous iterations. For example, the CopterSonde after the CopterSonde-1, dubbed the CopterSonde-2, was fabricated without much knowledge of its expected performance. The CopterSonde-2 had a weight of 2.5 kg, and even though the CS2 was flyable, the propulsion system was noticeably underpowered. Later, the CopterSonde-2.5 had a power unit improvement and a weight reduction to 2.3 kg thanks to improved building techniques. However, the CopterSonde-2.5 motors turned out to be unnecessarily bulky with excessive cooling material, thus, operating outside its optimal range. Lastly, the CopterSonde-3D had a weight of 2 kg with a propulsion system that gave a balanced compromise between UAV weight, motor temperature, thrust efficiency, and flight endurance. Figure 3.12 shows the predicted CopterSonde-3D performance plots generated using Ecalc. The selected propulsion components are listed in Table 3.5, and airframe specifications are described in Section 3.3.1.

3.5 Thermodynamic Sensor Package Design

Acquiring precise measurements of the air temperature and humidity is particularly challenging due to uncertainties arising from multiple sources around the UAS. Insuf-

Table 3.5: List of selected propulsion components for the CopterSonde-3D (CS3D). These components were chosen based on performance estimations calculated using Ecalc [94].

CS3D propulsion components	
Battery	DJI PH4 HV-Lipo 5870 mAh – 45 C – 4 S
ESC	Lumenier 32 bit 35 A 4-in-1 BLHeli_32
Motor	T-Motor Brushless MN3110-780
Propeller	T-Motor Carbon Fiber 11×5.5 in

ficient radiation shielding, exposure to mixed turbulent air from the propellers, and electronic self-heating are the main factors contributing to temperature, and humidity data contamination [42, 53, 89]. In this section, a complete description and some performance indicators of the current thermodynamic sensor package of the latest CopterSonde revision, the CopterSonde-3D, are presented. As a reference to visualize the advantages of the CopterSonde-3D design, the sensor package concept of the CopterSonde-1 is also briefly described and treated as a standard UAV without heavy modifications for weather sampling. The CopterSonde-1 was designed to carry four iMet-XF thermistors and four HYT-271 humidity sensors symmetrically distributed around the main body of the CopterSonde-1 (see Figure 3.2). A symmetrical sensor layout was chosen because the chances of measurement contamination by heat advection from the CopterSonde-1 body are high regardless of the wind direction. A symmetrical sensor distribution made it possible to discard the sensors located downwind of the CopterSonde-1 main body. However, this reduces the number of effective measurements while the sensors become useless passengers. Each sensor was mounted on one arm inside cylindrical plastic solar shields below the propellers. The location of the sensors underneath the propellers was determined based on considerations from [89].

On the other hand, the CopterSonde-3D's front shell was outfitted with a set of three iMet-XF thermistors and three HYT-271 humidity sensors to guarantee redundancy of

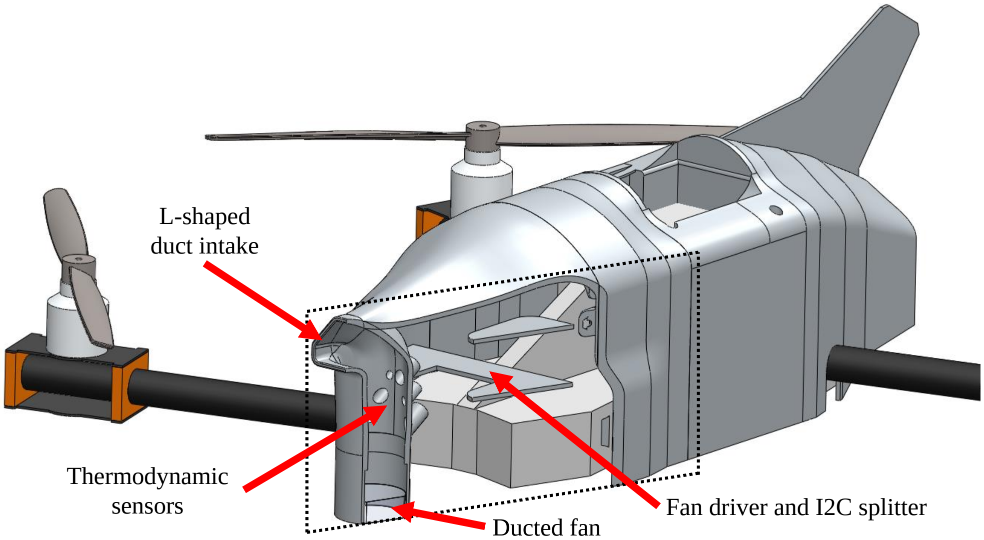

Figure 3.13: Section-cut of the front shell of the CopterSonde-3D CAD model illustrating the solar shield and compartment design, in addition to the location of the thermodynamic sensors and other components relevant to the sensor package. the dotted rectangle represents the plane of the cut made to the shell.

thermodynamic sampling, thus reducing measurement error and potential down-time. As opposed to the CopterSonde-1, the thermodynamic sensors of the CopterSonde-3D were all situated closely together at one particular location inside the front shell in order to approximately sample the same volume of air. Figure 3.13 shows the location of the weather sensors inside the duct and other components relevant to the sensor package incorporated into the front shell. The sensors were placed in an inverted “V” shape pattern to prevent the sensors from sampling heated and disturbed air produced by the wake and self-heating of the upstream sensors. The intake of the duct was molded into an inverted “L” shape with the intention of hiding the sensors from solar radiation as much as possible. This design resembles a scoop and, hence, is nicknamed after it. It was also considered to boss-extrude the intake away from the main body of the UAS and draw air outside the turbulent air created by the CopterSonde-3D. However, there were concerns that such a design could increase the resistance to rotation and exposure to strong aerodynamic forces that could produce flight instability. In this case, priority was given to flight stability over the quality of air samples. Therefore, the scoop intake was kept short and close to the CopterSonde-3D body. A small ducted fan was installed on the other end of the scoop to force air inside the duct and across the sensors. The fan was calibrated to draw air across the sensors at a constant speed of 10 m s^{-1}. The autopilot was programmed to automatically toggle the fan's power on and off after takeoff and before landing, respectively, to protect the sensors from dust close to the ground. The electronics of the front shell were connected to the main body of the CopterSonde-3D through 3 different cables: a power supply, a command signal for the ducted fan, and an I2C bus for sensor configuration and data logging. The front shell can be easily detached from the CopterSonde-3D and run separately for testing and calibration purposes, provided that an external power source and data logger are used.

3.5.1 Flow Simulation Analysis

To assess and compare the performances of these two sensor placement concepts, a series of parametric flow simulation analyses were conducted using SolidWorks® CAD software. The simulation aimed to measure the spread in temperature measurements of the sensors mounted on the UAS. Inside the simulated environment, this discrepancy was expected to result from heat being advected from the main body of the CopterSonde and across the sensor. Solar radiation was not included since, at the time of the experiments, it was not supported in the simulation software. The method used to determine the spread in the measurements among the sensors was by computing the mean of the absolute differences (MAD). For instance, the CopterSonde-3D has three

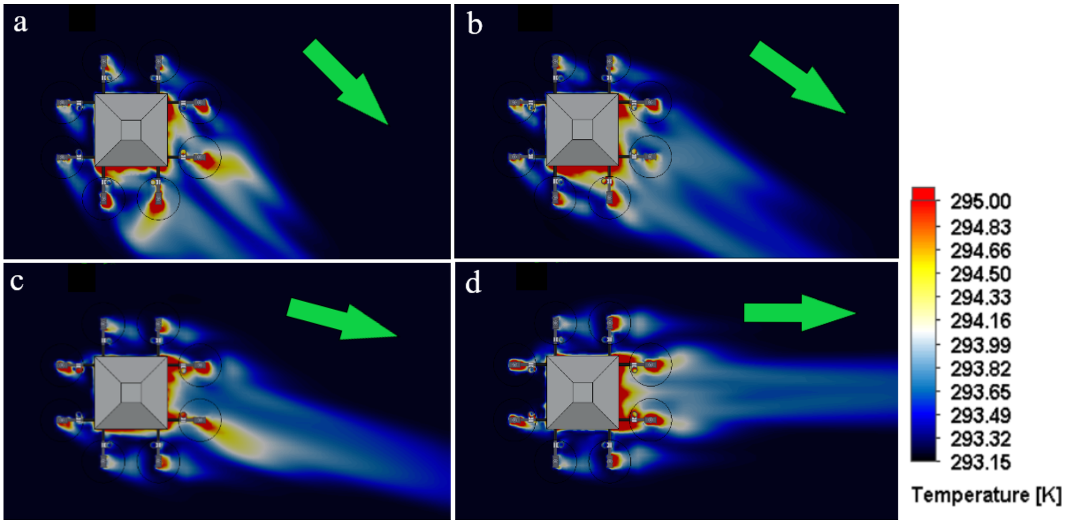

Figure 3.14: Color-map plots of air temperature distribution around the CopterSonde-1 model result of flow simulations using SolidWorks® CAD software. The shell and each motor were defined as the main sources of heat. The simulation did not include the effects of solar radiation. Different wind incidence angles, (a): 45 deg, (b): 30 deg, (c): 15 deg, and (d): 0 deg, were tested to visualize the effects of heat advection on the thermodynamic sensor using a standard UAV design.

temperature sensors and, therefore, the MAD equation is given by,

$$\text{MAD} = \frac{|T_1 - T_2| + |T_1 - T_3| + |T_2 - T_3|}{3} \tag{3.1}$$

where T_1, T_2, and T_3 are the fluid temperature measurements at the location of each sensor. The MAD equation for the CopterSonde-1 case is an extended version of Equation (3.1) given that it carries 4 sensors. It takes the difference of each pair of sensors obtained by permutation without repetition. The CopterSonde-1 and CopterSonde-3D CAD models were slightly modified to include dummy sensors with ideal trace points that collect air temperature after the simulation convergence. The simulated ambient temperature and wind speed were set to 293.2 K and 7 m s^{-1}, respectively, which are typical conditions for an average day in Oklahoma, USA. The wind direction was defined as a parametric variable that spans from 0 deg to 45 deg. Since both the

CopterSonde-1 and CopterSonde-3D airframes are symmetrical with respect to their longitudinal plane, then the range of 45 deg is enough to fully visualize the airflow behavior around them. Simple propeller CAD models were also included in the UAV models rotating at half the motor's top speed to simulate the prop wash. Lastly, the walls of each motor and the exterior of the shell were assumed to be the main sources and conductors of heat with the surrounding air. The heat transfer coefficients of aluminum 5052 and PLA plastic were used for the motors and shell, respectively. Motor temperature strictly depends on the power demand during a flight. However, based on data from stress flights, the worst-case scenario, it was observed that the motors and shell reached temperatures of 325 K and 305 K, respectively. Therefore, the wall conditions on the motors and shell were set to these measured temperatures.

Regarding simulation results, Figure 3.14 and 3.15 show examples of air temperature distribution around the platform for different wind directions as indicated by the green arrow. In these figures, it can be seen that the CopterSonde-1 produces a larger turbulent wake footprint, noticeable by the stagnant air and longer hot air trail downwind of the CopterSonde-1 compared to the CopterSonde-3D. This is a good indicator that the CopterSonde-3D presents less aerodynamic resistance, which helps improve high wind tolerance. Besides this, the turbulent wake close to the CopterSonde-1 rotors seems to be unpredictable, and, in some cases, it is visible that disturbed air flows near the sensors. On the other hand, the CopterSonde-3D exhibits a cleaner wake that stays behind the CopterSonde-3D for every wind direction step. Additionally, no visible disturbed air streams were found close to the scoop located opposite the wake. However, small temperature differences were detected after computing the MAD of the temperature measurements, which is included in Table 3.6. The localized sensor placement on the CopterSonde-3D exhibits a small spread in temperature, which stays consistent regardless of wind incidence angle. By contrast, the CopterSonde-1 presents large

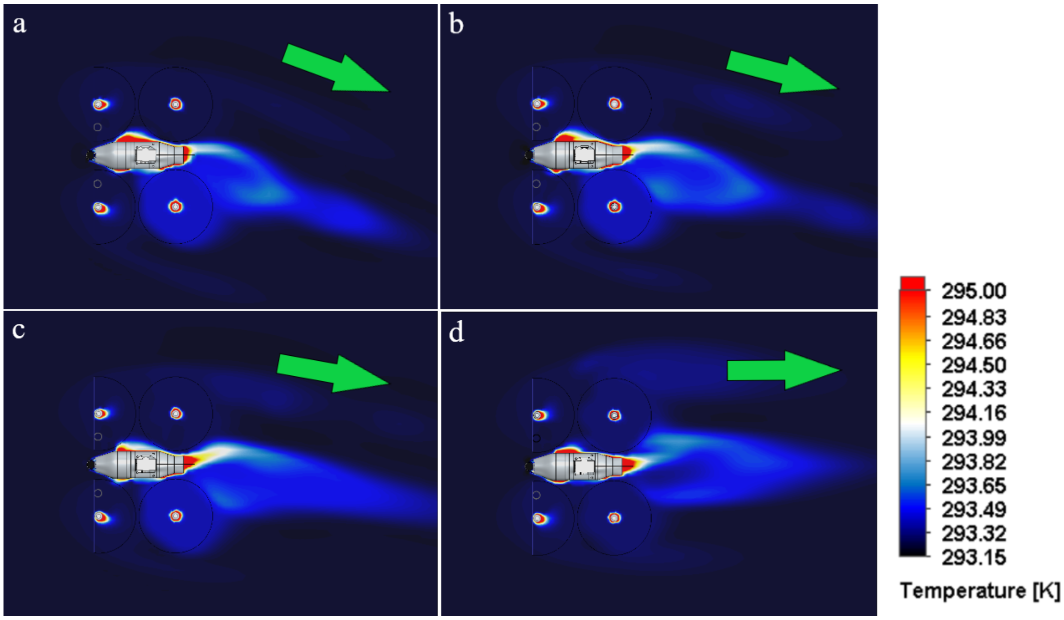

Figure 3.15: Color-map plots of air temperature distribution around the CopterSonde-3D model result of flow simulations using SolidWorks® CAD software. The shell and each motor were defined as the main sources of heat. The simulation did not include the effects of solar radiation. Different wind incidence angles, (a): 30 deg, (b): 20 deg, (c): 10 deg, and (d): 0 deg, were tested to visualize the effects of heat advection on the thermodynamic sensor using the proposed CopterSonde-3D UAV design for weather sampling.

measurement discrepancies among the sensors, evidenced by the large MAD values compared to the CopterSonde-3D.

3.5.2 Steady State Calibration

Every new build of the CopterSonde undergoes a series of calibration and validation steps. Taking advantage of the CopterSonde's modularity, the front shell was detached and configured for calibration inside an environmental chamber. The chamber used for the thermodynamic calibrations was the commercially-available Thunder Scientific Model 2500 (TSM2500) [96]. The TSM2500 is a reference instrument certified by the National Institute of Standards and Technology (NIST) and owned by the Oklahoma

Table 3.6: Comparison of mean of the absolute difference (MAD) for different wind incidence angles. MAD measures the spread in the temperature measurements among the thermodynamic sensors onboard the CopterSonde. If the sensors were correctly calibrated, MAD could be used as an indicator to determine the presence of sources of error, such as unwanted heat advection.

MAD	Wind incidence angle			
Platform	0 deg	15 deg	30 deg	45 deg
CopterSonde-3D	0.344 K	0.362 K	0.313 K	0.322 K
CopterSonde-1	0.397 K	0.664 K	1.876 K	1.869 K

Mesonet Lab located in the National Weather Center of the University of Oklahoma. A description of the Oklahoma Mesonet, its facilities, and operations can be found in [97]. The hardware setup for calibration is illustrated in Figure 3.16, where it can be seen that the entire front shell was fitted inside the chamber together with the thermodynamic probes of the TSM2500 and a calibrated Vaisala HMP155 probe [98] for redundancy. This configuration allows for the sensors to be tested and calibrated in their final fixed positions under similar thermodynamic conditions found in the field. The TSM2500 probes were placed as close to the intake of the scoop as possible in order to get similar aspiration conditions as the sensors inside the scoop. The front shell's ducted fan was left running during the whole calibration process to continually aspirate the sensors, besides also helping to mix the air more rapidly inside the chamber. One limitation of the TSM2500 is that it cannot condition the air below freezing temperatures, and thus, the sensors had to be left uncorrected under freezing conditions. Offset correction was applied to temperature and relative humidity measurements for above-freezing temperature conditions, which was the case for the majority of the flight operations conducted with the CopterSonde.

The TSM2500 can take up to 30 min to modify the air inside the chamber before settling down at desired temperature and humidity set-points. For this reason, it was opted to hold the air conditions for an hour long and only use the steady state portions for comparison and computation of the offsets. Hence, this calibration process only aims to correct steady-state biases of the sensors over a defined range [42, 99]. A method for correcting measurement errors due to fast sensor dynamics is discussed in the next chapter. Accordingly, the TSM2500 was programmed to automatically follow a defined temperature pattern and, subsequently, a relative humidity pattern. For temperature, chamber temperatures ranged from 10–30 °C by increments of 10 °C every hour at a constant relative humidity of 50 %. For relative humidity, the chamber was held at a constant 25 °C while varying relative humidity for an hour at each level. These levels were 15, 35, 55, 75, and 95 %. The calibration process took approximately 8 hours in total. Individual linear temperature and relative humidity sensor offsets were then obtained by comparing 1 min averaged measurements to the reference chamber's traceable sensor temperature and relative humidity in a steady state and computing their average differences or offsets. When applying the correction offsets to the sensor measurements, polynomial interpolation is used to determine the offset between the computed average differences.

3.5.3 Observations in the Field

In order to complement and give validation to the results obtained through flow simulations, real experiments were conducted in the field using the CopterSonde-3D. A windy day was chosen to give prominence to the heat advection effects on the thermodynamic sensors. Also, flights were conducted around solar noon to minimize temperature bias on the sides of the CopterSonde-3D due to solar radiation effects. Taking advantage of the WVFM, two special flight patterns were performed nearby a meteorological tower, used as a reference, to gather temperature data in an effort to resemble the results found

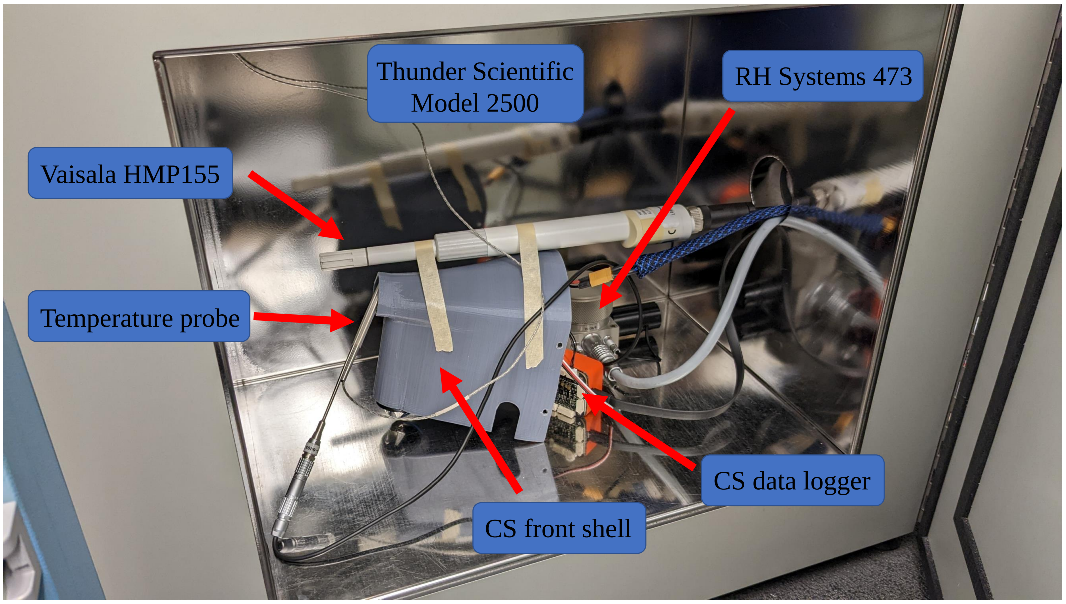

Figure 3.16: Experimental setup adopted for the calibration of the thermodynamic sensors inside the detached front shell of the CopterSonde-3D. The chamber used was a Thunder Scientific Model 2500 Benchtop Humidity Generator, a NIST-certified reference instrument from the Oklahoma Mesonet Lab of the University of Oklahoma. The chamber was programmed to condition the air and hold it for a period of 1 hour for each temperature and relative humidity step. The ducted fan was on during these calibrations to continually aspirate the sensors.

in the flow simulations. For both flights, the CopterSonde-3D was programmed to hover at the same height as the temperature probe on the tower with a horizontal separation of approximately 10 m.

For the first flight, the CopterSonde-3D maintained its orientation facing into the wind, assisted by the WVFM. This is the normal flight configuration of the CopterSonde-3D, where the thermodynamic sensors are placed downwind of the CopterSonde-3D. Halfway through the flight, an offset of 180 deg was sent to the WVFM, making the CopterSonde-3D rotate and align with the wind vector, effectively placing the sensors upwind of the CopterSonde-3D. Figure 3.17 illustrates the negative impact on the temperature measurements of the CopterSonde-3D caused by heat advection as a result of the 180 deg rotation. The observed temperature step is quite

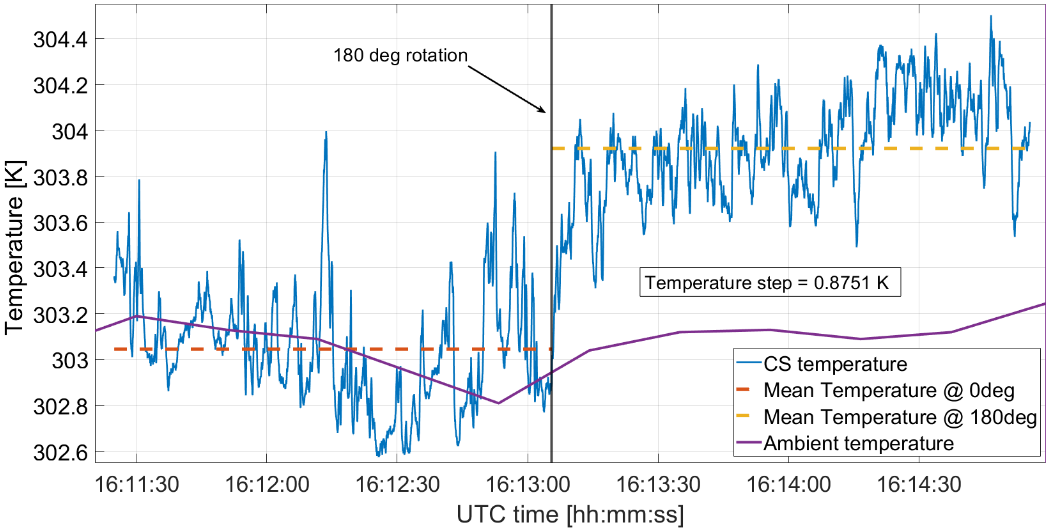

Figure 3.17: Temperature time series observed using the CopterSonde-3D while hovering near a meteorological tower for reference. Initially, the CopterSonde-3D was programmed to maintain its orientation into the wind to keep the sensors in undisturbed air. Halfway into the flight, the CopterSonde-3D was commanded to rotate 180 deg with respect to the wind vector and place the sensors upwind of the CopterSonde-3D. The increase in temperature is evidence of heat being advected from the CopterSonde-3D's body and across the sensors.

consistent with the flow simulation results and puts in evidence the flaws of the sensor layout of the CopterSonde-1.

For the second flight, the CopterSonde-3D was programmed to rotate about its vertical axis with a constant angular speed of 2 revolutions per minute. By doing this, the localized sensor-placement design behaved approximately like a distributed sensor-placement concept around the UAV. The CopterSonde-3D completed 15 revolutions during the flight while taking thermodynamic measurements in every azimuth direction, effectively measuring the air temperature distribution around the CopterSonde-3D. As a result, a point cloud of temperature observations was generated and plotted over heading as depicted in Figure 3.18. The mean ambient temperature and wind direction were computed using observations from the meteorological tower during the flight. The blue line represents the best fit curve using Fourier curve fitting, assuming the data follows a

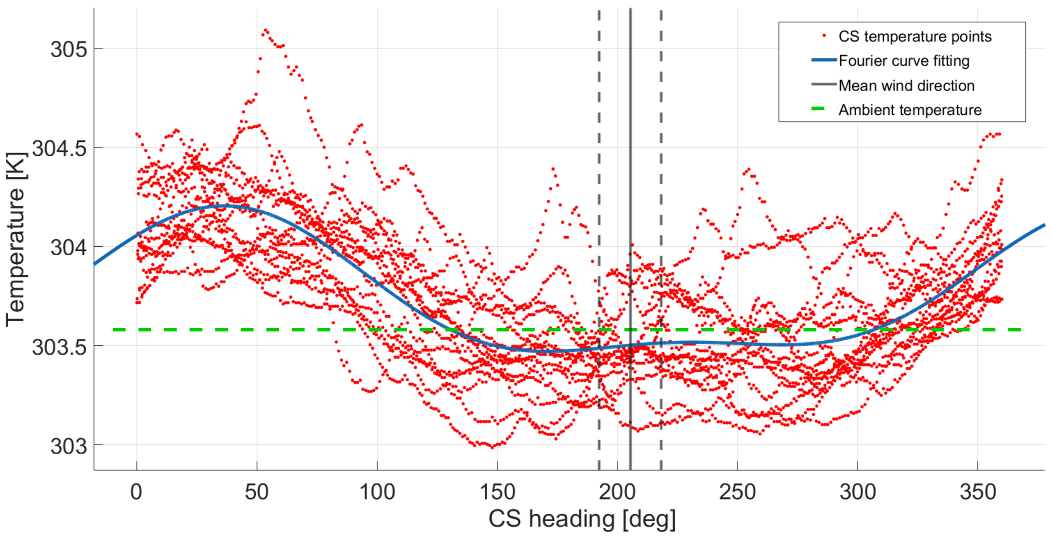

Figure 3.18: Point cloud of temperature observations over heading collected with the CopterSonde-3D while rotating with a constant angular speed of 2 revolutions per minute. The mean ambient temperature and wind direction were computed using observations from a nearby meteorological tower during the flight. The vertical dashed lines represent 3 times the standard deviation of the measured wind direction. The blue line represents the best fit curve based on Fourier curve fitting, assuming the data follows a sinusoidal pattern.

sinusoidal pattern. This clearly shows the maxima and minima of the temperature field around the CopterSonde-3D. More interestingly, the lowest temperatures, which are almost perfectly in agreement with the mean ambient temperature, are flattened out over a significant azimuth range centered close to the mean wind direction. This not only confirms the high effectiveness of the CopterSonde-3D sensor package design but also gives the WVFM some wiggle room to operate in without substantially affecting the thermodynamic measurements. Based on this observed flat region, a range of 50 deg on either yaw direction is set as a design constraint for the WVFM, which is discussed in the next chapter. The left-shifted mean wind direction over the flat region may be attributed to solar radiation since it was observed that the sun was located on the left plane with respect to the mean wind vector. As a consequence, the measured temperature on the left region ($<$ 200 deg) had a slight bias, while the opposite is seen on the right region (> 200 deg).

Push-up flights, or vertical profiles, were also conducted to examine and compare the thermodynamic measurements between the ascent and descent portions of the flight. It was observed that both portions exhibit different temperature and relative humidity observations, assuming that the PBL has not significantly changed its properties within the $\sim$15 min flight time. Particularly, the descent-leg measurements presented an increase in oscillations and a significant shift or lag compared to the ascent-leg measurements, as evidenced in Figure 3.19. The explanation for this mismatch is mainly due to the prop wash of the CopterSonde. When the platform is descending, the induced airflow of the propellers goes against the general motion of the air relative to the CopterSonde. This pushes the disturbed air from the propellers back to the CopterSonde, creating a temporary volume of stagnant and turbulent air around the platform. This volume of stagnant air takes longer to cycle, which drags and mixes air from higher layers down to the lower layers. This effect is seen as a "delay" or lag in the thermodynamic measurement with respect to the ascent leg. This effect is more pronounced when the CopterSonde is flying with little to no wind. The descent-leg measurement may be more consistent at higher wind speeds since the wind would help to push the prop wash away from the scoop. However, given the unpredictable nature of the prop wash, it was opted to prioritize and optimize the ascent-leg sampling and discard the descent-leg observations completely.

3.6 Operational Envelope and Energy Budget

The operational envelope defines the flight limits for the aerial platform with respect to maximum speed and structural loads given particular atmospheric conditions. This operational envelope is the region where the platform can operate safely and under con-

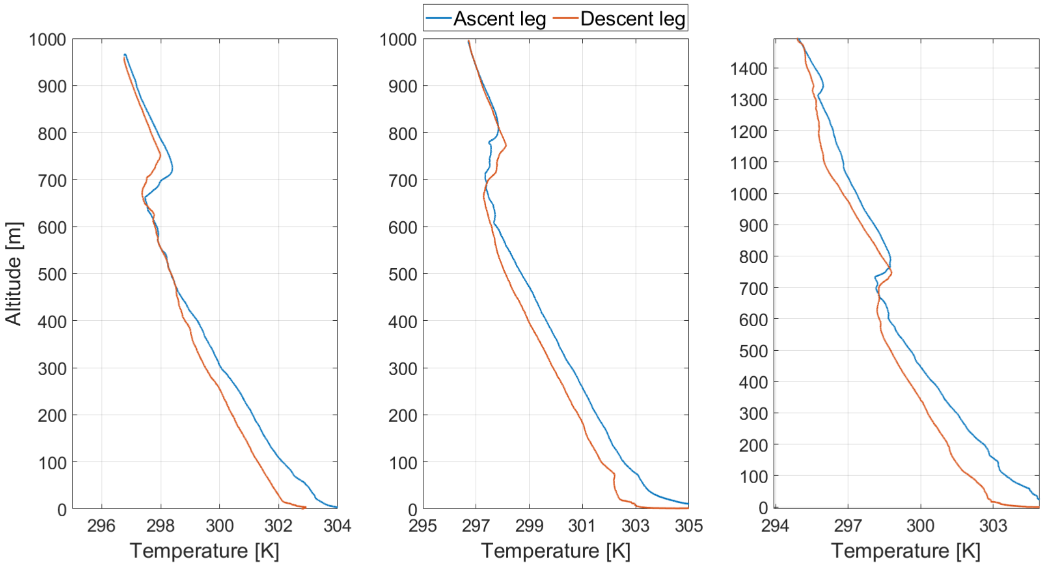

Figure 3.19: Three examples of vertical profiles taken with the CopterSonde-3D showing temperature measurement differences between the ascent and descent portions of the flight. The descent-leg measurements present a significant lag with respect to the ascent leg due to the effects of the prop wash of the CopterSonde-3D when descending.

trol in a stable manner. Any attempt to fly outside this region may cause damage to the platform and put the flight mission at risk. Given that the CopterSonde is an experimental platform, it is imperative to learn about its limits in order to establish safety procedures to avoid operating beyond its nominal design specifications. Additionally, since the CopterSonde is property of the University of Oklahoma, it must be insured through OU Risk Management department [100]. According to the university's guidelines, the CopterSonde was required to obtain an internal airworthiness certification before conducting field operations. Accordingly, flight tests were established to show OU's evaluators the system's capabilities, safety features, and ground crew management in order to comply with risk mitigation requirements.

Every new CopterSonde must first pass a series of flight tests to examine its structural integrity and system readiness. These flight tests were designed to put the CopterSonde through its paces and determine the boundaries of the flight envelope. Some

Table 3.7: Measured flight envelope and technical specifications of the CopterSonde-3D after examining a compilation of several flight tests done throughout the years of development.

Technical parameter	Measurement
Max. all-up weight	2.36 kg
Max. hover time	18 min
Max. forward speed	28.4 m s^{-1}
Max. sideways speed	22.3 m s^{-1}
Max. mean wind speed	22 m s^{-1}
Max. wind gust speed	26 m s^{-1}
Max. climb rate	12.2 m s^{-1}
Max. descent rate	6.5 m s^{-1}
Max. input voltage	17.5 Volts
Min. input voltage	12.5 Volts
Max. peak current	94.4 Amps
Max. constant current	61.5 Amps
Max. mechanical vibration	27 m s^{-2}
Max. motor temperature	52 °C
Max. operating altitude	3210 m AMSL
Max. altitude above ground	1800 m AGL
Max. operating temperature	40 °C
Min. operating temperature	-20 °C
Max. operating humidity	100% (light rain)

of the parameters, however, were learned after subjecting the CopterSonde to extreme weather conditions, such as arctic weather conditions in Finland and low air density in Colorado, USA. Moreover, the CopterSonde-3D successfully completed every flight where one of these parameters was topped, and post-inspections revealed that the CopterSonde-3D was still structurally sound. Table 3.7 lists all the measured flight envelope parameters and other important technical specifications that apply to the CopterSonde-3D, which were obtained after collecting flight data from several stress flight tests. Many of these parameters were then used as thresholds in custom algorithms for self-diagnosing. These algorithms were designed to trigger failsafe mechanisms automatically upon any extreme weather circumstance. Some of the custom

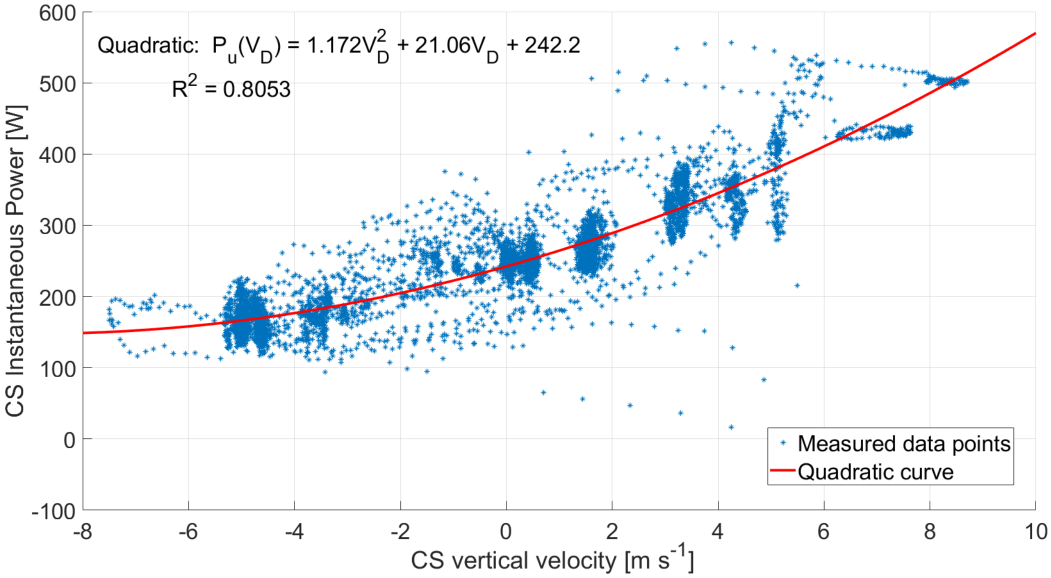

Figure 3.20: Scatter plot of the instantaneous power and vertical velocity of the CopterSonde-3D, which was fitted using a quadratic curve. The resultant function $P_u = f(V_D)$ is shown in the top left corner together with the cross-correlation. Multiple vertical flights were conducted using the CopterSonde-3D with different ascent and descent speeds each time. Meanwhile, instantaneous power drawn from the battery was recorded using the internal power module of the CopterSonde-3D. An extremely windy day ($>$ 10 m s^{-1}) was chosen for these flight tests to account for the high power demands of the worst-case scenarios.

failsafe mechanisms were described in Section 3.2.2.

Besides establishing the limits and specifications of the CopterSonde-3D design, studying the energy budget needed to successfully perform a single vertical profile and safely complete the flight was necessary. The parameters involved in the calculation of the energy budget are battery capacity E_B, required energy for ascent E_a and descent E_d, instantaneous power used P_u in flight, vertical velocity V_D of the UAV, the flight ceiling h_t, and the time t_h it takes to reach to the target altitude. Some of these parameters are known, like the battery capacity $E_B = 89.2$ Wh per manufacturer specification and the flight ceiling $h_t = 1524$ m AGL. This is because it was the highest flight ceiling that CASS got approved by the FAA. For this reason, the energy budget

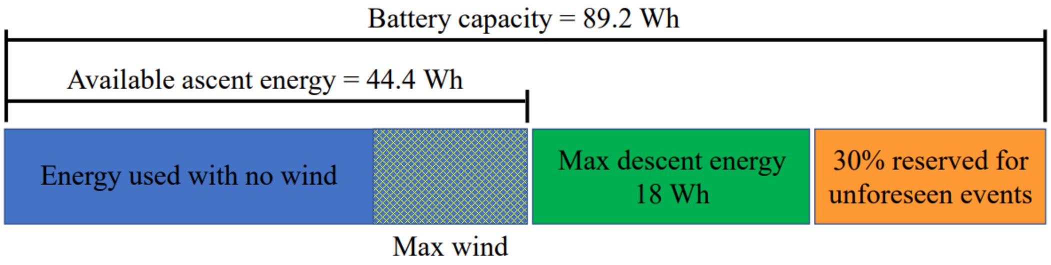

Figure 3.21: Proposed energy budget for the CopterSonde-3D assuming only vertical profiles with a flight ceiling of 1524 m are conducted. The energy for the descent leg was defined as a fixed value for safety reasons and obtained from flight tests in extreme wind conditions. Additionally, it was decided, out of precaution, to reserve 30% of the energy in the battery to prevent the battery from fully depleting in an unexpected event while flying. The remaining energy in the battery is used for the ascent leg, which can be managed within a range of ascent speeds.

of the CopterSonde-3D had to be tuned and adjusted to this specific height limit. Due to limitations in the autopilot software, the vertical velocity V_D can only be modified before takeoff and stays constant throughout the vertical profile. However, if desired, the ascent and descent vertical velocities can be different in magnitude. Since priority is given to the ascent-leg measurements, as explained in Section 3.5.3, it is convenient to spend as little energy as possible in the descent leg. Therefore, the CopterSonde-3D was programmed to descend at a constant speed of 5 m s^{-1}, leaving a safe margin with respect to the maximum descent speed. As good practice and for extreme precaution, a safety factor $S_f = 1.3$ was applied to the energy budget calculation from this point forward. This safety factor considers possible errors in the computation and unforeseen events that require extra energy to endure, like high winds, battery degradation over time, or unexpected maneuvers to avoid air traffic.

To begin with the calculation of the energy budget, the power used by the CopterSonde-3D must be characterized to determine its relationship with the vertical velocity. For this, multiple vertical flights were conducted using the CopterSonde-3D with different ascent and descent speeds each time. Meanwhile, instantaneous

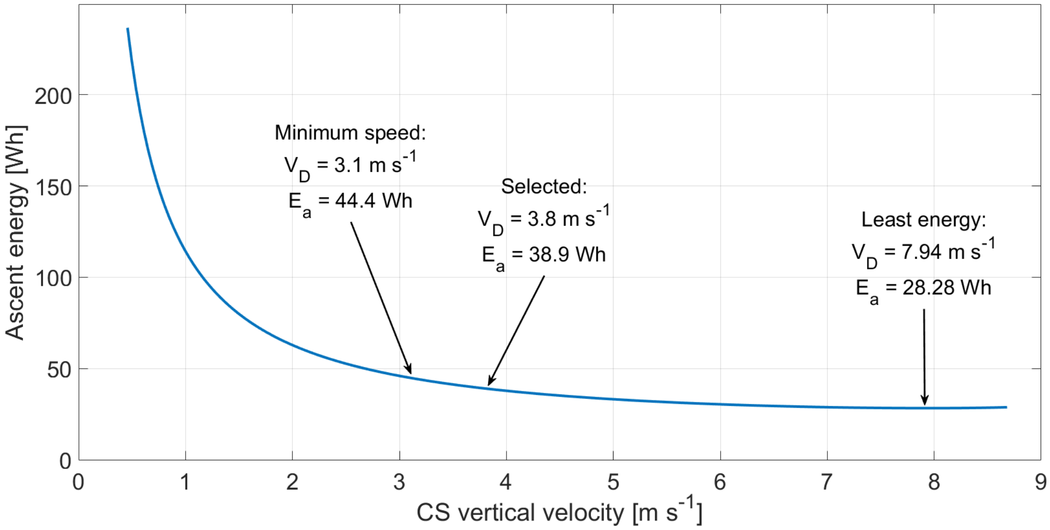

Figure 3.22: Plot of the ascent energy E_a required to reach a target altitude of 1524 m AGL as a function of vertical velocity V_D. A range of climb speeds was defined for the CopterSonde-3D, which meets the energy budget required to complete a vertical profile.

power drawn from the battery was recorded using the internal power module of the CopterSonde-3D. An extremely windy day (> 10 m s^{-1}) was chosen for these flight tests to account for the high power demands of the worst-case scenarios. The recorded data was used to produce Figure 3.20, a scatter plot of power against vertical velocity, which was fitted using a quadratic curve with resultant function $P_u = f(V_D)$ given as,

$$P_u = 1.172V_D^2 + 21.06V_D + 242.2 \quad [\mathrm{W}] \tag{3.2}$$

Using Equation (3.2), the energy E_d required for the CopterSonde-3D to descend from 1524 m at 5 m s^{-1} was calculated as follows,

$$E_d = \frac{S_f P_u(V_D) h_t}{3600|V_D|} \approx 18 \text{ Wh} \tag{3.3}$$

Therefore, this was defined as the minimum amount of energy that must be reserved from the CopterSonde-3D battery to make its way back to the launch point safely. Subsequently, an energy budget for the CopterSonde-3D is proposed in Figure 3.21 where the battery capacity and the descent energy are known. Additionally, it was decided, out of precaution, to reserve 30% of the energy in the battery to prevent the battery from fully depleting in an unexpected event while flying. The energy left in the battery (44.4 Wh) is used for the ascent leg, which can be managed by adjusting the ascent speed of the CopterSonde-3D. To visualize this, Equation (3.2) was modified to show the total energy consumption for the ascent leg after multiplying it by the time it takes to reach flight ceiling, or $t_h = \frac{h_t}{V_D}$. This math operation gives the following energy equation as a function of vertical velocity,

$$P_u \frac{h_t}{V_D} = E_a = \frac{1}{3600}\left(1.172 h_t V_D + 21.06 h_t + \frac{242.2 h_t}{V_D}\right) \quad [\text{Wh}] \tag{3.4}$$

which produced the plot illustrated in Figure 3.22. It can be seen that as the V_D increases, the E_a decreases up to a certain minimum point. Although the power required to move faster is greater, the reduced time to reach the target altitude compensates for the extra power demand on the energy budget. From Equation (3.4), a range of climb speeds was deduced which meets the energy budget requirements for a vertical profile up to 1524 m AGL. The limits of the ascent speed range are defined as $V_D = 7.94$ m s^{-1} for maximum speed, and $V_D = 3.1$ m s^{-1} for minimum speed. Although it is intuitive to choose the maximum ascent speed for minimum energy consumption, several other factors must be considered before selecting a climb rate. First, the spatial resolution of the atmospheric measurements gets more coarse as the velocity increases. Second, fast ascents require high power, which renders less available power to withstand high winds. Lastly, fast climb rates produce high stress on the propulsion system as a result of high power demands that can degrade the electronics faster. With these trade-offs in mind, a low ascent speed of 3.8 m s^{-1} was selected on the additional reasoning that the CopterSonde-3D is an experimental platform, and caution was taken not to wear out the instrument. It was opted to do more science with the CopterSonde-3D in a safe manner over exploring its limits and risking high expenditures.

3.7 Chapter Summary

The CopterSonde series rotary-wing WxUAV was developed in-house by a team of engineers and meteorologists from the University of Oklahoma. It was designed to be both robust and optimized for sampling the thermodynamic and kinematic state of the lower Earth's atmosphere, with a focus on vertical profiles in the planetary boundary layer. It provides the same information as the radiosondes but with much more control of its sampling location and the advantage of being reusable. The initial design, the CopterSonde-1, underwent considerable modifications that led to the latest version, the CopterSonde-3D. The current CopterSonde is capable of adaptive atmospheric sampling, real-time data processing, and data dissemination while offering significantly superior methods for mitigating thermodynamic measurement errors.

The design evolution of the CopterSonde platform and the proof of concept were thoroughly discussed in this chapter. It summarized the engineering challenges encountered from the concept of the UAV-based atmospheric measurements system to the current state and the decisions taken to continue improving the crucial components that conform to the WxUAV system. An intricate balance between autopilot software integration, airframe selection, and propulsion design had to be understood to create a platform capable of satisfying the desired atmospheric measurement requirements while complying with imposed safety protocols. On top of this, the sensor package and shell design were a challenge in and of itself that must work in harmony with the rest of the UAV components to produce satisfying results. By modifying the autopilot code, the chosen thermodynamic sensors were integrated into the CopterSonde system enabling the confluence of weather data streams with flight data streams. CAD models of the CopterSonde-3D and CopterSonde-1 were created and subjected to flow simulation to learn about the heat footprint of each platform over a range of wind incidence angles. This facilitated rendering visual images and producing statistics that helped to compare the two proposed sensor siting concepts. Based on the outcomes presented in Section 3.5, it is apparent that the localized sensor placement of the CopterSonde-3D combined with the WVFM is more successful than the distributed sensor layout of the CopterSonde-1 at mitigating effects from heat advection.

Moreover, field experiments were conducted to characterize the temperature field around the CopterSonde-3D and validate the flow simulation results. These experiments consisted in taking temperature measurements in different directions with respect to the wind field by manually introducing offsets in the WVFM estimation. The flights were carried out nearby a calibrated meteorological tower used for reference. The results of these experiments helped to define the range of angles in which the thermodynamic measurements are unaffected by heat advection. Additionally, it was shown that the prop wash is a source of large thermodynamic errors when the CopterSonde-3D is descending. As a result, priority was given to the optimization of weather sampling in the ascent leg over the descent leg.

Lastly, the flight envelope of the CopterSonde-3D was presented in Section 3.6 and defined after analyzing a collection of flight records where the CopterSonde-3D was subjected to extreme events. This helped to establish the design specifications of the CopterSonde-3D, which were then used as thresholds in custom algorithms for automatic self-diagnosing while in the air. These decision-making algorithms are able to trigger failsafe mechanisms and quickly alert the user about the issue. This greatly assists the user to quickly identifying ongoing extreme events and taking action to avoid pushing the CopterSonde-3D outside its operating range. Moreover, a thorough study of the energy budget required to complete a vertical profile successfully was discussed. Safety was kept as a top priority, and generous energy reserves were made available to the CopterSonde-3D in case of unexpected events while still being able to complete its mission.

Chapter 4

Weather-Specific Feature Developments

In this chapter, the major add-on features that contributed to enhancing the thermodynamic and kinematic measurement of the CopterSonde are described.

First, advanced modeling techniques and signal processing algorithms were investigated to compensate for slow sensor dynamics. For this study, dynamic models were developed to characterize and assess the transient response of commonly used temperature and humidity sensors. Consequently, an inverse dynamic model processing (IDMP) algorithm that enhances signal restoration was presented and demonstrated on simulated data. This study also provides contributions to analyzing the model stability necessary for proper parameter tuning of the sensor measurement correction method. Several case studies were discussed where the application and results of the IDMP through strong thermodynamic gradients of the PBL were provided.

Second, the design and implementation of the WVFM on the autopilot code were introduced, adding an extra flight function to the CopterSonde. The WVFM method allowed the CopterSonde to estimate wind direction and continuously turn itself into the wind. As demonstrated using flow simulations in Section 3.5.1, the resultant orientation was advantageous for sampling undisturbed air if the sensors were placed at the most downwind section of the UAV body. Moreover, the elongated shape of the CopterSonde body and shell took advantage of the aerodynamic benefits made possible when using the WVFM.

Third, given that the UAV significantly alters its immediate surrounding air to stay aloft, measurements can be affected by several sources of bias and uncertainties if these alterations are not considered. Three-dimensional (3D) wind sensing using UAV presents a particularly great challenge, as the induced airflow produced by the UAV must be decoupled from the desired wind measurements. Correctly placing the wind sensors on the multicopter UAV without compromising flight stability is one viable solution presented in the literature [101]. However, this approach requires significant modification of the multicopter UAV configuration, given that a great part of the sensor hardware must be exposed to moving air. This not only reduces valuable payload availability in terms of space and weight limitations but also increases air resistance which may lower the wind speed tolerance. The approach taken in this work was to discard as many protuberances from the UAV as possible to produce a sleek shell design with low air resistance. For this, it was opted not to use a dedicated wind sensor and, instead, exploit UAV characteristics to estimate wind in an indirect way. This chapter presents a method to estimate 3D winds simply by using the CopterSonde body without any dedicated wind sensor mounted. In other words, the entire CopterSonde acts as the wind-sensing element to produce wind estimations while trying to remove external disturbances through modeling techniques.

Finally, a brief discussion summarizing the contributions of these developments is provided at the end of the chapter.

4.1 Method for Correcting Thermo-Hygrometer Measurements

The aim of this section is to lay the foundations for exploring measurement restoration techniques suitable for weather sensors onboard WxUAS. The CopterSonde offers a unique way of mitigating measurement bias that can be exploited to improve the quality of the weather measurements further. The mitigation of slow sensor dynamics and the removal of sensor noise using low-cost weather sensors is challenging, but their impacts can be reduced using the right tools. The IDMP techniques have traditionally been used in control theory to design controllers to influence the system's behavior. This modern technique uses known physical properties of the sensor to restore the original signal given a sensor reading. To ensure the proper functioning and reliable results of the IDMP, it is important to mitigate sources of error around the UAS by applying the strategies discussed in Section 3.5. The IDMP is sensitive to noisy inputs and may produce divergence in the output if the system is close to being unstable.

Slow transient responses in sensors are commonly associated with amplitude attenuation and phase delay of the output signal (measured weather signal) with respect to the input signal (actual weather signal). These effects can be appreciated in the Bode diagram in Figure 4.1, which shows the frequency response of the forward model of the HYT-271 humidity sensor. The dynamics of the sensor are similar to that of a lowpass filter. The continuous model is the approximation to the analog behavior of the sensor, useful to simulate the "real" sensing element. The discrete system is a "sampled" version of the continuous system with a sample rate equal to that of the real sensor or the analog-to-digital converter (ADC). The truncation effect that comes with sampling a system produces a mismatch in the frequency response at high frequencies, which is also discernible in Figure 4.1.

While the impact of sensor dynamics can largely be neglected when considering static scenarios, measurements should not be considered co-located in space and instantaneous time when the sensor moves through strong gradients [88]. Several studies have proposed ways to reduce the impact of the sensor transient response for temperature [77, 78] and humidity [84] sensors.

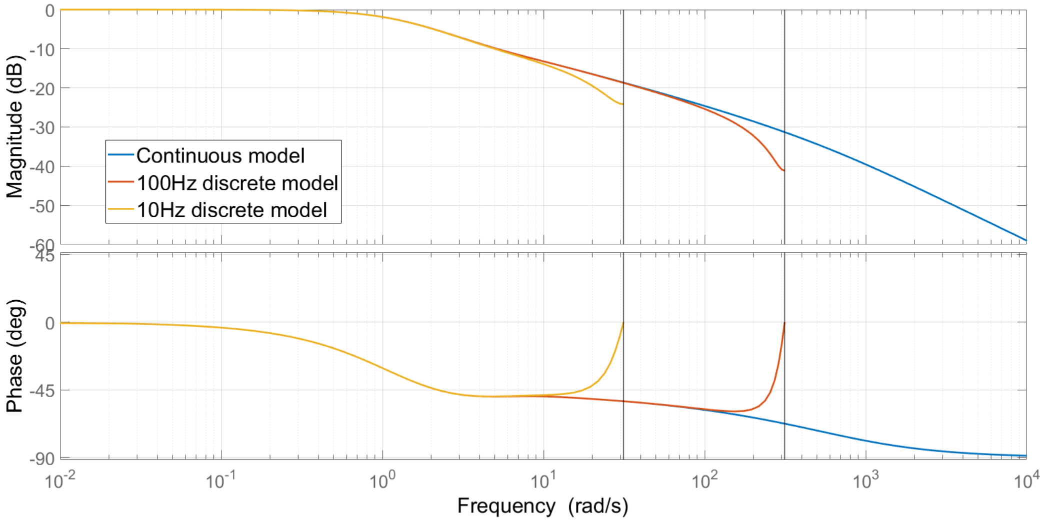

Figure 4.1: Example of Bode diagram of a continuous (blue line), or analog, sensor model and two discrete sensor models with different sampling rates (red and yellow lines). This shows the mismatch in the frequency response product of the truncation effects. Magnitude and phase are shown on the top and bottom plots, respectively.

Two mathematical models were introduced in Section 2.3, one describing the bead thermistor sensor dynamics and another describing the capacitive humidity sensor dynamics. The following sub-sections show the implementation of the IDMP measurement correction technique using these models. In an effort to reinforce the CopterSonde design concepts shown in the previous chapter, the results of the IDMP show evidence that the CopterSonde design effectively mitigates measurement biases compared to the standard UAS design.

4.1.1 Sensor Dynamics Characterization

In an effort to establish considerations and guidance for the sensor characterization on UAS, some studies conducted experiments where WxUAS were flown across a pseudo-step change in temperature and humidity from an air-conditioned room to the outdoor environment [23]. Although their goal was to measure the sensor time response with the effects of UAS altogether, the study only describes the qualitative results with few considerations to mitigate slow sensor dynamics. Therefore, a different approach was taken for this study, where the problem was divided into two parts. First, the sensors were isolated and characterized independently of the UAS body through experimentation. Second, sensor siting on the UAS and sampling techniques were investigated to minimize the external effects on the measurements.

The geometry and boundary conditions were defined in the forward sensor models presented in Section 2.3.1. The sampling period of the sensor for both iMet-XF and HYT-271 is known and equal to $\Delta t = 0.1$ s. The remaining parameters to be defined in the models are the thermal (water vapor) diffusivity α (D), the width of the sensing material R (L), and the thickness of the layers Δr (Δx). These parameters are usually unavailable in the sensor's datasheet and sometimes kept as a trade secret by the manufacturers. However, they are associated with the time response of the sensor, and, hence, the models can be adjusted to approximate the time response of the real sensor [84]. This way, the remaining parameters were obtained empirically through experimentation within a controlled environment. Ideally, the time response is measured by stimulating the sensor with an ideal step function (e.g., thermal shock). However, step functions of temperature and humidity are not possible in real-world conditions. Instead, [102] assumed a ramp function to model the thermodynamic shock and found that the error of assuming an ideal step function is less than 10% if the transition time from the initial to the final state is less than the time response of the sensor. Figure 4.2 shows the experimental configuration used to measure the step response of the weather sensors through the thermal shock. This included using an environmental chamber able to modify the temperature and humidity of the air to desired states. The environmental chamber used was a Thunder Scientific Model 2500 humidity generator provided by the Oklahoma Mesonet Lab located in the National Weather Center (NWC) of the

University of Oklahoma as described in Section 3.5.2.

Temperature and humidity shock experiments were conducted separately to determine the step response of each sensor. In these experiments, the shock was produced by rapidly inserting the sensors into the chamber through the side hole and allowing the sensor output to settle. The resulting shock was characterized by a sudden change in temperature and humidity over a distance of less than 10 cm, which translates to less than 1 s of sensor measurement time. Calibrated and validated sensors inside and outside the chamber were present on both sides of the shock for reference. The described shock experiment is a smaller scale of the experiments used to evaluate the sensor response in U-tube shields for mobile Mesonet [103], which were used as guidance in this study.

The data collected were then used to adjust the sensor models (see Section 2.3.2) using an iterative learning process called Differential Evolution (DE) [104]. The DE method optimizes the sensor model by adjusting the model parameters until finding a solution that closely matches the observations with regard to a given quality measure, such as the root-mean-square error (RMSE). Table 4.1 shows the resulting model parameters obtained for this particular experiment, while Figure 4.3 illustrates the step response comparison between the real sensor and the optimized sensor model. The response time, or rise time, is commonly defined as the time taken by the model's output to change from an initial state to 63.1% of the final value. Based on a step response analysis, the resulting temperature and relative humidity sensor models exhibit $\sim$ 0.7 s and $\sim$ 4 s rise time, respectively, which fall within the specifications of the sensors (see Table 2.1). The results of the presented sensor characterization process were used to develop and test the IDMP correction technique in the following sections.

It must be emphasized that the presented sensor characterizations are for a particular set of sensors within specified operating conditions. Several external factors

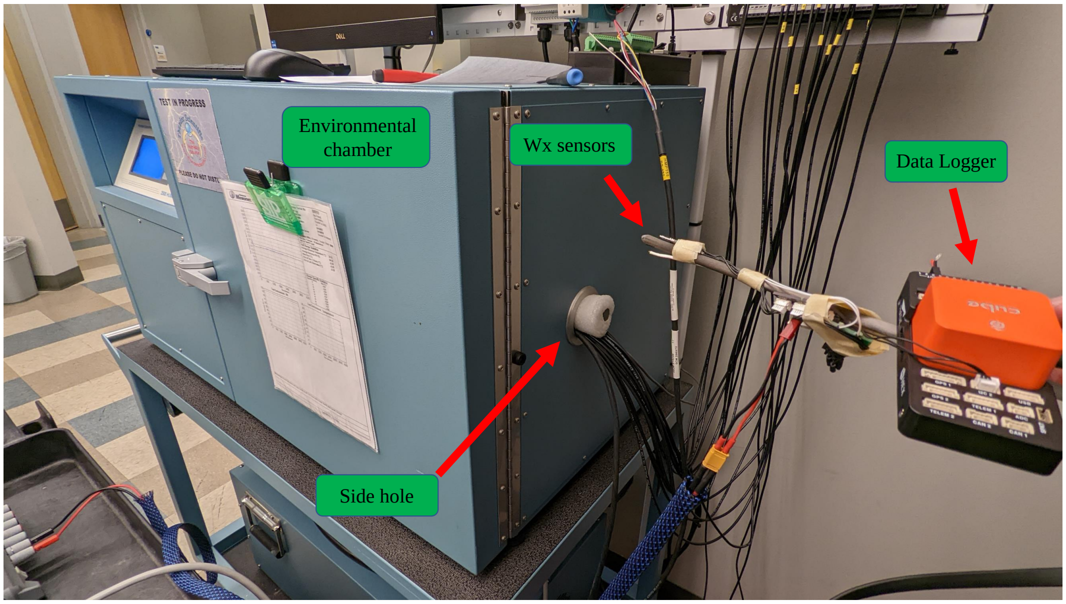

Figure 4.2: Experimental configuration used to measure the step response of the weather sensors. The air temperature and humidity inside the chamber were set to 308 K and 75 %, respectively. Whereas the room ambient was approximately 20 K and 20 % lower than the chamber, respectively. The thermal shock was performed by rapidly inserting the sensors into the chamber through the hole on the chamber's side. The environmental chamber used was a Thunder Scientific Model 2500 humidity generator provided by the Oklahoma Mesonet Lab in the National Weather Center (NWC) of the University of Oklahoma.

influence the physical aspects of weather sensors that must be considered to properly characterize the sensors for a wide range of temperatures and humidity. In particular, the capacitive humidity sensor is primarily affected by the ambient temperature [45]. This is because the porosity and thickness of the sensor's polymer significantly change with temperature. This means that there is no universal water vapor diffusivity D that can be effectively used for a wide range of ambient temperatures. Therefore, the shock experiments for the humidity sensor must be performed under multiple air temperature conditions to create a lookup table of values. Conversely, the thermal diffusivity α of the bead thermistor does not significantly change with humidity [105]. Consequently, only one shock experiment should be enough to compute a universal thermal diffusivity

Table 4.1: Resulting model parameters for temperature and humidity obtained using thermal shock observations with an environmental chamber and sensor model optimization with a Differential Evolution method.

Sensor	α or D	R or L	N	RMSE
iMet-XF	3.72×10^{-7} m^2 s^{-1}	1.1×10^{-3} m	2	0.3853 K
HYT-271	9.01×10^{-12} m^2 s^{-1}	1.01×10^{-5} m	23	0.7035 %

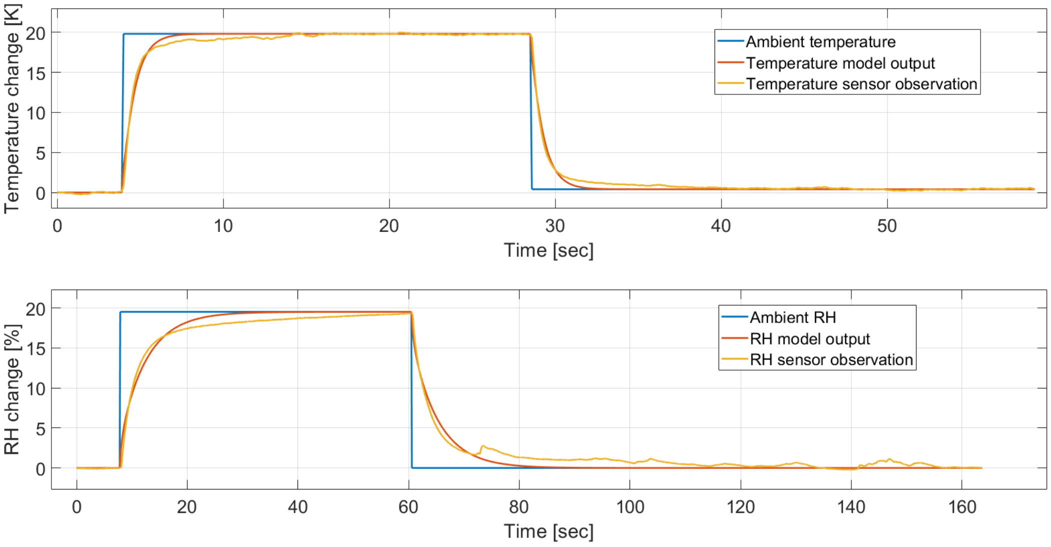

Figure 4.3: Step response comparison between real sensor measurements and sensor model outputs after optimizing the sensor models using thermal shock observations. The data collected from the shock experiment were used to adjust the sensor models (see Section 2.3.2) using an iterative learning process called Differential Evolution [104].

α for the bead thermistor.

4.1.2 General Procedures and Limitations of the IDMP

From this point forward, real weather signals are referred to as “actual” weather signals, whereas the output signals from the sensors and forward models are labeled as “measured” signals, and the restored signals using the IDMP are called “corrected” signals. In order to detail and formulate the IDMP restoration technique, a summary of the general procedure inspired by [84] is listed below:

1. Identify the sensor noise floor from the sensor measurements by inspecting its power spectral density (PSD) and suppress the noise using a zero-phase lowpass filter.
2. Apply the inverse sensor model to the filtered measurements after adjusting the model parameters based on the weather conditions and sensor characterization.
3. Re-apply the filter from step 1 to the restored signal to filter out any amplified noise.
4. Quantify the improvement by inspecting the time series and spectral response of the signal before and after applying the inverse sensor model.
5. Validate the correction by comparing the structure-function with the theoretical 2/3 slope for locally isotropic turbulence in the ISR.

Given the assumed Taylor's hypothesis for frozen field, the CopterSonde flights were limited to steady hovers in CBL and windy conditions. This enables converting temporal measurements into spatial measurements, which is necessary for the computation of the KTS and the structure-function. Step 5 in the procedures is feasible if and only if the atmosphere is assumed to be horizontally homogeneous and locally isotropic without any rapid atmospheric evolution [71].

The initial signal conditioning of the measured signals is necessary to avoid feeding the IDMP with noisy signals that could produce divergence. Therefore, the measured signals were first run through a digital lowpass filter. The cut-off frequency of the filter was manually tuned on a case-by-case basis by inspecting the PSD of the measured signal. The cut-off frequency was defined as the frequency where the PSD has a noticeable increase in its slope greater than -5/3. Additionally, a logic to identify distortions and contamination in the PSD was formulated by taking advantage of KTS. The reasoning is as follows:

- Based on KTS, the natural trend of the PSD should be a slope of -5/3 on a log scale. Accordingly, if the slope of the PSD is greater than -5/3 at high wavenumbers, the region is considered to be contaminated by external perturbations and/or sensor noise. Therefore, it must be removed using a lowpass filter before the restoration phase and prevent undesired signals from getting amplified.
- Otherwise, if the slope is less than -5/3, then the measured signal is considered to be attenuated and distorted by slow sensor dynamics. This indicates that the sensor cannot keep up with the fast variations and fails to capture the turbulence dynamics. With proper sensor characterization and modeling, the IDMP should be able to correct this bad trend and produce a corrected signal with a PSD approximating the theoretical -5/3 slope line.

The next step is to run the conditioned signal through the core of the IDMP method, the inverse model of the sensor. To obtain the inverse model $H(z)$, the z-transform of the state-space system is computed first, and then the system is inverted using control theory methods. These operations were done using MATLAB 2020a Update 8 (February 2022 release). $H(z)$ was then fed with the filtered sensor measurements to produce the corrected sensor measurement. Lastly, the same lowpass filter was applied to the corrected signal to remove any amplified noise that survived the process.

4.1.3 System Tuning

The inverse system of $G(z)$ exists and is stable if and only if $G(z)$ is minimum phase, meaning that all the poles and zeros are within the unit circle [106]. As a result, the transfer function of the inverse sensor model is obtained by simply taking the inverse of $H(z) = G^{-1}(z)$. Even though the process of finding the inverse seems to be simple and straightforward, special attention must be given to the poles of $H(z)$. The resulting poles of $H(z)$ might end up too close to the unit circle, which could cause instability and divergence in the output signal. The stability parameter for the presented models is defined by [83] as $\phi = \frac{\gamma \Delta t}{\Delta x^2} < 0.5$ where γ is an intrinsic parameter of the sensor, such as the thermal and diffusivity coefficients. The equation shows how fast the sampling rate must be in order to precisely capture the dynamics of the sensor within a small spatial interval. Given that the sampling rate of the sensors is fixed to $\Delta t = 0.1$ s, then the only way to adjust the poles is by varying Δx. This means that to capture the internal dynamics of the sensor, then a proper spatial discretization of the sensing element is required. The forward model and; hence, its inverse $H(z)$ are stable with large values of Δx at the expense of reducing the order of the model and; consequently, the overall accuracy and resolution of the method. Moreover, notice that the degree of correction made on the sensor measurements is limited by the sensor's sampling rate. If the same sensors could sample at higher rates, the IDMP would become more effective.

4.1.4 Weather Signals Generation and Sensor Simulation

The first step to investigate the potential of applying the IDMP for temperature and humidity measurements is to develop a time-series weather signal generator that could be used as a benchmark to evaluate the performance of the proposed framework. As described in Section 2.2.2, CBL weather signals from a horizontal transect tend to have a particular PSD with a -5/3 slope on a log scale. Moreover, assuming horizontal CBL weather signals are produced by a wide-sense stationary (WSS) random process with a Gaussian probability density function, it is possible to generate the artificial

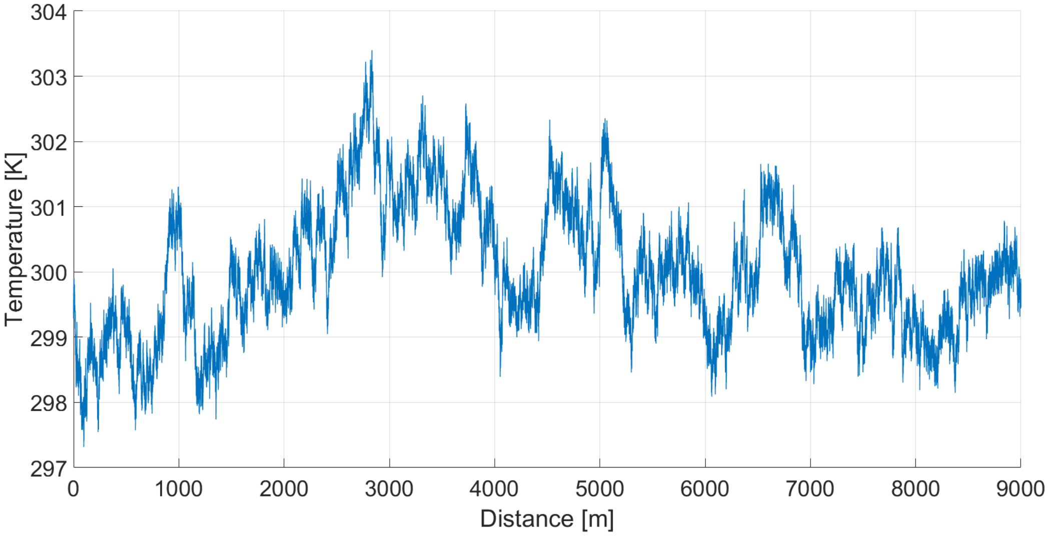

Figure 4.4: Generated spatial temperature signal that follows the -5/3 Kolmogorov law. This was obtained after converting the time-series data given a constant wind speed of 10 m s^{-1} using Taylor's hypothesis of frozen fields.

weather signals by modifying the PSD of a Gaussian white noise signal to look like Kolmogorov's energy cascade power spectrum. This was achieved by taking the PSD of a white noise signal generated with MATLAB. Subsequently, each PSD point was divided by its corresponding frequency to the power of 5/3 while keeping the phase unchanged. Figure 4.4 shows an example of an artificially generated CBL weather signal.

4.1.5 Validation of the IDMP in Simulated Conditions

To simulate the sensor measurement process, the sensor model was divided into three parts: the analog sensing element, the ADC discrete sampling, and sensor noise generation. The sensing element was simulated using the forward models shown in Section 2.3 with a much smaller sampling period $\Delta t = 0.01$ s. This is because analog signals cannot be generated in a digital computer, and, therefore, the best approximation is to increase the resolution of the discrete model. The actual weather signal was run through the high-resolution sensor model to add the effects of sensor dynamics. This signal then goes through the ADC, which downsamples the signal to the actual sampling period of the sensor $\Delta t = 0.1$ s. The down-sampling process may create aliasing of rapidly changing signals, which makes it more realistic. Finally, the down-sampled signal gets its characteristic noise floor by adding additive white Gaussian noise (AWGN). The noise amplitude from each sensor was taken from previous steady-state calibrations conducted in a controlled laboratory environment (see Section 3.5.2).

The following measurement validation method for CBL conditions exploits the ISR of turbulent fluctuations theory by using the PSD and structure-function calculations. In real-world CBL conditions, data were collected by conducting a hovering or stationary flight in windy conditions at a constant altitude using a multicopter UAV. For brevity, results will be shown in an alternated fashion between temperature and humidity.

As an example, the PSD of generated weather signals was computed and compared in Figure 4.5. Following the procedures of the IDMP, the cut-off frequency of the low-pass filter was selected near the constant and flat power level of the measured signal, and the sensor noise was effectively mitigated as a result. The effect of the slow sensor dynamics is noticeable as a downward trend with respect to the -5/3 slope line. The IDMP successfully restored the power levels of the measured signal at high frequencies. Next, Figure 4.6 shows a comparison of the time-series of the measured and corrected signals. The time-series plot clearly shows an improvement in the time response of the sensor where the corrected signal is more tightly fit to the actual weather signal. Finally, Figure 4.7 shows results from the two-point spatial correlation calculation, namely, the structure-function. Assuming locally isotropic turbulence conditions, the deviations of the computed structure function from the theoretical 2/3 slope in the ISR region are indications of the effects of sensor dynamics and sensor noise on the

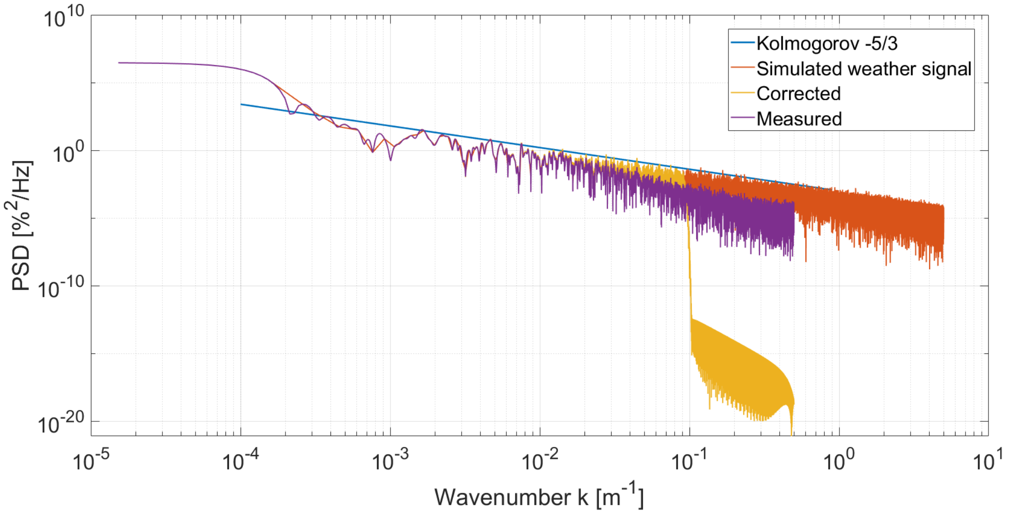

Figure 4.5: Power spectral density of the simulated weather signal and processed signals using the sensor models in CBL conditions. Results from before and after applying the IDMP are shown.

measurement. Moreover, the results can be used to slightly tune the IDMP until getting the best-possible agreement with the theory. The presented results show that the IDMP method is able to partially restore the signal without any visible signs of instability and oscillations. Given that the generation of the weather signals is random, the IDMP was demonstrated to be consistent and able to produce similar results using other similar weather signals as inputs. The restoration is partial because of missing parts in the frequency content due to noise filtering, low sampling rate, and poor capturing of the weather dynamics.

4.1.6 Evaluation with Real Data

The presented simulation results show the feasibility of the IDMP technique on measurements taken with a UAS under ideal conditions. However, several assumptions were made to produce the models and simulations, which may not hold true for real observations in the field. Therefore, to begin exploring the mitigation of slow sensor

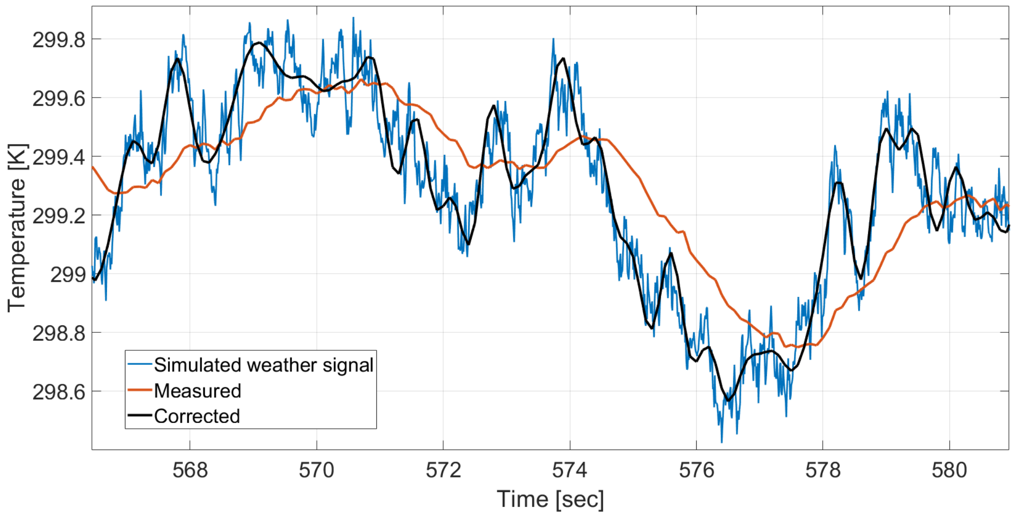

Figure 4.6: Time-series of the simulated weather signal in CBL conditions and processed signals using the sensor models. Results from before and after applying the IDMP are shown.

dynamics and sensor noise for realistic UAS flights, the IDMP was applied to real data collected using the CopterSonde. Two flights were picked from the extensive database made in the past years throughout several field campaigns. These flights were conducted in CBL and FTI weather conditions, respectively, at the Kessler Atmospheric and Ecological Field Station (KAEFS) in Purcell, Oklahoma, USA, located 30 km southwest of the OU Norman campus. The Certificate of Authorization (COA) with number 2020-CSA-6030-COA, issued by the Federal Aviation Administration (FAA), allowed for CopterSonde flights above 400 ft with a flight ceiling of 5000 ft.

In CBL conditions, the CopterSonde was flown stationary at a constant altitude of 10 m for about 15 min with a mean wind speed of 10.2 m s^{-1}. Figure 4.8(a) shows a close-up of a portion of the measured and corrected relative humidity time series, while Figure 4.8(b) illustrates the degree of correction made by the IDMP. This is noticeable by observing the amount of deviation in the structure-function, particularly in the region of smaller lags. With this, the IDMP demonstrates it is capable of partially restoring

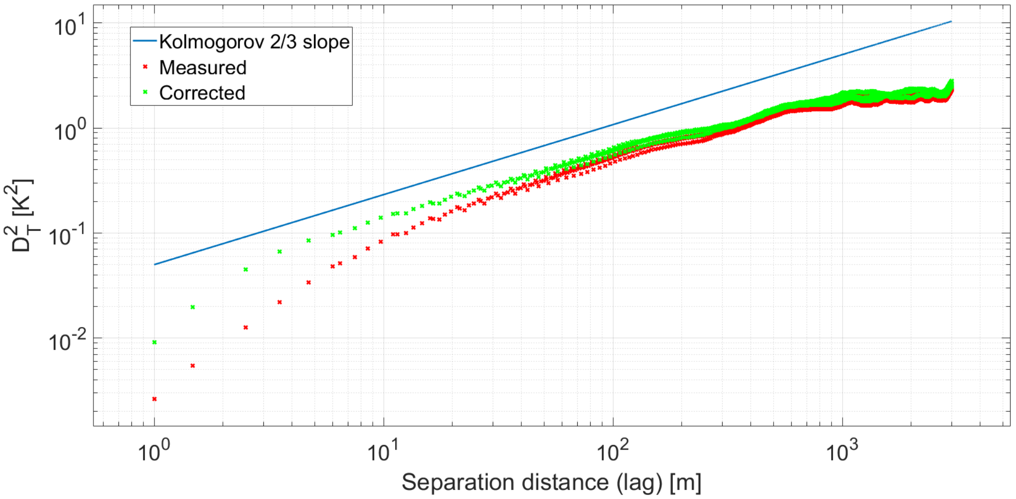

Figure 4.7: Structure function of the simulated weather signal and processed signals using the sensor models in CBL conditions. Results from before and after applying the IDMP are illustrated.

high-frequency content that was initially degraded by slow sensor dynamics.

In FTI conditions, the CopterSonde was flown shortly after a cold front moved through KAEFS, leaving a shallow cold pool. The ascent rate was set to 3.8 m s^{-1}, whereas the descent rate was set to 5 m s^{-1}. The CopterSonde was sent to 1300 m AGL, collecting temperature and humidity data in the ascent and descent legs. The flight took about 10 min from take-off to landing. Figure 4.9(a) shows a comparison between the measured and corrected vertical profiles of relative humidity. The correction is not noticeable due to the large spatial scale and the slow vertical speed of the UAS. The errors are smaller when flying at low speeds; however, the observation might not be representative because the weather phenomena may have evolved faster than the observation period [88]. However, Figure 4.9(b) is a zoomed-in plot of the lower altitude region where the small correction is visible. Assuming that the descent-leg observations are valid, this helps to confirm that the ascent and descent speeds of the CopterSonde are small enough not to impact the sensor measurements when flying

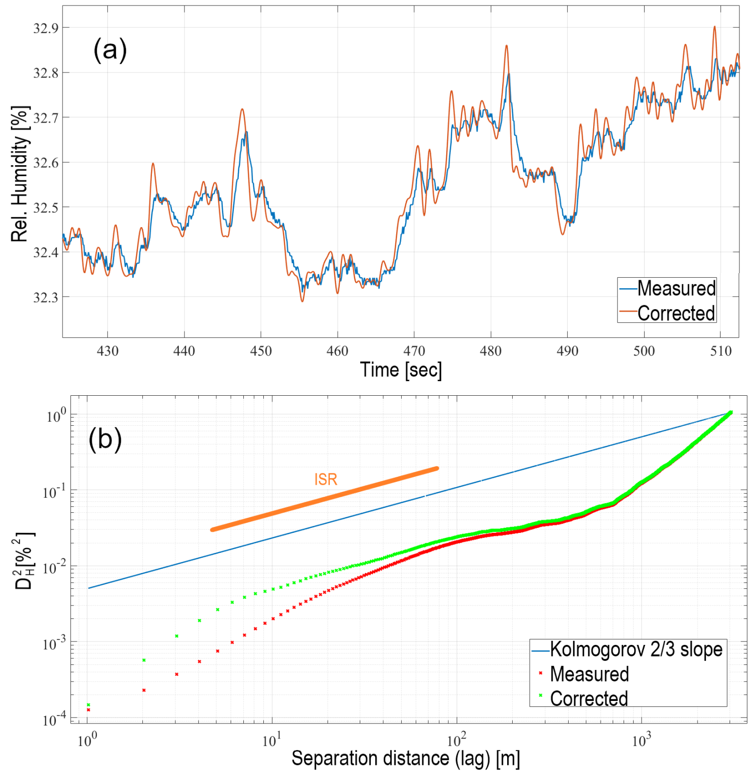

Figure 4.8: Thermodynamic observations were collected using the CopterSonde-3D at KAEFS in Purcell, Oklahoma, USA. The platform was flown stationary at a constant altitude of 10 m for about 15 min with a mean wind speed of 10.2 m s^{-1}. Raw relative humidity measurements were compared against the same data processed using the IDMP technique: (a) Time-series comparison of the measured relative humidity against corrected relative humidity. (b) Relative humidity structure-function comparison.

across a steep thermodynamic gradient. Given that the amount of correction was small, the IDMP method may not be worth using for this case unless the study of small-scale high-frequency variations is relevant.

4.2 Wind Vane Flight Mode

Concisely, the concept of the WVFM was to ensure that the CopterSonde is pointing headwind by changing its yaw angle in the direction that the roll is minimized. The advantage of this approach is that there is no need for an additional dedicated wind sen-

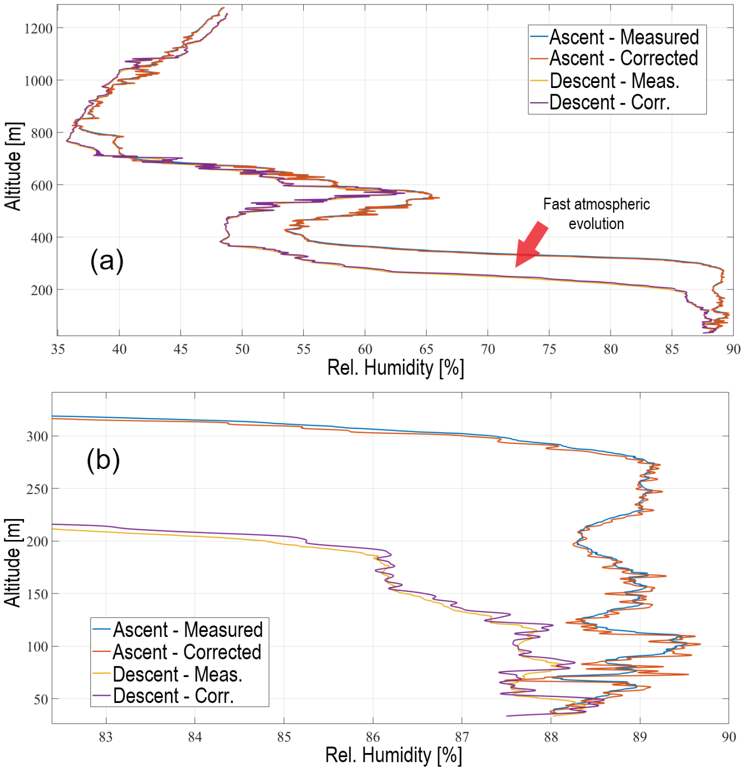

Figure 4.9: The CopterSonde was flown up to 1300 m AGL shortly after a cold front moved through KAEFS, leaving a shallow cold pool. The ascent rate was set to 3.8 m s^{-1}, whereas the descent rate was set to 5 m s^{-1} . (a) Vertical profile of relative humidity over height, measured against corrected data. (b) A close-up plot of the first 300 m of the vertical profile.

sor like an airspeed sensor or anemometer. Otherwise, the extra onboard device would reduce the available space and weight limit for other valuable payload components. By maintaining the CopterSonde orientation into the oncoming wind, the air being drawn across the sensors has not been disturbed by the effects of the CopterSonde body. It also enabled the selection of an elongated airframe configuration that allows longitudinal distribution of the internal components (see Section 3.3.1). This helped enhance the shape of the CopterSonde shell in one direction and decreases the aerodynamic drag that would otherwise be unachievable with a conventional and symmetric UAV airframe.

The following sections describe the theory behind the WVFM and its integration into the CopterSonde. The method was tested and debugged in a simulated environment to guarantee its correct behavior before implementing it on the real autopilot code. Finally, comparisons against conventional wind instruments are shown from which operating ranges and limitations were defined.

4.2.1 Concept and Theory

The position and velocity estimates computed by the navigation system of the CopterSonde's autopilot are based on an absolute Earth reference frame. This is done by using the GNSS on board the CopterSonde and computed by the autopilot. The position and velocity estimation accuracy are further improved by the autopilot by internally fusing the GNSS data with the IMU data. Given that the ArduPilot autopilot code uses a Proportional-Integral-Derivative (PID) flight control system, it only reacts when there is a position or velocity error with respect to the desired target location. Meaning that the CopterSonde will remain in its target position regardless of external forces or disturbances.

For instance, wind produces a drag force D over the CopterSonde that pushes it away from the target location, increasing the position error. Consequently, the CopterSonde compensates for the position error by tilting its thrust vector in the opposite direction to the wind. This cancels out the force applied by the wind while the CopterSonde remains in position. However, if commanded, the CopterSonde may tilt its thrust vector to change its horizontal position. This additional inclination is added to the tilt caused by wind, potentially producing wrong wind estimates unless properly accounted for. Assuming there is no horizontal position change through the vertical profile, it is possible to take advantage of the CopterSonde's reaction to the wind to estimate the wind vector based on its tilt and aerodynamic properties.

The WVFM method was formulated on angle estimations provided by the onboard IMU built into the CubeOrange autopilot board. The ArduPilot flight code follows the North-East-Down (NED) reference frame convention defined as $I : \{\vec{N}, \vec{E}, \vec{D}\}$ [91] which is used as the inertial reference frame. The $\vec{N}$ axis points True North, the $\vec{E}$ axis points East, and the $\vec{D}$ axis points to the center of the Earth. For ease of calculation, the origin of the I frame is coincident with the center of mass (CoM) of the CopterSonde. A second reference frame, the body frame, was defined as $B : \{\vec{X}, \vec{Y}, \vec{Z}\}$ and it follows the angular movements of the CopterSonde with origin on the CoM as well. The $\vec{X}$ axis points forward, $\vec{Y}$ axis points to the right, and $\vec{Z}$ axis points down perpendicular to the $\vec{X}\vec{Y}$ plane.

The orientation of the frame B with respect to the inertial frame I was defined by using Euler angles: pitch θ, roll ϕ, and yaw ψ. However, the order of rotations is not associative, and a convention must be defined beforehand. Again, following ArduPilot's definition, the chosen order of rotation is yaw-pitch-roll, where the first rotation is the right-most angle in the sequence. Each of these individual rotations can be described using a 3×3 matrix, defined in Equations (4.1)–(4.3), where s and c denote sine and cosine functions, respectively. The notation R_B^I means a conversion from the B frame to the I frame. In other words, a vector expressed in B frame that is left-multiplied by R_B^I results in a vector expressed in I frame [107].

$$R_B^I(\psi) = \begin{bmatrix} c_\psi & -s_\psi & 0 \\ s_\psi & c_\psi & 0 \\ 0 & 0 & 1 \end{bmatrix} \tag{4.1}$$

$$R_B^I(\theta) = \begin{bmatrix} c_\theta & 0 & s_\theta \\ 0 & 1 & 0 \\ -s_\theta & 0 & c_\theta \end{bmatrix} \tag{4.2}$$

$$R_B^I(\phi) = \begin{bmatrix} 1 & 0 & 0 \\ 0 & c_\phi & -s_\phi \\ 0 & s_\phi & c_\phi \end{bmatrix} \tag{4.3}$$

It is possible to get a single rotation matrix by multiplying all individual rotation matrices together in the order of the convention. The result of multiplying the rotation matrices together is shown in the following.

$$R_B^I(\psi,\theta,\phi) = \begin{bmatrix} c_\theta c_\psi & -c_\theta s_\psi + s_\phi s_\theta c_\psi & s_\phi s_\psi + c_\phi s_\theta c_\psi \\ c_\theta s_\psi & c_\phi c_\psi + s_\phi s_\theta s_\psi & -s_\phi c_\psi + c_\phi s_\theta s_\psi \\ -s_\theta & s_\phi c_\theta & c_\phi c_\theta \end{bmatrix} \tag{4.4}$$

The rotation matrix can be computed every time the autopilot outputs a new set of Euler angle estimates. The tilt vector $\vec{e}_T$ is a vector expressed in the I frame, and it measures the inclination angle γ of the CopterSonde with respect to the D axis. To obtain the tilt vector $\vec{e}_T$ using the rotation matrix, $R_B^I(\psi,\theta,\phi)$ must be multiplied by the column vector $\vec{V}_B = [0,0,1]^T$ which is the Z axis of frame B. As a result, the tilt vector $\vec{e}_T$ is equal to the right-most column of $R_B^I(\psi,\theta,\phi)$ in Equation (4.4) which is shown below.

$$\vec{e}_T = \begin{bmatrix} s_\phi s_\psi + c_\phi s_\theta c_\psi & -s_\phi c_\psi + c_\phi s_\theta s_\psi & c_\phi c_\theta \end{bmatrix}^T \tag{4.5}$$

The projection of the vector $\vec{e}_T$ onto the $\vec{N}\vec{E}$ plane gives a vector that points in the opposite direction of the inclination. After reversing the projected vector, the angle with respect to True North is assumed to be the absolute wind direction if the flight conditions described at the beginning of this section are followed. Taking the arc tangent of the first two elements of the tilt vector in Equation (4.5) results in wind direction estimates given by the expression:

$$\Psi = \arctan(\frac{s_\phi c_\psi - c_\phi s_\theta s_\psi}{-s_\phi s_\psi - c_\phi s_\theta c_\psi}) \pmod{2\pi} \tag{4.6}$$

The inclination angle γ is directly proportional to the aerodynamic drag force D on the aircraft. D in turn is related to the horizontal wind speed U_H encountered by the CopterSonde defined as:

$$U_H = \sqrt{\frac{2D}{\rho A_{proj} c_d}}, \tag{4.7}$$

where ρ is the air density, A_{proj} is the aircraft surface area normal to the wind, and c_d is a drag coefficient [108]. This equation is a modification of the Rayleigh equation for aerodynamic drag. Because of continually changing conditions and orientations of the multicopter UAV, A_{proj} and c_d are generally not well defined. However, it is possible to estimate wind speed through a linear regression model as:

$$U_H = C_0 + C_1 \sqrt{\tan\gamma}, \tag{4.8}$$

where constants C_0 and C_1 are derived empirically using a common reference measuring wind speed. This model, therefore, accounts for the intricate design geometry of the aircraft to a first-order approximation without the need for complicated expressions for drag coefficients and surface areas.

4.2.2 Code Implementation

The ArduPilot autopilot code allows for seamless integration of user-defined functions. These custom functions run in a separate thread from the main flight control, although it is possible to exchange data between them. The WVFM algorithm was written inside an empty code “slot” meant for code testing and development provided by ArduPilot. The computational procedure of the WVFM method is presented in Table 4.2. In general, the raw WVFM wind estimates carry high-frequency signals due to the mechanical vibrations captured by the IMU. However, the high-frequency content in the estimates is too high for the CopterSonde yaw control dynamics to follow properly. If the raw estimates are directly injected into the autopilot, it could result in significant damage or failure of the airframe and propulsion system. Therefore, the main reason for including digital infinite impulse response (IIR) Butterworth filters was to smooth out the wind estimates of the WVFM to the point where the yaw control performs stably.

On top of the WVFM algorithm, a state machine code was used to handle the different possible scenarios during flight and perform specific tasks. The WVFM state machine overrides the yaw control of the CopterSonde and uses a decision-making process to validate the yaw commands generated by the WVFM. The WVFM function is active only when the CopterSonde is flying in an autonomous flight mode. The human operator is able to take over full control of the CopterSonde by disabling the function at any time if desired. As described in the previous section, the WVFM produces valid wind estimates when the CopterSonde is flying horizontally steady. Therefore, if the speed of the CopterSonde is over a defined threshold, then the WVFM stops correcting the platform’s heading and switches back to the default “look-ahead” yaw commands. An important safety feature incorporated into the WVFM is the automatic high wind fail-safe which triggers the Return-To-Launch (RTL) mode immediately after detecting extreme wind speeds. This function greatly helps relieve the CopterSonde operator from judging extreme flight scenarios in high wind where the CopterSonde is pushed to its operating limits. Figure 4.10 illustrates the WVFM state machine process, which runs in a loop at a rate of 10 Hz.

Table 4.2: Pseudo-code of the WVFM algorithm incorporated into the ArduPilot autopilot code. This code is executed in a loop providing wind estimates at a rate of 10 Hz. If desired, the wind vane mode can be enabled or disabled while still estimating wind.

```
1. Initialize wind estimates and Butterworth filters
        $\lambda \rightarrow 0,\ v_{wind} \rightarrow 0$
while true:
    2. Get Euler angles and compute rotation matrix
        $\psi, \theta, \phi \rightarrow R_B^I$
    3. Retrieve tilt vector from rotation matrix
        $R_B^I(\psi, \theta, \phi) \rightarrow \vec{e}_T$
    4. Compute wind speed and direction estimates
        $\Psi = f(\vec{e}_T),\ v_{wind} = g(\vec{e}_T)$
    5. Remove high-frequency content from wind estimates
        $\Psi_f = Butterworth\_filter(\Psi)$
    6. Command yaw turn and check wind tolerance
        $set\_heading(\Psi_f + \pi)$
        if$(v_{wind} > max)\{start\_landing(true)\}$
end while
```

4.2.3 System Calibration and Limitations

The procedure for determining coefficients C_0 and C_1 in Equation (4.8) and evaluating the performance of these models for the CopterSonde is nearly identical to that from Section 3.1.2 of [109]. The Washington site of the Oklahoma Mesonet was used as a reference for wind speed and direction, which outputs 1 min data from an RM Young Wind Monitor. The Oklahoma Mesonet typically produces wind data every 5 min, but CASS had access to a data stream from the tower with a better time resolution. The CopterSonde was flown at a hover at 10 m near the tower, as shown in Figure 4.11, for 10–15 min at a time on several days under a variety of wind conditions for the statistical model. The aircraft inclination angles were then averaged to 1 min intervals to be consistent with the Mesonet data. Linear regression was then performed with the

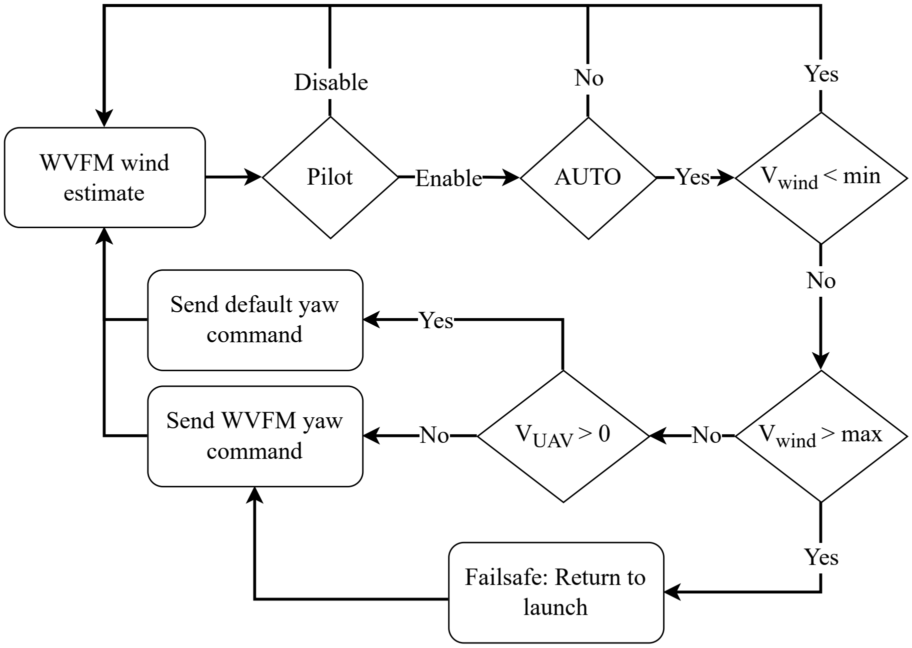

Figure 4.10: Diagram of the WVFM state machine. The state machine was used to handle the different possible scenarios during flight and perform specific tasks. The WVFM state machine overrides the yaw control of the CopterSonde and uses a decision-making process to validate the yaw commands generated by the WVFM.

input of $\sqrt{\tan\gamma}$ and Mesonet wind speed as a reference to get a transfer function of the form in Equation (4.8). This can then be applied to output wind speed estimates (Figure 4.13). In practice, compared to other sampling methodologies like radiosondes and Doppler wind lidars, this method of estimating wind speed with the CopterSonde is accurate to ±0.6 m s^{-1} from recent calibrations [110].

Similarly, the wind direction estimated by the WVFM during these flights was compared to the reference Mesonet tower. Generally, this is a more direct approach and requires no statistical modeling unless a constant offset bias is observed. The output angle for the CopterSonde as calculated from Equation (4.6) and accounting for the yaw angle ψ tends to be within 4 deg of the reference in recent calibrations [110]. Nonetheless, the calibrations done through this method only accounts for small variations (or quasi-steady state) of wind speed and direction. This is because wind does

Figure 4.11: Picture of the CopterSonde by the Washington Oklahoma Mesonet tower at KAEFS, near Purcell, Oklahoma. The CopterSonde was flown at a hover at 10 m near the tower for 10–15 min at a time on several days under various wind conditions for the statistical model of wind estimation.

not typically change significantly during the ∼15 min flight of the CopterSonde by the Mesonet tower. After calibrating the WVFM, a series of flights by the Mesonet tower were performed to validate the calibration and evaluate the performance of the WVFM. An example of wind speed and direction comparison between the CopterSonde and the Washington Oklahoma Mesonet tower at KAEFS is shown in Figure 4.12. There is a significant sampling period difference between the CopterSonde (every 0.1 s) and the Mesonet tower (every 60 s). To make a fair comparison, the CopterSonde data were averaged every 60 sec to match with the data points collected by the Mesonet tower. However, only 10 comparison points were able to be computed per flight due to the short flight autonomy of the CopterSonde-3D by the tower. To make a fair statistical comparison, several flights were conducted by the tower to increase the number of data points. Based on data accumulated from over 5 flights, the WVFM is able to achieve

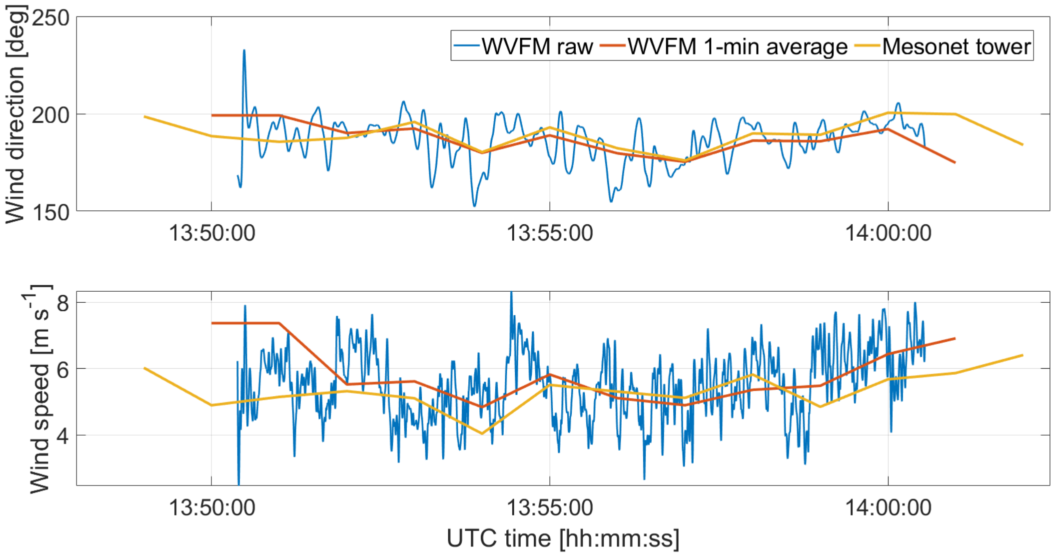

Figure 4.12: Example of wind speed and direction comparison plot between the CopterSonde and the Washington Oklahoma Mesonet tower at KAEFS. A 1-min average estimation of the WVFM was also included for a more fair comparison. Based on data accumulated from over 5 flights by the tower, the WVFM is able to achieve an accuracy of ±0.6 m s^{-1} for wind speed and 4 deg for wind direction.

an accuracy of ±0.6 m s^{-1} for wind speed and 4 deg for wind direction. To study the dynamics of the WVFM method, a flight simulation environment was used to visualize the behavior of the WVFM through strong wind shears discussed in the following section.

4.2.4 Simulation Results and Analysis

A simulation framework was developed, which was used in studying the feasibility of the WVFM estimations for wind tracking and estimating the error levels to be expected in field experiments. This framework takes into consideration the design criteria presented in the previous sections, as well as sources of error introduced by atmospheric wind turbulence. This tool was important in establishing optimal parameters of the WVFM that guarantees a stable operation with bounded errors within a defined operat-

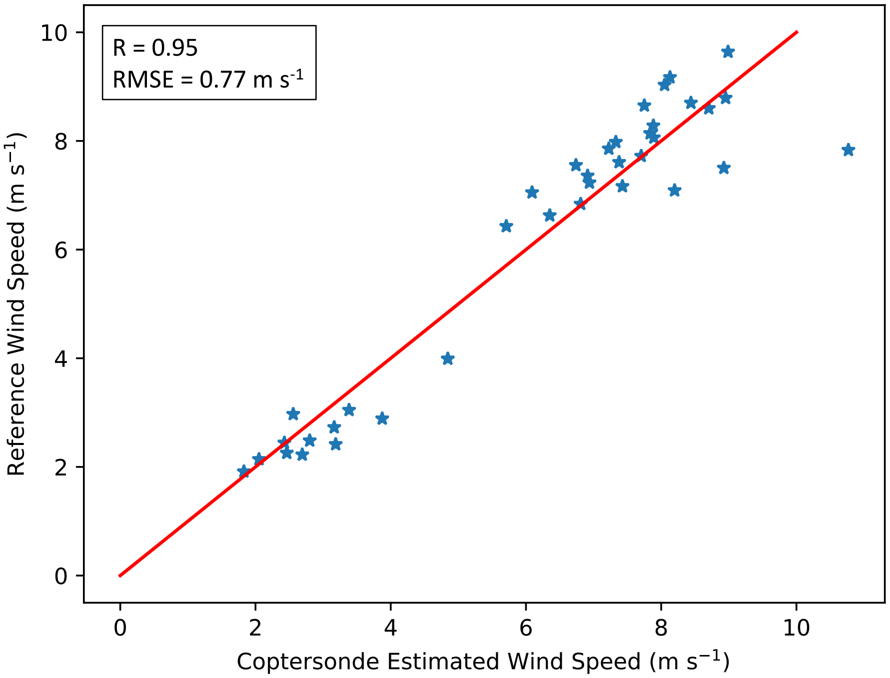

Figure 4.13: Example of CopterSonde wind speed calibration against 1 min Oklahoma Mesonet 10 m anemometer measurements. The red line represents the 1-to-1 line for reference. This statistical fit produces a correlation coefficient of 0.95 and root mean squared error of 0.77 m s^{-1} compared to the Mesonet reference.

ing range.

The simulation framework was based on the existing simulator SITL built into the ArduPilot autopilot code, which was introduced in Section 3.2.1. Changing the code compiler configuration allowed it to generate an executable file that can run the autopilot code within a simulated environment using a computer. Some parameters of the multicopter model that comes with SITL were tuned, allowing for results with better approximation to the real experimental UAV. The weight, size, inertia, and thrust coefficient were adjusted to match the CopterSonde physical properties.

The simulated environment also included simple modeling of a few atmospheric variables, such as wind and turbulence, which were adjusted as desired. By default, the wind speed is modeled using a simple logarithmic function that becomes constant

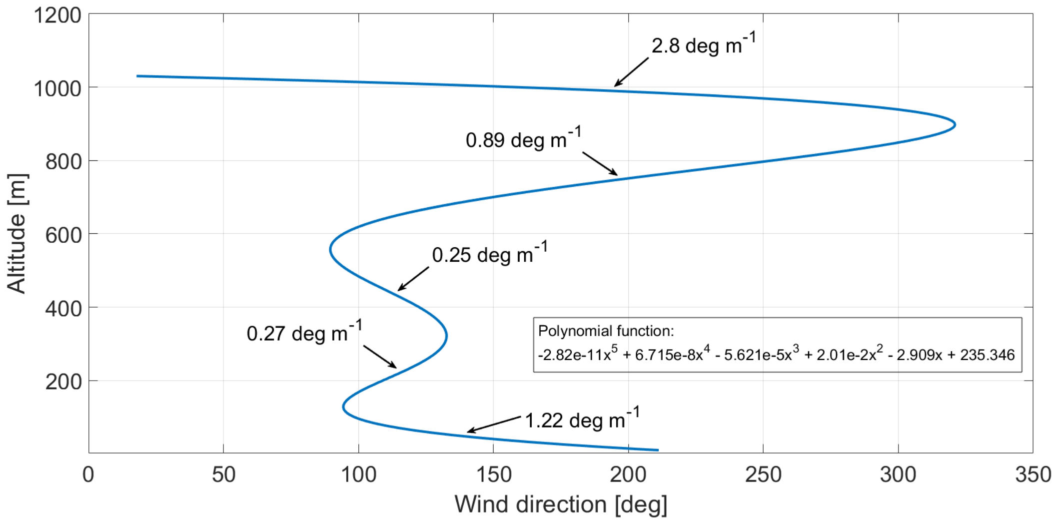

Figure 4.14: Polynomial function used to model wind shear in the simulated environment, SITL. The WVFM method is tested through the different wind shear rates along the vertical profile. This helped to determine the expected accuracy and time response of the system.

at a desired altitude, whereas the wind direction function is constant over height. A constant wind direction would not help to visualize the performance and dynamics of the WVFM. Therefore, the wind direction function was modified and replaced with a high-order polynomial equation to describe wind shear. Figure 4.14 depicts the wind shear model used to test the WVFM method. The wind profile resembles an extreme case of PBL wind shear conditions with different wind shear rates throughout the vertical profile. This helped to determine the expected accuracy and time response of the WVFM.

The dynamics of the WVFM are mainly defined by the digital causal Butterworth filter in addition to the autopilot's reaction time to position errors. Furthermore, it was possible to adjust the time response of the WVFM by changing the cut-off frequency of the digital filter. Extremely low cut-off frequencies introduced a significant delay to the wind estimation. Whereas high cut-off frequencies can cause damage to the propulsion and structure of the CopterSonde due to the abrupt "switchback" yaw rotations may produce. Thus, the goal is to find an adequate cut-off frequency that allows the CopterSonde to track and turn into the wind as fast as possible while keeping the propulsion system free of noisy command signals. Since the WVFM method works in the time domain with a constant sampling frequency of 10 Hz, same does the digital filter. Although the wind field is in the spatial domain, it can be converted to the time domain by dividing the spatial domain by the ascent speed. Consequently, the CopterSonde's speed is another variable that affects the outcome of the WVFM and must be considered in the design. Nonetheless, the climb rate of the CopterSonde, calculated in Section 3.6, was set to a fixed value of 3.8 m s^{-1} and, thus, the tuning of the WVFM depends solely on the filter's cut-off frequency. Figure 4.15 (a) shows simulation results of estimated wind direction profiles taken from the generated wind field. Different cut-off frequencies were tested, providing WVFM outcomes with different delays with respect to the actual wind direction. The CopterSonde heading offset with respect to the wind vector was computed by taking the difference between the estimated and actual wind direction profiles. The results were compared to the ideal yaw angle range, determined in Section 3.5.3, where it can be seen the filter configurations that fall within the desired range (Figure 4.15 (b)). This established the minimum cut-off frequency for the digital Butterworth filter in the WVFM algorithm. From this point, the cut-off frequency may be increased to allow the CopterSonde to react faster to small-scale wind direction changes. However, the upper bound is limited by the propulsion system's tolerance to fast commands and the stability of the yaw control. The FAA has a tedious procedure in case of accidents with UAVs while potentially getting banned from conducting flight operations. Therefore, experimenting close to the limits of the CopterSonde is risky, and hence, other methods and criteria must be considered. By inspecting Figure 4.15 (b), this shows an increase in amplitude and number of yaw switchbacks when using high cut-off frequencies. Hence, a useful criterion for the upper bound is to ob-

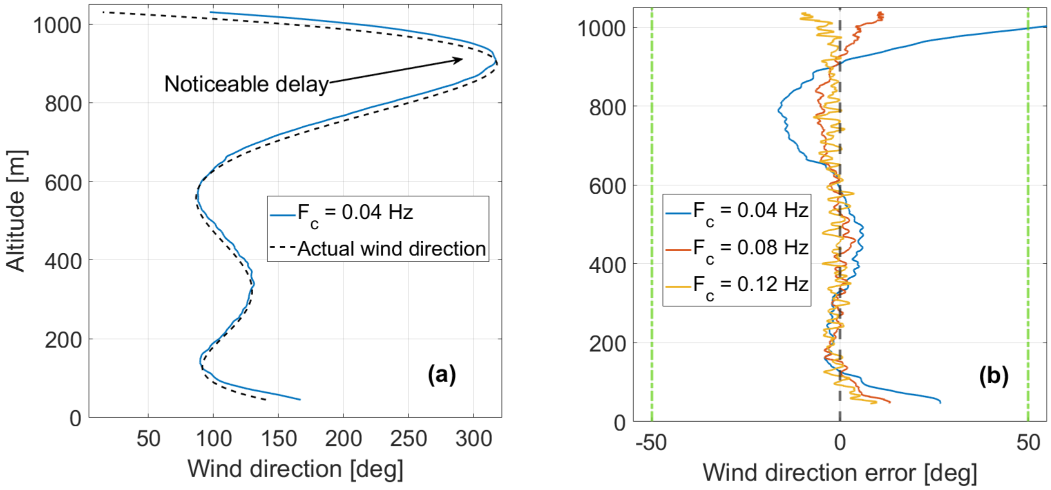

Figure 4.15: (a) Example of WVFM outcome based on simulation results using SITL and the custom wind field. Different cut-off frequencies were tested, providing WVFM outcomes with different delays with respect to the actual wind direction. (b) Difference between the estimated and true wind direction profiles shows the heading offset with respect to the actual wind field. The WVFM must be able to maintain the CopterSonde heading within the desired yaw range (dashed green lines), determined in Section 3.5.3, while producing smooth rotations with as few switchbacks as possible.

tain a smooth wind direction with as few and small yaw switchbacks as possible while maintaining the heading within the desired range. The resulting cut-off frequency was 0.06 Hz, obtained by trial and error under the simulated environment in SITL.

This procedure established the upper and lower bounds of the WVFM's cut-off frequency based on results obtained through simulation using SITL. The selection of any frequency within this range should satisfy the requirements. However, the simulated environment presents several simplifications which may not hold true for real observations and flights in the field. Therefore, the CopterSonde was first tuned in the lower region of the frequency range and then dialed up until finding an adequate yaw behavior. An adequate yaw behavior was defined as yaw corrections produced by the WVFM as fast as possible that do not overheat the propulsion system. The motor's maximum operating temperature from the manufacturer was used as a reference.

4.3 Three-dimensional Wind Estimation

Wind field estimates are a highly requested parameter among researchers in the meteorology community. The measuring of wind is critical to understanding the surface-atmosphere interactions driving the dynamic state of the PBL. Particularly, the vertical wind component is important in studying gas-tracing and atmospheric fluxes that produce spatial variability, mixing, and, thus, evolution of the PBL. These atmospheric processes directly impact human activities such as public health, transport of pollutants, wind power supply, weather forecast, air traffic control, the spread of wildfires, etc. Therefore, characterizing the dynamic state of the PBL in the micro and mesoscale domains is paramount.

Two approaches to measuring wind using multicopter UAS were found in the literature; direct and indirect estimation of the wind velocity vector [111]. Direct methods use a combination of onboard wind sensors and IMU measurements to infer wind velocity using vector math [101]. The direct method involves choosing sensors for wind sensing (anemometer, pitot tubes, multi-hole probe, etc.) that may come with different sizes and power requirements. Besides that, the addition of extra payload can greatly impact the configuration and structural layout of the UAV. On the other hand, indirect methods exploit the UAV dynamical model and flight navigation data to estimate the wind vector by employing state estimation techniques. The indirect method does not require the use of wind sensors onboard. However, their accuracy highly depends on the physical properties of the UAV as well as the complexity of the dynamical model [112]. In the literature, there are a few studies related to wind estimation using indirect methods based on dynamical models. For example, a previous study implemented a state observer based on acceleration readings of the UAV, but it was limited to indoor flights and horizontal wind velocity [113]. Similarly, a recent study developed a wind estimation method for outdoor flights but limited to steady hovering flights close to the surface [114]. Lastly, another recent study presented advances in developing a 3D wind estimation method, which proposed a modified Rayleigh aerodynamic drag equation based on curve fitting using experimental data [115]. This study was limited to wind estimation while hovering close to the surface and only using a meteorological tower for measurement comparison.

ArduPilot is a multi-platform autopilot code, and, therefore, its navigation system was designed to be hardware agnostic, meaning that no physical properties of the UAV are needed for flight control computation. In other words, the ArduPilot autopilot code is based purely on kinematic equations, while the flight control system compensates for the unknown UAV dynamics by adaptively tuning the PID gains. This allows ArduPilot to have a wider range of compatible UAVs with different sizes and weights. However, this significantly limits the ability to estimate the UAV's behavior and external disturbances fully. Nonetheless, if the physical and aerodynamic properties of the UAV are known, it is possible to augment ArduPilot's kinematic estimations using dynamical models and, thus, extract more information about the flight and surrounding environment.

In the following sections, an indirect UAV-based method for estimating 3D wind vectors using a combination of kinematic and dynamical equations tailored for the CopterSonde is presented. This study describes a way to estimate 3D winds using the CopterSonde quadcopter UAV by applying dynamical models and a state observer inspired by studies in active disturbance rejection control (ADRC) [116, 117]. Moreover, the WVFM and vertical flight pattern allowed for assumptions that further simplify the computation of wind velocity estimates. The method briefly consists in using a linear extended state observer (LESO) to estimate the drag force acting on the CopterSonde when it is flying horizontally steady. The drag force is then converted to wind velocity by employing aerodynamic friction equations which require prior characterization of the CopterSonde. Despite the similarity of the presented method with other published studies in the literature, the contribution of this work is to extend the use of the indirect 3D wind estimation method to vertical profiles up to altitudes close to 5000 ft. In addition, the characterization of the aerodynamic drag of the CopterSonde, together with wind calibration and validation of the method using Doppler wind lidars, is presented.

4.3.1 CopterSonde Dynamical Model and Assumptions

As explained in Section 4.2.1, the inertial frame I and the body frame B are used to describe the motion and orientation of the CopterSonde. However, for the study of 3D wind estimation, the origin O_I of the frame I was located at the take-off position of the CopterSonde, whereas the origin O_B of frame B remained on the center of mass of the CopterSonde. Vectors expressed in frame I can be converted to frame B, and vice-versa, using the rotation matrix deduced in Equation (4.4) and measured Euler angles (ψ, θ, ϕ). A free-body diagram of the CopterSonde was used to show the relative magnitude and direction of all forces acting upon the CopterSonde while flying in a vertical trajectory. The strictly vertical flight pattern, together with the WVFM, presented a few useful conditions when modeling the aerodynamic drag of the CopterSonde presented later in Section 4.3.4.

Assuming that the wind produces evenly distributed aerodynamic forces about the center of mass, the study of rotational motions becomes irrelevant. Therefore, the physical dimensions of the CopterSonde were ignored, and the location of all the force vectors was assumed to be acting on the center of mass. In order to further simplify the equations of motion, the following assumptions were made:

1. The UAV's body is rigid. Deflection of the airframe that may shift force locations

while flying was assumed to be negligible.

2. The center of mass and the body frame origin are coincident.

3. The propellers are rigid and the forces produced by gyroscopic precession were considered insignificant, assuming no extreme flight maneuvers.

4. The propellers' aerodynamic effects and performance were assumed unchanged while running close to the body of the CopterSonde.

These assumptions enable the decoupling of the propeller system from the rest of the UAV. Meaning that a separate model can be used to describe the dynamics of the propeller where the thrust output is an input to the UAV dynamical model.

Figure 4.16 depicts both reference frames as well as the position $\vec{P}$, velocity $\vec{V}$, thrust $\vec{T}$, drag $\vec{D}$, and weight $\vec{W} = m\vec{g}$ vectors of the CopterSonde. Other parameters used in the calculations were the mass m of the CopterSonde, Earth's gravity vector $\vec{g}$, and the wind velocity vector $\vec{U}$. According to Newton's law of motion, the translational dynamics of the CopterSonde were obtained by taking the net force in the free-body diagram and equating it to the mass times the total acceleration of the body. This results in a linear system of equations that is an approximation to the real translational motion of the CopterSonde defined in the reference frame I and shown in Equations (4.9). These equations link together the kinematics and dynamical behavior of the CopterSonde. The position $\vec{P}$ and velocity $\vec{V}$ estimated by ArduPilot were taken as measurements (first guess), whereas the input to the system is the thrust $\vec{T}$. The aerodynamic drag $\vec{D}$ was considered an external disturbance to be estimated. Other unmodeled disturbances

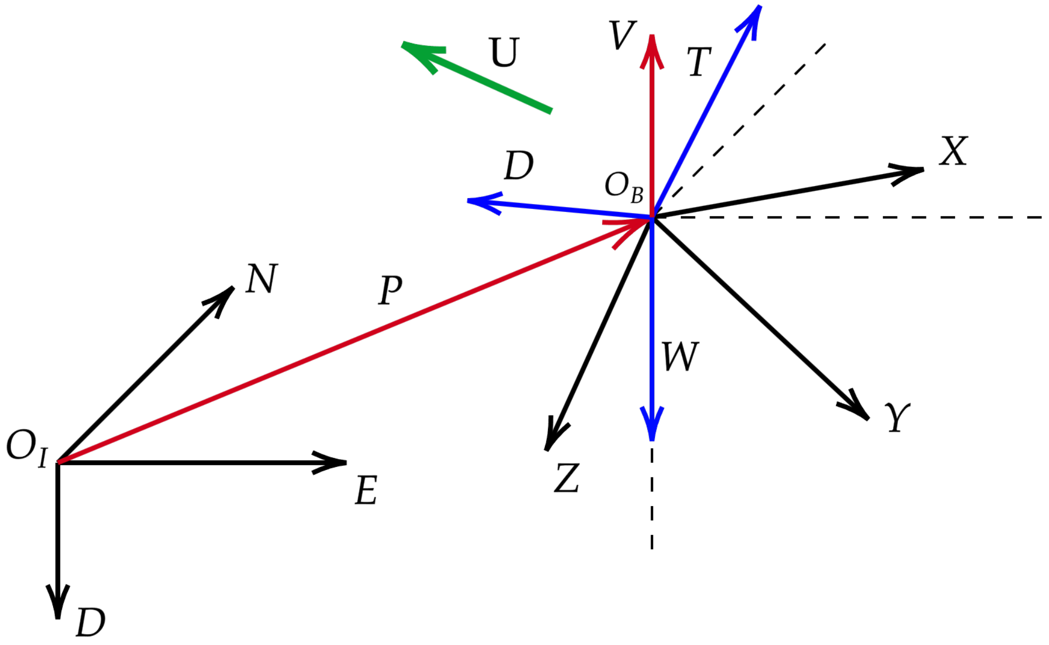

Figure 4.16: Inertial I : $\{\vec{N}, \vec{E}, \vec{D}\}$ and body B : $\{\vec{X}, \vec{Y}, \vec{Z}\}$ reference frames convention used by ArduPilot and adopted for this study. The origin O_I of the frame I is located at the take-off position, whereas the origin O_B of frame B remains on the center of mass. The kinematics of reference frame B is fully defined by its position $\vec{P}$, velocity $\vec{V}$, and Euler rotation angles (ψ, θ, ϕ) with respect to the fixed frame I. The free-body diagram of the CopterSonde is also shown in blue vectors. Thrust $\vec{T}$, drag $\vec{D}$, and weight $\vec{W} = m\vec{g}$ are the main forces acting upon the CS. The wind velocity $\vec{U}$ is shown in green.

and uncertainties of the system are represented by the term ν.

$$\begin{cases} \dot{\vec{P}} = \vec{V} \\ \dot{\vec{V}} = \vec{g} + \frac{1}{m} R^I_B \vec{T} + \frac{1}{m} \vec{D} + \nu \end{cases} \tag{4.9}$$

Equations (4.9) is a linear time-invariant (LTI) system which has the following form in matrix notation:

$$\begin{cases} \dot{\mathbf{x}} = A\mathbf{x} + B\mathbf{u} \\ \mathbf{y} = C\mathbf{x} \end{cases} \tag{4.10}$$

Where **x** is the state array of the system at a given time, **u** is the input array to the system, **y** is the output of the system, and A, B, and C are the state, input, and output matrices, respectively. These parameters will be defined after introducing the state observer in Section 4.3.3. Furthermore, Equations (4.9) can be broken down into three different scalar systems, Equations (4.11–4.13), each representing the dynamical motion of the CopterSonde along the principal axes of I. This operation is valid if it is assumed that the aerodynamic drag effects along each axis are independent and decoupled from the others.

$$\begin{cases} \dot{P}_N = V_N \\ \dot{V}_N = \frac{1}{m}(R_B^I \vec{T})_N + \frac{1}{m} D_N + \nu_N \end{cases} \tag{4.11}$$

$$\begin{cases} \dot{P}_E = V_E \\ \dot{V}_E = \frac{1}{m}(R_B^I \vec{T})_E + \frac{1}{m} D_E + \nu_E \end{cases} \tag{4.12}$$

$$\begin{cases} \dot{P}_D = V_D \\ \dot{V}_D = g + \frac{1}{m}(R_B^I \vec{T})_D + \frac{1}{m} D_D + \nu_D \end{cases} \tag{4.13}$$

A quick inspection of Equations (4.9) in advance shows that the input array **u** can be defined as equal to $\vec{g} + \frac{1}{m} R_B^I \vec{T}$ assuming that the thrust vector can be directly measured. The following section describes the process of calculating the thrust and other forces of the propeller employing a dynamical model.

4.3.2 Propeller Model

A propeller blade is essentially an airfoil rotating at subsonic speeds and producing lift and drag, similar to an aircraft wing. Varying the angular speed Ω of the propellers individually allows the CopterSonde to change the total thrust and moments and, hence, its attitude and position as desired. In order to complete the UAV model presented in the previous section, a separate parametric model must be used to estimate the thrust F_T and drag F_H generated by the motion of the propeller. However, given that the study of aerodynamic principles and modeling of propellers is highly complex, it falls outside the scope of this work. Therefore, the guidelines, methods, and formulae presented in [118, 119] were adopted and employed for the mathematical description of the CopterSonde's propellers. Their method is claimed to be computationally efficient while still providing highly accurate estimations. The models were derived using explicit expressions based on the most salient features listed below [119].

1. N_b is the number of blades, whereas R is the radius of the propeller.
2. θ_{tip} and c_{tip} are the angle of attack and width of the propeller's tip, respectively.
3. δ represents the fraction of the propeller that does not contribute to the generation of thrust and drag.
4. $(c_{l,0}, c_{l,\alpha})$ and $(c_{d,0}, c_{d,\alpha})$ are coefficients of linear equations that describe the lift and drag coefficients of the propeller, respectively.

Although some of these parameters can be physically measured from the real propeller, they actually may differ from the real one. This is because the propeller model is a template that must be adjusted through experimentation and characterization. The parameters can be identified using supervised gray-box fitting from experimental data, i.e., using a wind tunnel. However, given the lack of resources and facilities, a proper characterization of the propellers could not be conducted. Instead, the propeller parameters, listed in [119], that approximate the dimensions and characteristics of the CopterSonde's propellers were selected and applied to the model. This may carry some

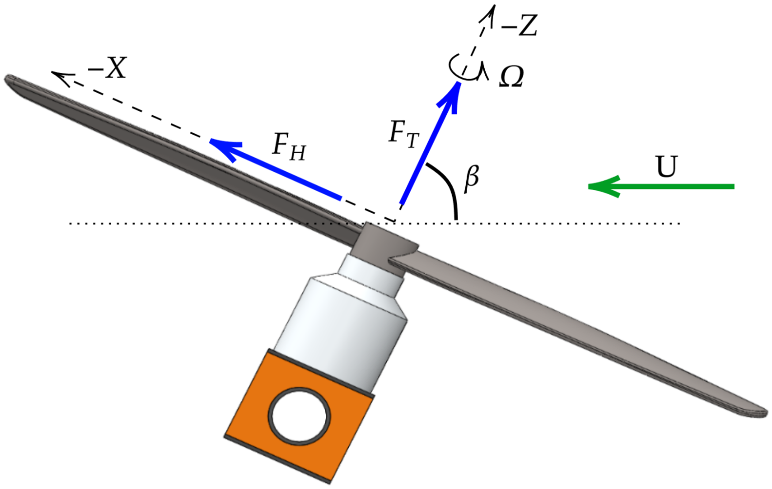

Propeller	N_b	R	$c_{l,0}$	$c_{l,\alpha}$	$c_{d,0}$	$c_{d,\alpha}$	δ	θ_{tip}	c_{tip}
APCE-10×7	2	0.14	0.75	6.6	0.12	2.8	0.12	0.21	5.7e-3

Figure 4.17: Propeller diagram illustrating the thrust F_T and drag F_H force vectors produced by the propeller rotating with an angular speed Ω. The propeller dynamics are also affected by incident wind, estimated by the WVFM, with velocity $\vec{U}$ and forming an angle β with the vertical axis. The included table shows the parameters used for the propeller model, which approximates the performance of the T-Motor CF 11×5.5 propeller installed on the CopterSonde. Errors introduced through this approximation may be partially corrected after calibration.

errors in the final 3D wind estimation results. However, it is expected that the calibration process, discussed later in Section 4.3.4, could partially absorb these errors.

Although the propeller model is able to resolve all forces and moments acting on the propeller, the total thrust F_T and drag F_H is all that is required for the 3D wind estimation based on the assumptions made in the Section 4.3.1. Figure 4.17 shows the reference frame used for vector calculation in addition to the body-free diagram of the propeller. The set of parameterized expressions that computes (F_T, F_H) as a function of intake airflow velocity V_{in}, angle of incidence β with respect to airflow velocity, and angular velocity Ω are summarized in the set of Equations (4.14) [119].

$$\begin{cases} \lambda_c = \frac{V_{in}\cos\beta}{\Omega R}, \quad \mu = \frac{V_{in}\sin\beta}{\Omega R}, \quad \lambda = \lambda_c + \lambda_i, \quad \sigma = \frac{N_b c_{tip}}{\pi R} \\ \lambda_i = \frac{1}{8}\{-4\lambda_c + c_{l,\alpha}\sigma(\delta - 1) + [16\lambda_c^2 + 8c_{l,\alpha}(\delta - 1)\lambda_c\sigma + \\ \qquad \frac{1}{\delta}(\delta - 1)\sigma(-8c_{l,0}\delta(1 + \delta) + c_{l,\alpha}(c_{l,\alpha}(\delta - 1)\delta\sigma - \\ \qquad 8(2\delta + \mu^2)\theta_{tip})) - 8c_{l,0}\mu^2\sigma\ln\delta]^{0.5}\} \\ C_{FT} = \frac{\sigma}{2\delta}\{(1 - \delta)[c_{l,0}\delta(1 + \delta) - 2c_{l,\alpha}\delta(\lambda - \theta_{tip}) + c_{l,\alpha}\mu^2\theta_{tip}] - \\ \qquad c_{l,0}\delta\mu^2\ln\delta\} \\ C_{FH} = \frac{\mu\sigma}{2\delta}\{(1 - \delta)[2c_{d,0}\delta + \theta_{tip}((c_{l,\alpha} - 2c_{d,\alpha})\lambda + 2c_{d,\alpha}\theta_{tip})] - \\ \qquad c_{l,0}\delta\lambda\ln\delta\} \\ F_T = 2C_{FT}\rho\pi\Omega^2R^4, \qquad F_H = 2C_{FH}\rho\pi\Omega^2R^5 \\ \vec{T} = \vec{F_T} + \vec{F_H} \end{cases} \tag{4.14}$$

Where λ_c is the advance ratio, μ is the climb ratio, λ_i is the induced inflow ratio, and C_{FT} and C_{FH} are the normalized thrust and drag forces, respectively. The incidence angle β is equal to the tilt γ of the CopterSonde and measured by the IMU. The angular speed of the rotor Ω is measured by the ESC. However, the airflow velocity V_{in} is unknown, which is an issue because it is equal to the desired wind velocity estimate U. To solve this, the first guess of V_{in} was made using the output of the WVFM. Then, the subsequent computations of the wind estimate U use the previous wind estimate output as V_{in}. Another limitation when using the presented propeller model is that V_{in} must always be positive. In other words, the model breaks when the V_{in} is opposite to the propeller's induced airflow. Therefore, the wind estimation method is limited to estimating wind velocities only when the CopterSonde is ascending. Moreover, it is assumed that the speed of any updraft sensed by the CopterSonde is slower than the ascent speed, deduced in section 3.6, to avoid similar problems.

The following section introduces the state observer for estimating the external disturbances upon the CopterSonde that will later lead to the estimation of 3D wind velocities.

4.3.3 Linear Extended State Observer (LESO) Design

In modern control theory, the state observer is used to estimate state variables that are unreachable for direct measurement. If the available measured outputs **y** from Equation (4.10) capture enough information about the system's dynamics, the full state variable can be reconstructed using a system model [120]. The basis for ADRC is a state observer that treats, unifies, and rejects actual disturbances and model uncertainties altogether, such that it relieves the flight control loop of any unwanted signals [116]. This way, only a coarse process model is sufficient to design a control loop that promises good robustness against process variations and easy tuning. However, for the purpose of this work, only the techniques for disturbance and model uncertainty estimation of the ADRC were borrowed to develop the 3D wind estimation method. Moreover, the linear case of ADRC is equivalent to a special case of classical state space representation with added disturbance estimation based on linear dynamical models. Regardless of the actual plant process, the linear ADRC (LADRC) leaves all modeling errors to be treated as disturbance [117].

A special case of state observer within the LADRC method is the LESO. The LESO uses an extension of the proposed dynamical model to estimate unknown inputs or faults by reconstructing the disturbance through error-driven methods based on real observations and estimates [121]. After deducing the scalar CopterSonde dynamical models for each axis in Equations (4.11–4.13), the formulation of the LESO starts by comparing the proposed models with an equivalent integral chain system of the form shown in Equation (4.15) and identifying each term [116, 121].

$$\begin{cases} \dot{x}_1 = x_2 \\ \dot{x}_2 = f(x_1, x_2, \nu(t), t) + bu \\ \mathbf{y} = C\mathbf{x} + \eta \end{cases} \tag{4.15}$$

Where $\mathbf{x} = [x_1 \; x_2]^T \equiv [P \; V]^T$ are the state variables, $u \equiv \vec{g} + \frac{1}{m} R_B^I \vec{T}$ is the control input, $b = 1$ is a system parameter that scales the input, **y** is the system output which can be measured, η is the measurement noise. Given that position $\vec{P}$ and velocity $\vec{V}$ are parameters measured by the CopterSonde, then C is equal to a 2×2 identity matrix. The multivariable function $f(x_1, x_2, \nu(t), t) \equiv \frac{1}{m}\vec{D} + \nu$ is the uncertain function that describes the combined external disturbances and model uncertainties. Besides the aerodynamic drag $\vec{D}$, other uncertainties that are lumped together in the ν term are unmodeled torque and moment dynamics of the propeller, flexing of the airframe, wake turbulence trailing behind the CopterSonde, etc. [121]. However, it is assumed that the uncertain function is approximately equal to $\vec{D}$ as long as the aerodynamic drag is much larger than the rest of the model uncertainties $\frac{1}{m}D >> \nu$.

The uncertain function $f(x_1, x_2, \nu(t), t)$ is treated as an additional state variable in the framework of LESO [116]. This way, the augmented or extended system is capable of providing estimates of the unknown parameters as long as the system remains observable. Let $x_3 = f(x_1, x_2, \nu(t), t)$ and $\dot{x}_3 = h(t)$, where $h(t)$ is the unknown rate of change of the disturbances, then the systems in Equations (4.11–4.13) take the following form,

$$\begin{cases} \dot{x}_1 = x_2 \\ \dot{x}_2 = \frac{1}{m}x_3 + u \\ \dot{x}_3 = h(t) \\ \mathbf{y} = C\mathbf{x} \end{cases} \tag{4.16}$$

In matrix notation, the system of Equations (4.16) is formulated as follows,

$$\begin{cases} \dot{\mathbf{x}} = A\mathbf{x} + B\mathbf{u} \\ \mathbf{y} = C\mathbf{x} \end{cases} \quad \text{where } A = \begin{bmatrix} 0 & 1 & 0 \\ 0 & 0 & \frac{1}{m} \\ 0 & 0 & 0 \end{bmatrix}, B = \begin{bmatrix} 0 \\ 1 \\ 0 \end{bmatrix}, C = \begin{bmatrix} 1 & 0 & 0 \\ 0 & 1 & 0 \end{bmatrix} \tag{4.17}$$

Subsequently, the state observer was constructed following the design process shown in [120]. The resultant state observer for the presented CopterSonde model on each principal axis is given below in matrix notation,

$$\begin{cases} \dot{\hat{\mathbf{x}}} = (A - LC)\hat{\mathbf{x}} + B_a \begin{bmatrix} u \\ h \end{bmatrix} + L\mathbf{y} \\ \mathbf{y} = C\hat{\mathbf{x}} \end{cases} \tag{4.18}$$

where $\hat{\mathbf{x}} = [P\ V\ D]^T$ is the estimate of the state variable $\mathbf{x}$ and the matrices are defined as,

$$A = \begin{bmatrix} 0 & 1 & 0 \\ 0 & 0 & \frac{1}{m} \\ 0 & 0 & 0 \end{bmatrix}, B_a = \begin{bmatrix} 0 & 0 \\ 1 & 0 \\ 0 & 1 \end{bmatrix}, C = \begin{bmatrix} 1 & 0 & 0 \\ 0 & 1 & 0 \end{bmatrix}, \text{ and } L = \begin{bmatrix} \beta_{p1} & \beta_{v1} \\ \beta_{p2} & \beta_{v2} \\ \beta_{p3} & \beta_{v3} \end{bmatrix}$$

The error-correcting portion of the system is governed by the observer gain matrix L.

This is reflected in the error dynamics of the system expressed as $\dot{\tilde{\mathbf{x}}} = (A - LC)\tilde{\mathbf{x}} - L\eta$ where $\tilde{\mathbf{x}} = \mathbf{x} - \hat{\mathbf{x}}$ is the error. The eigenvalues of $(A - LC)$ must be located on the left side of the s-plane for the error dynamics to tend to zero [120]. However, a large observer gain may amplify the measurement noise η and increase the error. Therefore, the L gain is chosen based on a trade-off between how fast the observer tracks the state variables and how sensitive it is to the sensor noises. The L gain was determined using formulae deduced in [122], where the elements of the matrix are defined as,

1. Position error correction: $\beta_{p1} = 3\omega_{po}$, $\beta_{p2} = 3\omega_{po}^2$, and $\beta_{p3} = \omega_{po}^3$,
2. Velocity error correction: $\beta_{v1} = 3\omega_{vo}$, $\beta_{v2} = 3\omega_{vo}^2$, and $\beta_{v3} = \omega_{vo}^3$.

The parameters ω_{po} and ω_{vo} are the observer bandwidth for position and velocity, respectively. In general, the larger the bandwidth of the LESO the faster the disturbance is tracked and observed. A common approximation is to choose $\omega_o = 3 \sim 5\omega_c$ [122]. The parameter ω_c is the control loop bandwidth of the autopilot in which it operates to correct errors in a stable manner. This was obtained by inspecting the PSD of the position and velocity measurements of the CopterSonde. These were computed using flight data recorded in windy conditions, the results are shown in Figure 4.18. As a result, the bandwidth of the observer must be in the range of $\omega_{po} = \omega_{vo} \approx 2.8 - 4.7$ rad s^{-1}.

The matrix B was augmented to B_a with the introduction of the new input h. Given that it is impossible to know the rate of change of aerodynamic drag h beforehand, then h was set to zero. This is correct under the assumption that the rate of change of wind sensed by the CopterSonde is small throughout the vertical profile. Like this, the drag state variable in Equation (4.18) reduces to a simple error integrator.

This completes the design of the LESO. Subsequently, the LESO was discretized using a sampling frequency of 10 Hz, equal to the logging rate of the CopterSonde, using the zero-order hold (ZOH) method for code implementation in MATLAB.

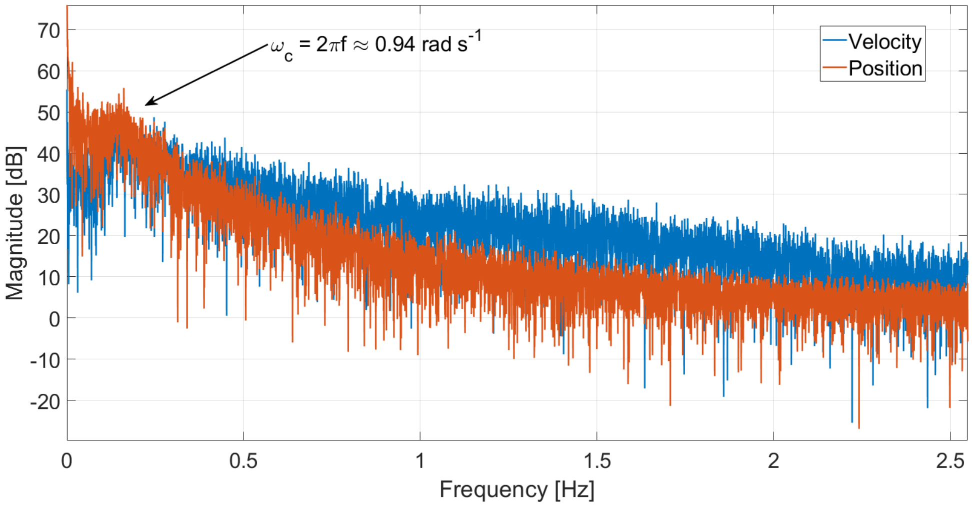

Figure 4.18: Power spectral density of velocity and position measurements taken while the CopterSonde performed vertical profile flights in windy conditions. After fine-tuning the autopilot, the bandwidth of the control loop was found to be $\omega_c \approx 0.94$ rad s^{-1}.

4.3.4 Aerodynamic Drag Modeling

A typical drag model used for translating aerodynamic forces into wind speed is the well-known Rayleigh equation as previously introduced in Equation (4.7) from Section 4.2.1. Theoretically, this equation is only valid when the fluid directly impinges onto the projected area A_p. Besides this, the fluid must come to a full stop at the surface, generating stagnation pressure over the whole area and producing a net force as a consequence. However, not all real objects present this exact behavior, and other types of boundary layers may be formed over the surface depending on the geometry. Given that the CopterSonde presents a complex shape with rough surfaces from 3D printing, it is not expected to strictly follow the power law in Rayleigh's drag equation. Therefore, another accepted representation of the relationship between D and U is to make the exponent a variable allowing for a more accurate approximation [123]. The following equation is the modified Rayleigh equation,

$$D = \frac{1}{2}\rho c_d A_p U^{1/b} \quad \text{or} \quad U = c_d^{-1}\left(\frac{2D}{\rho A_p}\right)^b \tag{4.19}$$

where c_d is the drag coefficient, ρ is the humid air density, and b is the variable exponent. The left-hand equation is in the standard form, while the right-hand equation is for calibration purposes using curve fitting. Equation (4.19) takes the form of Rayleigh's drag equation if the exponent $1/b$ is equal to 2. From this point, the modifications made to the aerodynamic drag equation were tailored to the CopterSonde design, as well as the aerodynamic advantages that come with the usage of the WVFM.

Assuming that the WVFM aligns the CopterSonde with the wind field fast enough, then the side drag and, hence, the side area of the CopterSonde can be neglected. This way, only the projected front, and top areas A_F and A_T, respectively, of the CopterSonde were considered in the wind speed calculations. Moreover, the projected area A_p is a function of pitch θ which was approximated to a linear equation of the form $A_p = m\theta + b$ where $m = 2(A_T - A_F)/\pi$ and $b = A_F$. The areas A_T and A_F were measured by taking the dimensions of the CopterSonde CAD model using SolidWorks software.

Rayleigh's drag equation depends on air density or, more specifically, moist air density, which includes water vapor. Given that the CopterSonde carries thermo-hygrometers and barometers, the calculation of moist air density becomes straightforward and can be accounted for in the wind calculations. The humid air density ρ is described as follows,

$$\begin{cases} \rho = \frac{p_d M_d + p_v M_v}{RT} \\ p_v = H p_{sat} \\ p_{sat} = p_a \exp(13.3185t - 1.9760t^2 - 0.6445t^3 - 0.1299t^4) \\ t = 1 - \frac{373.15}{T} \end{cases} \tag{4.20}$$

where p_d is the pressure of dry air, p_v is the pressure of water vapor, R is the universal gas constant, T is the air temperature, H is the relative humidity, and p_a is the standard pressure at sea level [68, 86].

The remaining parameters to be determined in Equation (4.19) are the drag coefficient c_d and the exponent b. For this, a calibration procedure was established consisting of vertical profiles alongside Doppler wind lidars (DWL). The relationship between wind measurements of the DWL and aerodynamic drag forces estimated by the LESO is described by the right-most expression in Equation (4.19). Consequently, the drag coefficient c_d and the exponent b were obtained through curve fitting method. For the CopterSonde-3D, these values were $c_d = 0.678$ and $b = 0.979$ for the vertical component, and $c_d = 5.363$ and $b = 0.414$ for the horizontal component. The vertical case exhibits a linear behavior ($b \approx 1$), whereas the horizontal component is closer to the original quadratic Rayleigh expression ($b \approx 0.5$).

Given that the CopterSonde is moving at a constant speed throughout the vertical profile, this creates additional relative motion of the air beside the wind velocity. The airspeed vector V_S of the CopterSonde is equal to the sum of the CopterSonde's velocity V_D and the wind velocity vector U. Subsequently, the wind velocity U is computed from the velocity vector triangle formed by said vectors. The drag vector D is assumed to be parallel to V_S. Therefore, magnitude of V_S is calculated using Equation (4.19).

Lastly, the wind vector is obtained by taking the difference between the V_S and V_D.

4.4 Results and Comparison with other Meteorological Instruments

Experiments to further evaluate the performance of the WVFM and LESO methods were conducted at KAEFS in Purcell, OK, USA, where the Washington Oklahoma Mesonet tower (WOMT) is located as previously described in section 4.2.3. In addition to the Mesonet tower, a Mobile Mesonet (MM) [124] upgraded with two DWLs provided by the National Severe Storm Laboratory (NSSL) was brought to KAEFS for wind profile comparison with the CopterSonde. Both DWLs mounted on the MM have the same specifications as the DWL installed on NSSL's Collaborative Lower Atmospheric Mobile Profiling System (CLAMPS), which is a Halo Photonics Streamline scanning Doppler Wind Lidar [125]. The advantage of this system is its ability to sample vertical columns of air almost instantaneously with high spatial and temporal resolution compared to radiosondes. Based on previous studies, it was found that co-located wind retrievals from CLAMPS and radiosondes compare well with correlations of 0.984 for wind speed and 0.899 for wind direction [110]. The MM and CLAMPS also have the ability to launch radiosondes as it has a dedicated compartment for helium tanks and an antenna for signal reception [126]. The radiosondes used for these experiments were Vaisala Radiosonde RS41-SGP sounding system with general specifications included in Table 4.3 according to the manufacturer [127].

To emphasize the performance evaluation of the CopterSonde wind retrievals, windy days were chosen to collect observations. A total of 16 CopterSonde profiles co-located with radiosonde, DWLs, and WOMT were conducted on 4 different days in June 2021 and June 2022. The weather at KAEFS was typical of a summer season

Table 4.3: Vaisala Radiosonde RS41-SGP general specifications according to the manufacturer [127]. This radiosonde was used as a benchmark for intercomparisons with CopterSonde kinematic and thermodynamic measurements of the PBL.

Measurement	Range	Accuracy	Response time	Resolution
Temperature	-90–60 °C	0.3 °C	0.5 s	0.01 °C
Humidity	0–100 %	4 %	$<$ 0.3 s @ 20 °C	0.1 %
Pressure	$>$ 3 mb	1 mb	–	0.01 mb
Wind speed	$<$ 160 m s^{-1}	0.15 m s^{-1}	–	0.1 m s^{-1}
Wind direction	0–360 deg	2 deg	–	0.1 deg

day with temperatures in the mid-20s °C, mainly southerly winds at 4–10 m s^{-1}, and partly sunny with scattered high clouds. In a series of independent trials, the CopterSonde was programmed to do vertical profiles up to 1500 m AGL while keeping a horizontal distance of approximately 10 m from the DWLs. This horizontal gap was necessary to prevent the CopterSonde prop wash from interfering with the DWL measurements. Figure 4.19 shows the experimental layout at KAEFS, including some of the staff and students that participated in the experiment. Every CopterSonde flight at KAEFS was conducted in compliance with the FAA's Certificate of Authorization (COA) described in Appendix B. During the flight operation period, the two DWLs on the MM were continuously running and collecting observations, each configured with a different scanning mode. The scan strategy used in one DWL consisted of an advanced velocity azimuth display (AVAD) [128] and slightly modified for CLAMPS. The AVAD was operating at 70 deg elevation to gather profile of wind speed and direction every 5 s. The second DWL was running Doppler Lidar Fixed Point (DLFP) mode consisting of vertical stares to collect vertical wind velocities with a time period of 2 s. Both DWLs were programmed to take observations with a range gate of 18 m. The CopterSonde takes approximately 7 min to reach the target altitude of 1500 m and produce a single sounding. Whereas both DWLs are able to collect several wind profiles during this pe-

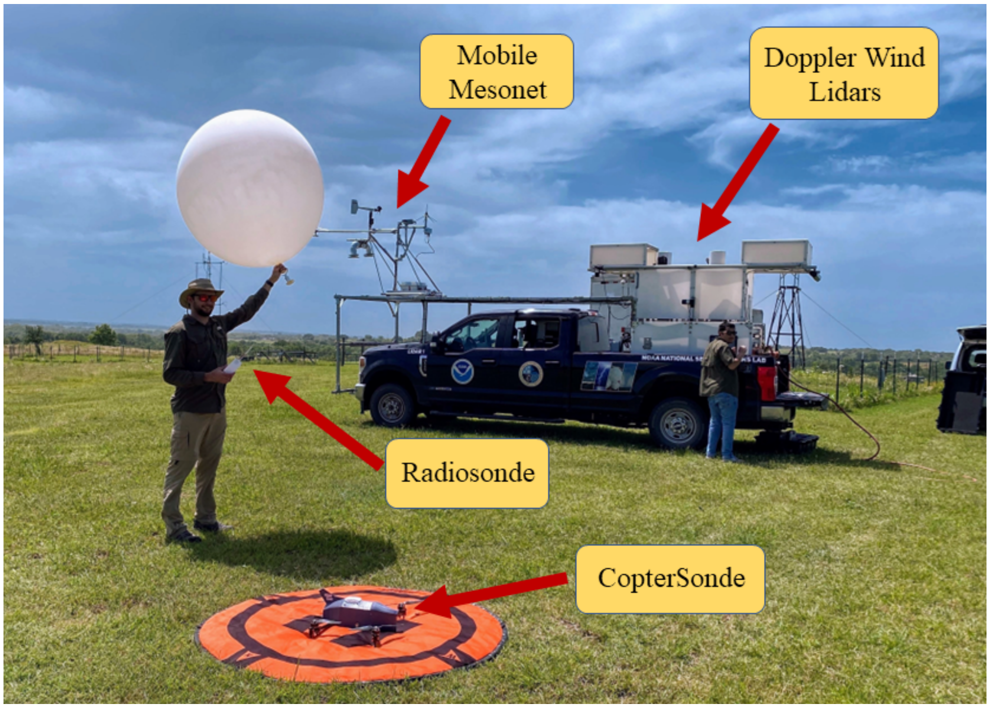

Figure 4.19: Experimental layout at KAEFS in Purcell, OK, USA. The CopterSonde was programmed to do vertical profiles up to 1500 m while keeping a horizontal distance of approximately 10 m from the MM and DWLs. Data collected from this experience were used to compare the kinematic and thermodynamic measurements of the CopterSonde with observations from Radiosonde and Doppler Wind Lidar. Every CopterSonde flight at KAEFS was done in compliance with the Certificate of Authorization issued by the FAA and described in Appendix B.

riod of time. Therefore, interpolation of the DWL wind data was performed to match with those of the CopterSonde at a given height and time to make a fair comparison. A similar process was done with the radiosonde data to match the number of data points collected with the CopterSonde.

Identifying and characterizing differences between platforms statistically is important to make conclusions about the weather measurement quality of the CopterSonde relative to conventional instruments. It was assumed that the DWLs and radiosonde used in this study are proven systems that can be used as benchmarks for atmospheric measurement comparisons. However, it is known that each platform presents different

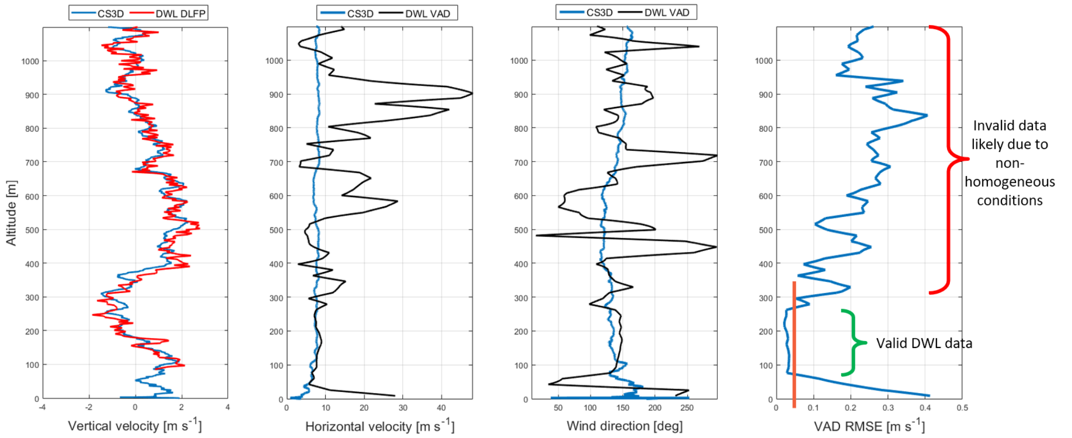

Figure 4.20: Single 3D Wind profile taken with the CopterSonde (CS) and DWL. (a) Vertical wind velocity. (b) Horizontal wind speed between. (c) Wind direction. This particular example shows a large spread and outliers in (a) and (b), likely due to non-homogeneous atmospheric conditions, as shown in the RMSE plot on the far right. The threshold (orange line) to discard inaccurate lidar measurements based on the RMSE values was defined on a case-by-case basis. As a result, this shows how the CopterSonde *in situ* measurements help to complement remote measurements taken with gound-based instruments whenever these get impaired.

assumptions while also being affected by sources of error. For instance, the AVAD scan assumes that the wind field is horizontally homogeneous and stationary in order to calculate horizontal winds. This, combined with a low concentration of scatterers in the air, may produce large errors in the estimates when the assumptions do not hold true in the PBL [110]. Thus, there were days when the AVAD was severely affected, producing wind profiles that had regions with extremely large errors. Figure 4.20 shows evidence of this problem, whereas the CopterSonde wind estimations indicated a different pattern, particularly for horizontal winds. The approach used to identify erroneous lidar measurements was to inspect the RMSE values produced by the AVAD. High RMSE indicates that homogeneous wind field assumption is violated. Therefore, a threshold was established on a case-by-case basis to discard DWL data affected by these unfavorable conditions. From this point forward, the regions with large outliers in the DWL

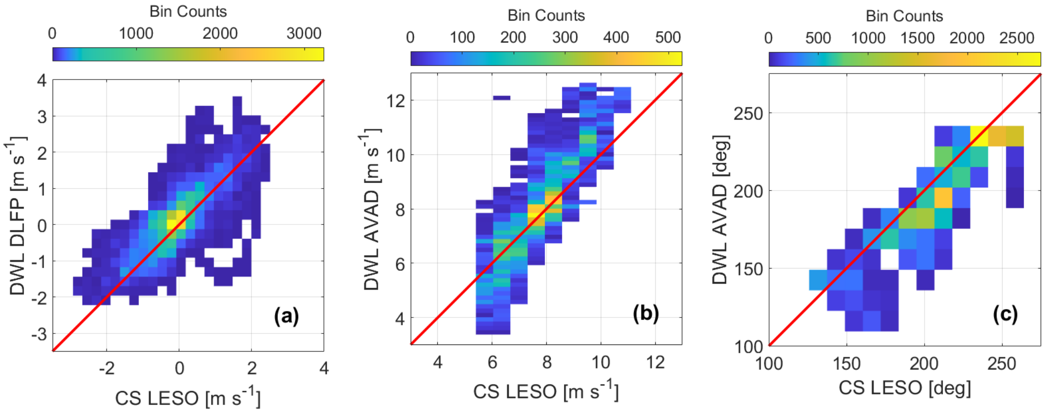

Figure 4.21: Cumulative scatter plots showing the relationship of the parameters estimated by LESO and DWL and the number of occurrences using a color map found on the top of each plot. A total of 16 different CopterSonde profiles were combined to produce the results shown here. The large spread and outliers due to the poor signal-to-noise ratio of the DWL were removed before the statistical analysis. The red line in each plot indicates a one-to-one perfect association. The total number of data points evaluated for each case was N=31386. (a) Vertical wind velocity with R=0.791, MD=-0.197 m s^{-1}, RMSE=0.492 m s^{-1}, and SD=0.451 m s^{-1}. (b) Horizontal wind speed with R=0.90, MD=-0.287 m s^{-1}, RMSE=1.025 m s^{-1}, and SD=0.984 m s^{-1}. (c) Wind direction with R=0.91, MD=11.3 deg, RMSE=17.36 deg, and SD=13.179 deg.

data were manually removed in order to make a fair statistical comparison. As a result, this shows how the *in situ* measurements of the CopterSonde can help to complement remote measurements whenever the other gets degraded by instrument limitations.

Additionally, radiosondes drift with the wind causing measurements to be far from the launch point horizontally. Consequently, the radiosonde may traverse temperature and moisture gradients in space that differs from the CopterSonde and DWL profiles. In summary, there are several causes known *a priori* for measurement differences among the presented instruments that are virtually unavoidable in practice. Although the following measurement comparisons may not be ideal given the platform limitations, it is the best approach available. Therefore, any differences in the data presented below contain three components: instrument inaccuracy, inability to sample the same point in space at the same time, and differences in the measurement technique itself

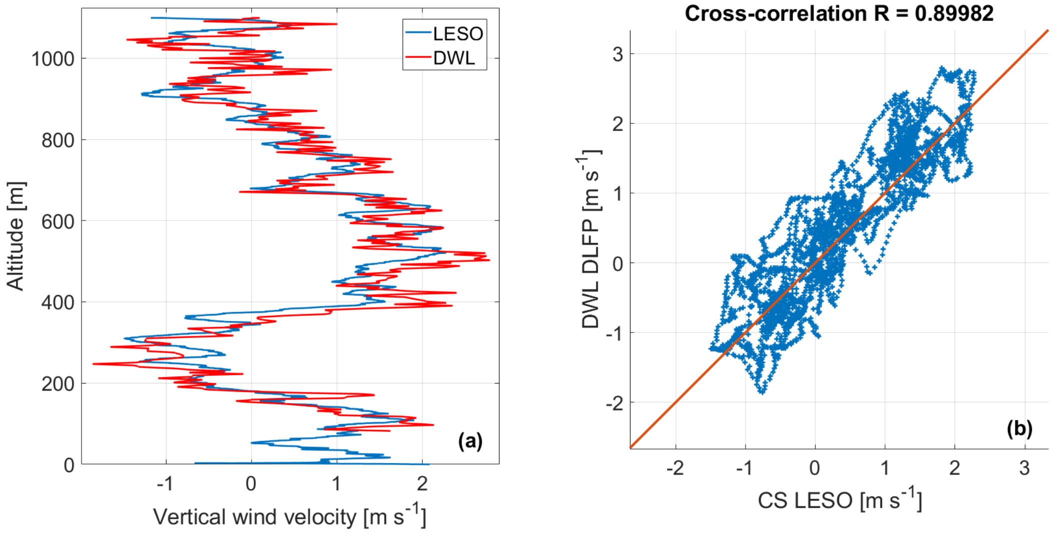

Figure 4.22: (a) Example of vertical wind profile produced by LESO technique (blue) and measured with a DWL (red) up to a height of 1500 m AGL. Updraft, downdraft, and vertically stationary air parcels were observed in this particular profile. (b) Respective scatter plot for further comparison together with the computed correlation. The straight red line indicates the one-to-one line with perfect association.

[110]. The statistical tools used to quantify the measurement differences between platforms were the mean difference (MD), RMSE, and correlation coefficient (R). For the radiosonde case, the MD over height may be pointless for comparison since the atmospheric conditions around the radiosonde change as it ascends and drifts away with the wind. Nonetheless, the radiosonde and DWL profiles were considered as ground truth for this study under the assumption that all platforms were sampling the same column of air within the same time frame. Furthermore, the standard deviation (SD) of the CopterSonde profiles was computed using the radiosonde and DWL profiles as true observations at each height.

To begin with the analysis of the results, the kinematic estimations of the CopterSonde LESO and DWL are discussed. Figure 4.21(a) shows binned scatter plots of vertical wind, wind speed, and wind direction, respectively, by combining all 16 CopterSonde profiles. This reveals the degree of correlation among the CopterSonde and

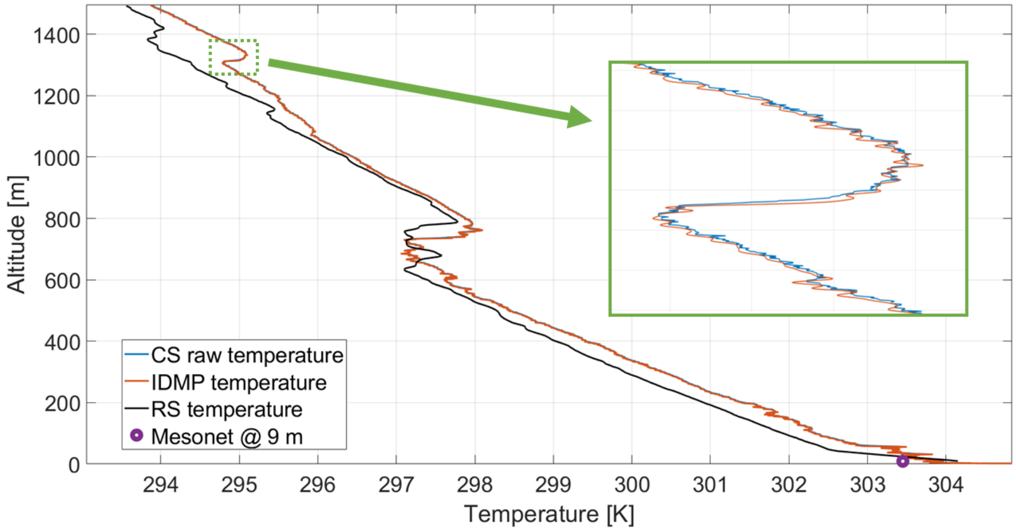

Figure 4.23: Temperature profile of the CopterSonde (CS) and radiosonde (RS) up to a height of 1500 m AGL. Two small PBL thermal inversions were captured by both systems. The second inversion is shifted due to the radiosonde traversing the layer at a different location far from the launch point. The CopterSonde temperature data was processed using the IDMP technique for comparison. The inset picture shows a close-up of the inversion to help see the restoration effects of the IDMP.

DWL estimates with data collected on different days under slightly different weather conditions. A few remarks were made after inspecting these binned scatter plots. First, an offset is visible in the wind direction. This is because the true heading of the DWL, used as a reference in the wind calculation, must be entered manually based off of measurements using an external compass. The estimations from a cellular phone compass were used, which may have introduced the noticeable offsets each day. Second, the LESO agrees fairly well with the DWL estimations at low horizontal wind speeds ($< \sim 8$ m s^{-1}), whereas a visible underestimation trend from the CopterSonde with respect to the one-to-one line appears past the 8 m s^{-1} wind speed mark. This is likely due to the nonlinear relationship between aerodynamic drag and wind velocity (Equation 4.19) affecting both WVFM and LESO. In addition, the dataset used for calibration had a low content of high wind speed data, which may have contributed to the poor fit-

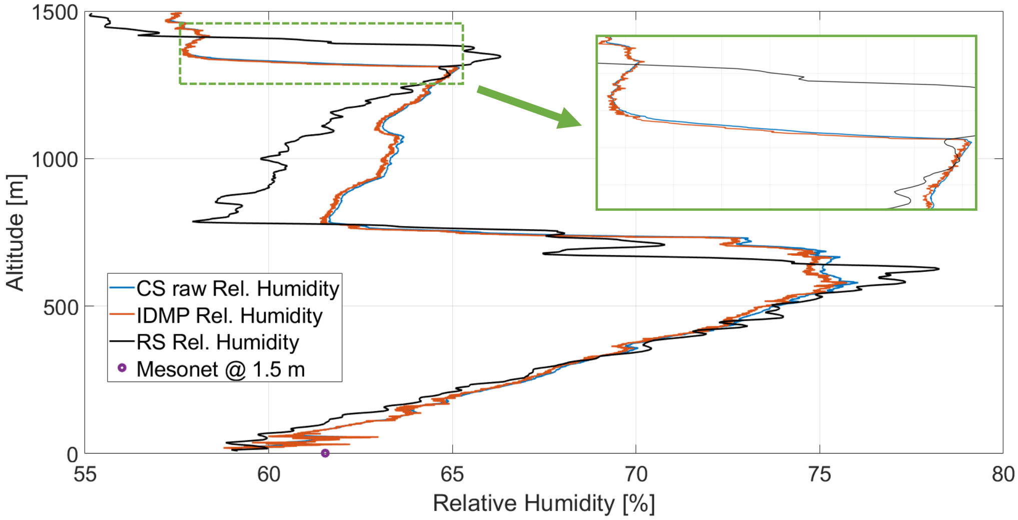

Figure 4.24: Relative humidity profile of the CopterSonde (CS) and radiosonde (RS) up to a height of 1500 m AGL. Their difference visibly increases as altitude increases due to the radiosonde drifting by wind and sampling regions of the PBL far from the launch point. Two small PBL thermal inversions were captured by both systems. The CopterSonde relative humidity data were processed using the IDMP technique for comparison. The inset picture shows a close-up of the inversion to help see the restoration effects of the IDMP.

ting of the modified Rayleigh curve at high wind speed. As a result, it is imperative to establish a more comprehensive calibration method for the LESO and WVFM methods. Moreover, using controlled environments, such as a wind tunnel, would greatly increase the accuracy of the calibration and, consequently, the overall performance of the LESO and WVFM. Lastly, the vertical wind velocity estimates of the LESO are remarkably similar to the DWL estimations throughout the trials. Figure 4.22(a) illustrates a vertical wind profile example where downdrafts, updrafts, and vertically steady air parcels were captured by both systems. While Figure 4.22(b) shows the scatter plot between the CopterSonde and DWL estimations with a notable correlation close to 0.9 for this particular case. Based on the reasoning made above about the modified Rayleigh curve, the high agreement of the vertical wind estimates is due to the low vertical wind speed

Table 4.4: Mean difference (MD), root-mean-squared error (RMSE), standard deviation (SD), and correlation coefficient (R) between CopterSonde-3D (CS3D) and radiosonde thermodynamic and kinematic profiles observed at the same time and initially co-located at the launch point. This includes the different techniques developed for wind estimation and thermodynamic correction of the CS3D.

CS3D technique	Radiosonde			
Wind speed	MD [m s^{-1}]	RMSE [m s^{-1}]	SD [m s^{-1}]	R
WVFM	-0.401	0.908	0.815	0.826
LESO	0.792	1.241	0.955	0.749
Wind direction	MD [deg]	RMSE [deg]	SD [deg]	R
WVFM	3.024	8.146	7.563	0.936
LESO	2.947	8.220	7.673	0.935
Temperature	MD [K]	RMSE [K]	SD [K]	R
CS3D raw	0.351	0.430	0.248	0.995
IDMP	0.341	0.422	0.249	0.995
Relative Humidity	MD [%]	RMSE [%]	SD [%]	R
CS3D raw	0.712	2.548	2.446	0.907
IDMP	0.541	2.519	2.460	0.905

experienced by the CopterSonde. Consequently, the LESO runs within a more linear regime, while the ax^b regression curve, Equation (4.19), suffers less from extrapolation errors.

Moving on to the thermodynamic analysis of the experiment. A single radiosonde was launched almost simultaneously with the CopterSonde on takeoff. Both instruments were visibly ascending almost at the same rate while the radiosonde was drifting with the wind. Figures 4.23 and 4.24 show temperature and humidity profiles, respectively, observed by the CopterSonde and radiosonde. Additionally, the raw CopterSonde data were processed employing the IDMP technique introduced earlier in this chapter. Two small PBL inversions, remainders of the early morning transition, were captured by the thermo-hygrometers onboard the CopterSonde and radiosonde. How-

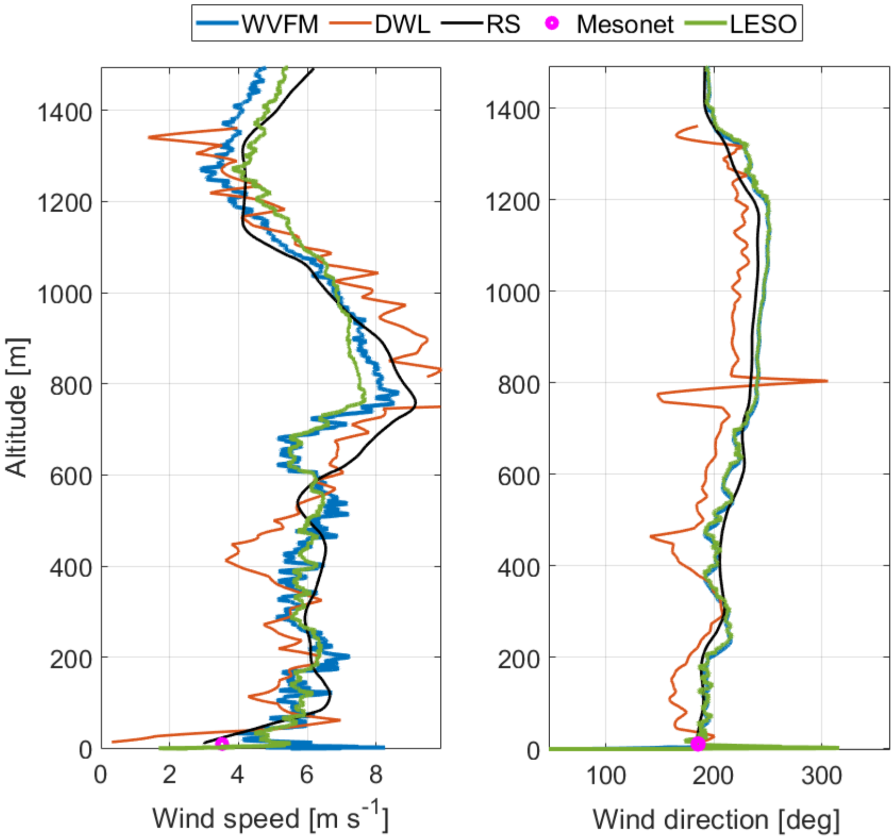

Figure 4.25: Horizontal wind speed (left) and direction (right) profiles of the CopterSonde, DWL, and radiosonde up to a height of 1500 m AGL. The 10 m wind measurement of WOMT at takeoff time was included as a reference. The offset seen on the DWL wind direction is due to the poor measurement of the true heading of the DWL using an external compass.

ever, the temperature and humidity profiles exhibit slightly different patterns, most likely due to the limitations of the radiosonde previously described. In addition, a small offset is observed in the temperature profile between the CopterSonde and radiosonde. This is likely due to the calibration offsets applied to the CopterSonde estimations, as previously described in Section 3.5.2, while the radiosonde measurements had no correction. Despite this, the radiosonde and CopterSonde thermodynamic measurements present a high level of agreement with a correlation coefficient of over 0.9 and RMSE close to sensor specifications (Table 4.4) and desired measurement specifications (Table 3.1). The IDMP shows little visible correction through the sharp temperature and humidity gradients of the profiles as shown in the inset close-up images in Figures 4.23 and 4.24. This is also manifested in the little RMSE and correlation change with respect to the raw CopterSonde measurements presented in Table 4.4. Given that the CopterSonde climb rate is relatively slow (3.8 m s^{-1}) through the gradients compared to the radiosonde climb rate (typically 5 m s^{-1}), this should allow the sensors to capture the dynamics of the PBL inversion better. Therefore, measurement corrections can be disregarded for low flight speeds. Besides this, the IDMP is also “recovering,” or amplifying, the small-scale temperature and humidity variations throughout the profile, which is visible in the inset close-up images. If the recovered variations are real and not a product of IDMP instability, they may be useful in analyzing atmospheric turbulence and mixing. Again, given the limitations of this comparison approach and the lack of unquestionable ground truth, it is virtually impossible to determine which systems are causing bias. Despite this, the results show that the thermodynamic measurements of the CopterSonde are similar to the widely accepted radiosonde instruments when compared to the desired measurement requirements (Table 3.1) and radiosonde specifications (Table 4.3). Overall, this verifies the work done to minimize platform errors for observing thermodynamic fields in the PBL.

The horizontal wind profiles of the radiosonde are more alike to the wind profile of the CopterSonde by the looks of Figure 4.25. A few spikes in the DWL measurements could either be a product of poor SNR, non-homogeneous wind, or both in those regions of the atmosphere. For this particular experiment, neither the WVFM nor LESO wind speed estimations have a correlation coefficient greater than 0.85 and RMSE lower than 0.9 m s^{-1} with respect to radiosonde and DWL estimations (Table 4.4).

4.5 Chapter Summary

This chapter introduced three complementary features for the CopterSonde, the IDMP, WVFM, and LESO. The design and development of these features were mainly driven by the hardware design of the CopterSonde, presented in the previous chapter, and meant to work together as a whole. The WVFM was created with the purpose of maintaining the CopterSonde heading into the wind based on real-time estimates of the tilt vector computed internally by the autopilot. A process to properly tune the WVFM was established where the operating constraints were determined based on results from flow simulations and observations in the field. As a result, the heat emanating from the CopterSonde body was redirected away from the thermo-hygrometers, and thus, greatly minimizing platform-source errors. Subsequently, the IDMP was introduced to lay the foundations for exploring measurement correction techniques for sensors onboard the UAVs. In particular for the CopterSonde hardware since the platform promises unique ways for minimizing thermodynamic measurement errors. Lastly, the 3D wind estimations using the LESO method with a modified Rayleigh equation for aerodynamic drag was demonstrated. Again, the WVFM and the particular hardware design of the CopterSonde allowed for a few assumptions that made the wind estimation process simpler, in addition to making possible the estimation of vertical wind velocities.

Experiments in the field were conducted to compare the CopterSonde measurements with other "co-located" instruments like radiosondes, Doppler wind lidars, and meteorological towers. A statistical analysis was made to determine the overall performance of the CopterSonde measurements as well as the presented techniques with respect to the radiosonde and DWLs.

Regarding the kinematic measurements, the CopterSonde and DWL wind estimations had a strong relationship with a correlation coefficient as high as 0.9 and a fair agreement with RMSE of 0.492 m s^{-1} for vertical wind, and 1.025 m s^{-1} for horizontal wind. The LESO performed better at lower wind speeds below 8 m s^{-1} while trending towards underestimation as the wind speed increases. This is likely produced by non-linearities of the aerodynamic drag and wind speed relation as well as possible extrapolation errors due to the poor wind speed range used for calibration. The results are encouraging but still not within the desired proposed measurement requirements in Table 3.1. When comparing the thermodynamic measurements of the CopterSonde-3D with the radiosonde, temperature profiles exhibit good relationship and agreement as evidenced by their correlation coefficient R=0.995 and RMSE=0.430 K. At the same time, the relative humidity sensor has an R=0.91 and RMSE=2.548 %. Even though both platforms were sampling different columns of air, the results are close to the absolute values shown in Table 3.1.

Although there are several subtleties and inherent limitations from each instrument that are unavoidable in practice, it was the best approach available. Despite these limitations, the temperature and humidity profiles between the CopterSonde-3D and radiosonde appear to be tracking consistently well in the first few hundred meters when the radiosonde is still close enough to the launch point (Figures 4.23 and 4.24). Even the statistical comparison shown in Table 4.4 is evidence that the measured profiles are relatively similar. The relative error is close to the absolute target values from Table 3.1 when considering the radiosonde specifications provided by the manufacturer (Table 4.3). However, a strong conclusion validating the CopterSonde-3D thermodynamic and kinematic results could not be made, given the lack of contrast against unquestionable ground-truth measurements. As future work, access to high-end wind tunnels and environmental chambers may allow for better characterization, calibration, and validation of the presented CopterSonde-3D techniques with a much higher certainty degree. Nonetheless, the thermodynamic analysis made in Section 3.5.3 shows great support that the CopterSonde-3D measurement technique effectively mitigates thermodynamic errors. If these results are assumed to be valid above the surface deeper into the PBL, then the difference in the thermodynamic measurements may be purely due to the spatial separation and sensor calibration. Like this, the WxUAS has the advantage of performing repeatable, targeted, and controlled vertical profiles but at a reduced maximum altitude compared to radiosonde. At this point, it would be up to the users to decide the most convenient platform that may fulfill their objectives, given the presented pros and cons of each instrument.

Chapter 5

CopterSonde Deployments and Community Impact

The CopterSonde system, in its present version, is in compliance with current operating regulations and requirements. Non-scientific operational and safety regulations dictated by the FAA, as well as the NOAA Office of Marine and Aviation Operations (OMAO), were followed in order to conduct FAA-approved and NOAA-related missions using the CopterSonde. During the time frame of this work, the FAA imposed stringent rules regarding operations with UAS that are proposed in Chapter 14 of the Code of Federal Regulation (14 CFR Part 107) [62]. The FAA can also issue a Certificate of Authorization (COA) upon petition, allowing UAS users to go beyond some of the rules in 14 CFR Part 107, such as increasing the flight ceiling and conducting night flights at the requested flight site. To comply with these rules, CASS trained their personnel according to the FAA standards on UAS to obtain valid Part 107 licenses. Additionally, CASS requested COAs for specific regions of scientific interest to allow for flight tests and experimentation. A summary of the applicable regulations regarding UAS operations during the time period of this work is presented in Appendix B.

Flight operations with the CopterSonde require a ground crew of at least three people. The head of operations is the Pilot in Command (PIC), who is in charge of the risk assessment and is responsible for decisions taken during the operation. The PIC also has the duty of preparing and controlling the CopterSonde by means of remote control as needed. The CopterSonde can fly autonomously from takeoff to landing; however, the PIC can assume control at any time, if necessary. The PIC must maintain a visual line of sight with the CopterSonde at all times. Therefore, the second person is the Ground Station Operator (GSO), who is in charge of carefully monitoring the flight data streamed by the CopterSonde through a computer interface. The GSO informs the PIC about any event reported by the CopterSonde system. Lastly, the Visual Observer (VO) completes the ground crew and has the task of scanning the sky for any oncoming air traffic or hazards that may interfere with the flight operation.

Moreover, every field campaign required the involvement of students, staff, and volunteers to help conduct CopterSonde operations. Many of them had no experience working with UAS. Therefore, part of this work was to design and implement a training program for anyone interested in becoming part of the CopterSonde crew. This work produced and provided user manuals, tutorial videos, flight simulator sessions, and field training to the trainees. The high acceptance of the participants and the successful completion of numerous field campaigns using the CopterSonde provides proof of its user-friendliness and adaptability. In addition, attended operations greatly help to identify and address unforeseen challenges. This helps to prepare the CopterSonde system and gradually move toward fully autonomous and unattended operations.

To digitally record and document every flight done using the CopterSonde, CASS acquired fleet-management software from DroneLogBook (DLB) [129]. DLB is fully compatible with CopterSonde's flight logs, extracting necessary information to generate records and statistics for each CopterSonde. Moreover, DLB was configured to send alerts about programmed inspections after a certain number of flying hours and other scheduled maintenance services. This helped to treat every CopterSonde evenly and consistently, which led to fair conclusions about its durability and performance. Although CopterSonde flights started in early 2017, the DLB system was acquired and first used in late 2019. For this reason, the statistics listed below are based on 2-year DLB records from late 2019 to late 2022.

- Total CopterSondes built: 11
- Number of trained participants: 25
- Total flying hours (CopterSonde fleet): 129 hrs and 16 min
- Total number of flights (CopterSonde fleet): 1154
- Greatest total flying hours (single CopterSonde): 35 hrs and 42 min
- Greatest total number of flights (single CopterSonde): 345

Another DLB feature is the thorough documentation of flight checklists during flight operations, which are extremely useful in reducing mission failure due to human errors caused by limited memory and attention. For the sake of brevity, the checklist titles with short descriptions are listed below.

- Pre-Departure: Must be completed 24–48 hrs before departure to the flight site. Essential equipment must be ready.
- Post-Arrival: These are crucial steps for flight site assessment and safe deployment of the equipment immediately after arriving.
- Pre-Flight: It checks the overall health of the CopterSonde system and reminds the crew of their tasks before takeoff.
- In-Flight: It aids in verifying the correct behavior of the CopterSonde soon after takeoff.
- Post-Flight: Goes over the shutdown sequence of the CopterSonde and visual inspection steps after landing.

- Post-Operation: These steps guide the crew in retrieving the flight logs and uploading them to the DLB system after the flight operation is over.

The takeoff of the CopterSonde can generally be performed autonomously and initialized by the PIC under unanimous approval from the crew. The platform immediately proceeds to execute the pre-loaded waypoint mission. The waypoint mission is the desired flight route for the CopterSonde to follow, which was planned and created before the flight by the PIC and GSO. The CopterSonde is capable of performing a variety of flight routes, from simple straight lines to complex spline curves. However, the vertical profile pattern was chosen as the preferred type of flight mission for temperature and humidity profiling, for which the CopterSonde was designed and optimized. The CopterSonde is able to return to the launch point and land autonomously provided that it is flying under good GPS conditions. Good GPS conditions are defined by ArduPilot as having horizontal dilution of precision (HDOP) less than five and more than five satellites visible. Otherwise, the PIC can take control through the remote control and manually land the CopterSonde at any time.

5.1 CopterSonde Products

The CopterSonde concept extends beyond the aircraft itself and also includes data handling and distribution systems for the end user. There are three primary components related to the distribution of sensor data from the CopterSonde. The first component is the sensor package within the flight controller which is responsible for collecting the raw measurement data, logging to a local log file, and transmitting it to the GCS. Sensor data are packed into a custom MAVLink message, as described in Section 3.2.2, and transmitted through the telemetry radio to the GCS using ArduPilot's messaging protocol. The second component is the custom GCS software developed by CASS, which decodes the MAVLink message, retrieves the desired information, plots the data on various graphical interfaces for visual feedback, and forwards the data to an online cloud service [26]. The final component is the data processing systems located within the cloud computing service Microsoft® Azure. The virtual machines analyze the ingested data, store the results in a cloud database, and finally pass the data to a post-processing service bus for interested remote end users or subscribers. For example, the public web application http://wxuas.com is subscribed to such service, and it was created to distribute the CopterSonde's data. The web application then forwards the information directly to connected web clients via web sockets. This enables a live view of the CopterSonde's data for any remote user via the web during flight operations. Another method of data storage is by using the included removable micro SD card mounted on the Pixhawk autopilot board. This method is preferred over streamed data for post-processing because it stores data with higher temporal resolution. Besides all the products presented in this work, some other useful products generated based on data acquired using the CopterSonde are the Skew–T log-p figures and time-height temperature contours. Examples of these are shown in Figure 5.1 and 5.2, respectively. Post-processing and visualization of CopterSonde data were performed in Python using the open-source packages NumPy [130], Matplotlib [131], MetPy [132], and SciPy [133]. These two types of visualizations allow atmospheric scientists to understand small-scale PBL processes in frameworks they are already familiar with, like radiosondes and ground-based remote sensors.

5.2 Work Accomplished and Recognition

To date, multiple iterations of CopterSonde have been deployed in several measurement campaigns that have encompassed a wide range of meteorological conditions. Each of

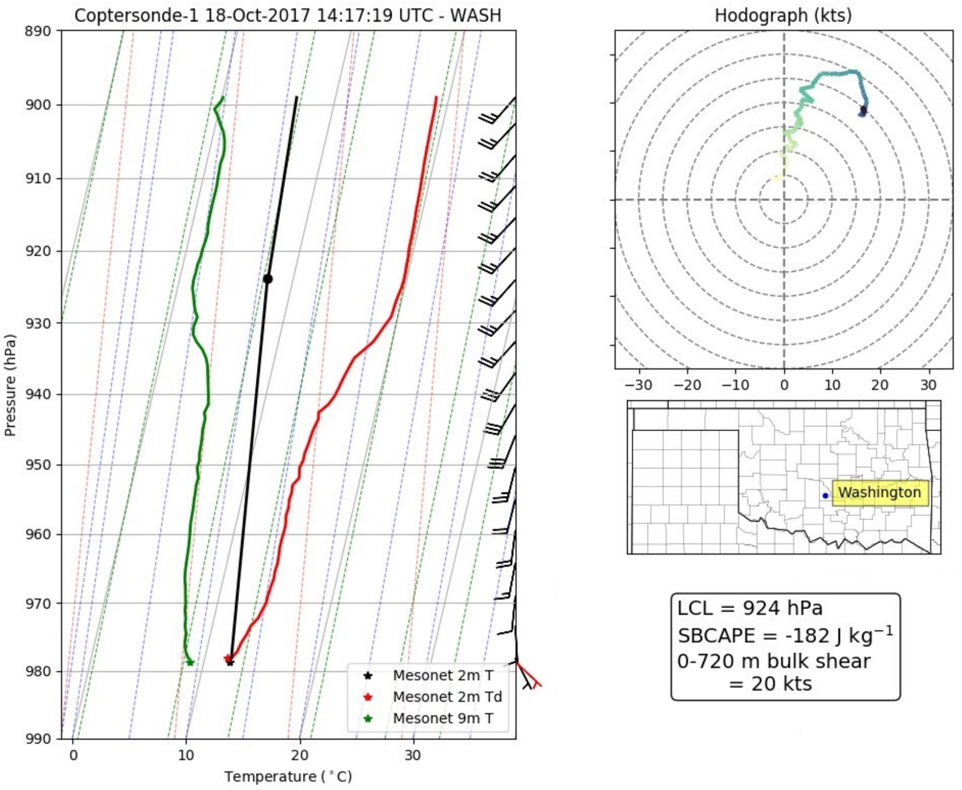

Figure 5.1: Example skew-T log-p plot of temperature (red line) and dewpoint (green line) generated from a single CopterSonde flight. The surface-based parcel process curve is also included (black line). A hodograph in the upper right corner shows the wind speed and direction over height. Also included are some basic thermodynamic air parcel properties and a map of where the profile was measured. The map was generated using the open-source Basemap package, which references the Generic Mapping Tools dataset for state borders [134].

the field campaigns led to new design ideas that shaped and streamlined the CopterSonde until the current version. The CopterSonde-1 was first deployed in the Environmental Profiling and Initiation of Convection (EPIC) field project in May 2017. EPIC's objective was to evaluate the potential of severe weather formation using data from several meteorological instruments, including WxUAS [21]. The EPIC field campaign revealed a few flaws of the CopterSonde-1 that defined the roadmap for the next CopterSonde revisions, as discussed in chapter 3. From this point forward, the CopterSonde

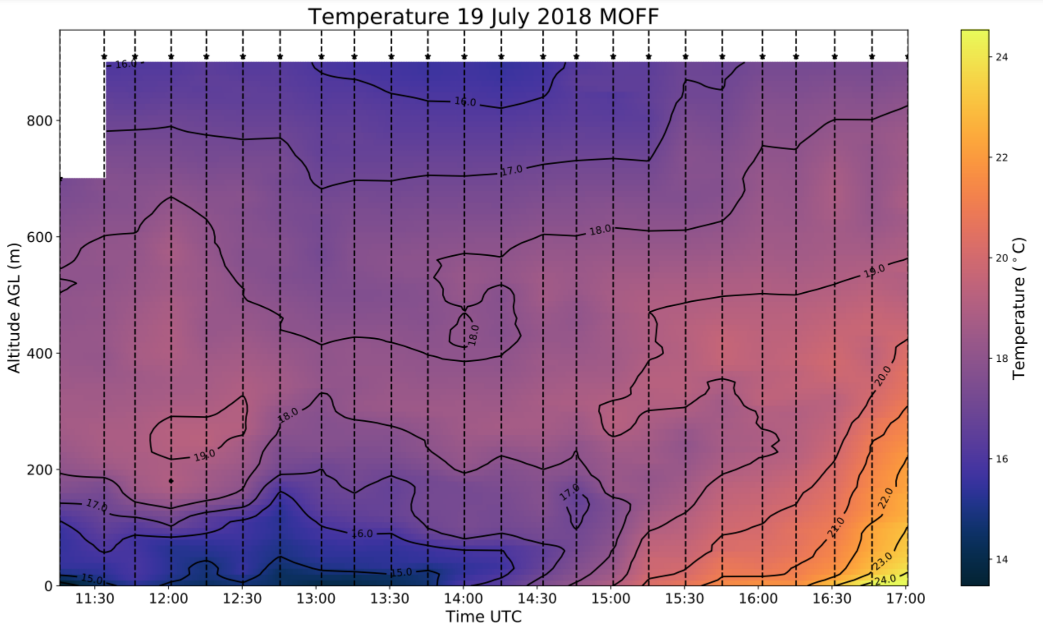

Figure 5.2: Example plot of the temperature evolution over time with contour lines up to a height of 914 m. Each CopterSonde profile was separated by about 15 min and denoted by vertical dashed lines. The contours and color fill were produced by interpolating each observation level in time, resulting in a rectangular time-height cross-section.

development continued under the support in part of the National Science Foundation (NSF) Grant No. 1539070, a project known as Collaboration Leading Operational UAS Development for Meteorology and Atmospheric Physics (CLOUD-MAP) [23], and internal funding from the OU. The observations from the field campaigns detailed below are still being analyzed, but the empirical experience and findings showed evidence of the capabilities of CopterSonde in sampling the PBL. In particular, achievements made with the CopterSonde operating under a wide range of atmospheric conditions are discussed, which led to substantial improvements in the WxUAS design.

5.2.1 Innovative Strategies for Observations in the Arctic Atmospheric Boundary Layer (ISOBAR)

The first extensive field testing of the CopterSonde in approximately its current configuration occurred during a 4-week-long field campaign in Hailuoto, Finland, in February 2018. This field campaign, known as Innovative Strategies for Observations in the Arctic Atmospheric Boundary Layer (ISOBAR), aimed to study the stable Arctic atmospheric boundary layer over sea ice [22, 135]. The University of Oklahoma CASS worked in close collaboration with the Finnish Meteorological Institute (FMI), the Geophysical Institute of the University of Bergen (UiB), the University of Tübingen, and the University of Applied Science Ostwestfalen-Lippe (OWL) to obtain continuous boundary layer profiles over the course of the field campaign. This allowed for the observation of the diurnal development of the stable boundary layer, which would have been difficult with only one crew. The CopterSonde used during ISOBAR was the CopterSonde-2, shown in Figure 5.3, which was the immediate successor of the CopterSonde-1. The CopterSonde-2 was the first design attempt toward the final CopterSonde-3D. This platform included an underdeveloped WVFM and weather sensor integration into the autopilot. The scoop intake was large compared to the CopterSonde-3D, completely exposing the sensors to the environment and, thus, solar radiation. However, the CopterSonde-2 was still able to complete the required scientific goals of the ISOBAR campaign and withstand the harsh arctic environment. In addition to accomplishing the scientific aims of measuring the stable boundary layer, the CopterSonde accomplished a number of firsts, including flying at night and outside the visual line of sight and establishing a new height record by ascending to 1800 m (5900 ft) AGL. Moreover, in one of the endurance flight tests, the CopterSonde-2 stayed aloft for 18.5 min, almost depleting the battery with less than 10% of its energy capacity left.

Figure 5.3: Left image: OU-CASS team in the island of Hailuoto, Finland, showcasing the UAS equipment used for the ISOBAR field campaign in February 2018. Right image: Front view of the CopterSonde 2 deployed outside in the freezing environment. This platform was the immediate successor of the CopterSonde-1 and the first design attempt toward the CopterSonde-3D concept. The custom integration of the WVFM and weather sensors into the autopilot were first introduced in this version.

Additionally, surface temperatures dropped to around -20 ° C during the experiments, and even a thin layer of ice was detected on the leading edge of the propellers after flying through the mist. However, the accumulated ice was not enough to produce notable effects on the CopterSonde performance. This does not mean that the CopterSonde is able to fly under icing conditions since a tolerable level of accumulated ice could not be determined, besides not having a method to quickly detect ice formation while flying.

5.2.2 Lower Atmospheric Process Studies at Elevation—a Remotely Piloted Aircraft Team Experiment (LAPSE-RATE)

After ISOBAR, the CopterSonde-2 has undergone several hardware and software modifications to account for issues encountered in previous experiences and improve the system overall. This led to the production of the CopterSonde-2.5 revision illustrated in Figure 5.4. The CopterSonde shell was substantially redesigned and streamlined in this

Figure 5.4: Left image: OU-CASS member flying the CopterSonde-2.5 in the San Luis Valley, Colorado, and capturing atmospheric observations for the LAPSE-RATE field campaign in July 2018. The platform successfully flew in an altitude range of 2300–3210 m AMSL for 5 consecutive days. Right image: Front-side view of the CopterSonde-2.5 developed after ISOBAR and first deployed during LAPSE-RATE. The CopterSonde shell was substantially redesigned and streamlined in this version while adding modularity to the payload and other components.

version while adding modularity to the payload and other components. Besides this, the scoop intake design was changed to better hide the weather sensors from sunlight. The propulsion system was also upgraded for flight stability and efficiency improvements.

With these enhancements, the CopterSonde-2.5 was deployed to the San Luis Valley in south-central Colorado in July 2018 for the Lower Atmospheric Process Studies at Elevation—a Remotely Piloted Aircraft Team Experiment (LAPSE-RATE). LAPSE-RATE was held in connection with the conference of the International Society for Atmospheric Research Using Remotely Piloted Aircraft (ISARRA) in Boulder, Colorado. A total of 13 universities participated in LAPSE-RATE over the six-day field campaign (14-19 July 2018). The scientific goals were roughly defined as examining environmental variables before convective initiation, analyzing drainage flows emanating from nearby mountains, and investigating the PBL during the morning transition phase. Another goal was to compare measurements gathered from multiple platforms flown by different academics and industrial partners [20]. In particular, thorough intercomparisons of the CopterSonde-2.5 data against data from meteorological towers, radiosondes, and Doppler wind lidar were discussed in [110]. Moreover, a study to assimilate data from some of the participating UASs into a weather research and forecasting model using an ensemble Kalman filter was conducted by the National Center for Atmospheric Research (NCAR) in Boulder, Colorado. Their findings showed how observations gathered with a fleet of WxUAS enhance high-resolution and short-term predictions in a limited domain with complex terrain [30]. The data collected using the CopterSonde system are available in the online data archive Zenodo [136] as well as from other platforms for reference and comparison [137, 138].

A total of 180 flights using the CopterSonde were completed over a span of 5 days at two different sites in the northern region of the San Luis valley. A total of two days of operations focused on convection initiation studies, one day dedicated to PBL diurnal transition studies, one day centered on internal comparison flights, and the last day of operations focused on cold air drainage flows [139]. The terrain elevation at the flight sites was approximately 2300 m above mean sea level (AMSL), which is 6.5 times higher than where the CopterSonde was originally built and tuned. In addition, flight permissions allowed the CopterSonde to sample the atmosphere up to 910 m AGL (3000 ft). Therefore, the CopterSonde effectively reached a maximum altitude of 3210 m AMSL without any noticeable decrease in flight performance.

5.2.3 Flux Capacitor

A few weeks after the culmination of the LAPSE-RATE experiments, the OU-organized Flux Capacitor field campaign took place at KAEFS on 5 October, 2018. CopterSonde and CLAMPS DWL data were collected during this in-house campaign to test and evaluate the CopterSonde's performance across a complete diurnal cycle. Flight permissions allowed the OU team to operate the WxUAS up to 1524 m AGL (5000 ft)

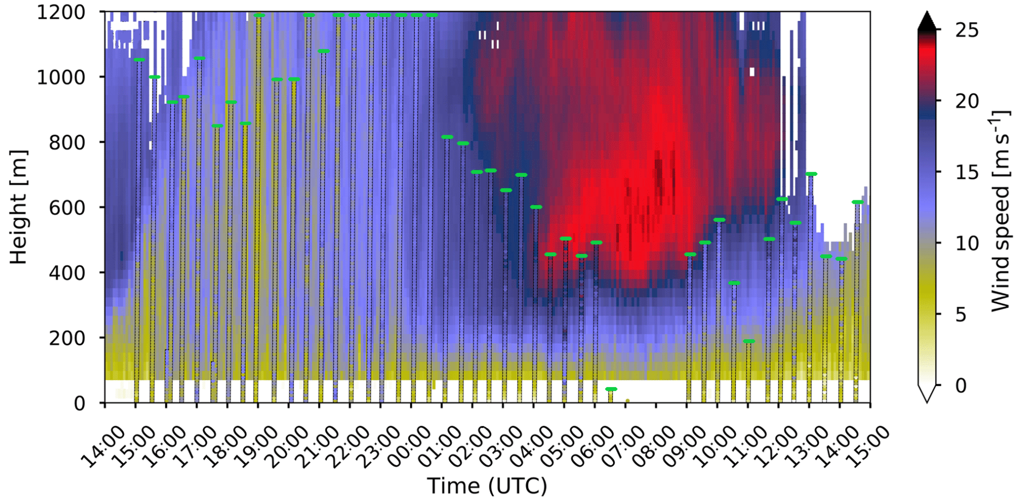

Figure 5.5: Time-height profiles of wind speed collected using a CopterSonde-2.5 UAS and CLAMPS Doppler wind lidar during an uninterrupted 24 hrs operation at KAEFS on 5 October, 2018. The colored background corresponds to wind data from CLAMPS DWL, whereas the vertical lines represent CopterSonde profiles, and green dots denote the maximum altitude reached. It can be seen that the maximum height of the CopterSonde decreased as the low-level jet stream intensified through the night. A post-analysis revealed that the CopterSonde withstood a maximum wind speed of 22.5 m s^{-1}. The image was taken from [110].

during the day and 1220 m (4000 ft) AGL at night. However, the OU team could no longer keep visual contact on the CopterSonde past approximately 1200 m and thus was forced to descend to comply with the FAA rules. Flights were done with a cadence of 30 min for the 24 hrs duration of the experiment. Besides recording the thermodynamic evolution of the atmosphere during this period, a remarkable event was captured when a low-level jet (LLJ) developed overnight. According to CLAMPS measurements, the LLJ wind speeds were peaking close to 25 m s^{-1} at around 500 m AGL.

Due to safety reasons, the CopterSonde was commanded to descend if the pitch angle was nearing 30 deg, caused by high winds, which was equal to 22 m s^{-1} when translated to wind speed using Equation (4.8). Hence, it was considered that the CopterSonde platform reached and recorded its maximum wind speed tolerance during Flux

Capacitor for the first time. This extreme case helped to evaluate and establish flight limits for the CopterSonde system. The correlation between the CopterSonde and DWL wind measurements is noticeable in Figure 5.5, a series of time-height wind profiles collected using a CopterSonde-2.5 UAS. The colored background corresponds to wind data from CLAMPS DWL, whereas the vertical lines represent CopterSonde profiles, and green dots denote the maximum altitude reached. The maximum height reached by the WxUAS decreased as the LLJ lowered and intensified overnight. A comprehensive statistical analysis of the thermodynamic and kinematic measurements was made in [110]. Additionally, a study to determine data availability and impacts on WxUAS operations based on platform limitations due to wind loads over the year was done in [140]. Such information was useful afterward when planning the concept of operations for CopterSonde deployments.

5.2.4 Propagation, Evolution, and Rotation in Linear Storms (PERiLS)

The Propagation, Evolution, and Rotation in Linear Storms (PERiLS) project was one of the most significant severe storm field campaigns conducted by the meteorological community supported by NOAA-NSSL and the NSF [141]. The first part of the project took place in the Southeast United States in the late winter to early spring months of 2022, and the second part is set to continue in 2023. Several instruments from NOAA and multiple research institutes and universities were deployed to capture the dynamics of quasi-linear convective systems (QLCSs). The PERiLS project aims to characterize near-storm environments and storm processes capable of producing tornadoes.

To become part of the PERiLS operations, the CopterSonde successfully underwent an airworthiness certification process to comply with NOAA's UAS guidelines

Figure 5.6: Picture of the CopterSonde-3D and the PIC in action nearby an oncoming squall line of thunderstorms taken during PERiLS 2022 field campaign. Three CopterSonde-3Ds were deployed during PERiLS, and each was strategically located at a different site in the southern region of the United States. The flight ceiling approved by the FAA and NOAA-OMAO was 1524 m (5000 ft). However, the maximum altitude reached by the CopterSonde-3D was just below 1000 m due to extremely high winds.

and policies. Through this work, safety features, concept of operations, and risk management procedures were described and shown to NOAA evaluators following instructions found in policies and a handbook issued by the Aircraft Operations Center of NOAA-OMAO [142, 143]. As of November 2021, the CopterSonde-3D was officially recognized by NOAA-OMAO as an airworthy UAS allowed to deploy in NOAA-related weather operations (see Appendix C).

A total of three CopterSonde-3Ds were deployed and operated simultaneously in March and April 2022 at three different sites (Yazoo City, Mississippi; Schlater, Mississippi; and Lake Village, Arkansas). Figure 5.6 illustrates the CopterSonde-3D and PIC in action nearby a storm formation, and Table 5.1 shows a summary of the CopterSonde

Table 5.1: CopterSonde operation summary for PERiLS conducted in March and April 2022. A total of three CopterSondes were deployed at three different sites simultaneously (Yazoo City, Mississippi; Schlater, Mississippi; and Lake Village, Arkansas).

Variable	All sites	Yazoo City	Schlater	Lake Village
Max. altitude [m]	996	848	996	784
Avg. altitude [m]	424.37	510.79	489.54	286.48
Total flight count	112	39	32	27
Crash/Collisions	0	0	0	0

operations during PERiLS. The flight ceiling approved by the FAA and NOAA-OMAO was 1524 m (5000 ft). However, the maximum altitude reached by the CopterSonde-3D was just below 1000 m due to extremely high winds. The persistent high winds in the pre-storm environment made the platform reach its limits on almost every flight, automatically triggering failsafe mechanisms to safely return the UAS to the launch point. Besides this, a few flights were completed under light rain conditions without electrical issues or failures. Due to the recent culmination of PERiLS 2022, data and observations are still being processed, and there are no related publications involving the use of CopterSonde data yet.

Nonetheless, NOAA proposed a systematic project metric system that supports the evaluation of the maturity of R&D projects from research to operation, application, commercial product or service, or other use and allows the consistent comparison of maturity between different projects [144]. After the successful completion of PERiLS 2022, it is estimated that the CopterSonde-3D UAS falls in the RL 6 category. The RL 6, by definition, is the successful demonstration of a prototype system, subsystem, process, product, service, or tool in a relevant or test environment (potential demonstrated).

5.2.5 Tracking Aerosol Convection Interactions Experiment (TRACER)

The UAS component of the Tracking Aerosol Convection Interactions Experiment (TRACER) field campaign aims to improve the understanding of physical processes governing the convective cloud lifecycle. Mainly, the project focused on coastal weather conditions where air-mass circulation produced by sea breeze is found, and that numerical weather models struggle to represent accurately [145]. Two brand new CopterSonde-3Ds were deployed south of the Houston metro area to collect frequent vertical profiles of thermodynamic and kinematic variables impacted by the Gulf of Mexico weather on a daily basis. Field observations were taken from June through September 2022, which resulted in the most extensive operation period undergone by the CopterSondes to date.

Although no published studies support the scientific relevance of the CopterSonde for TRACER yet, conclusions about the CopterSonde's endurance were made based on the flight records. After eight weeks of operations, both CopterSondes completed a combined total of 604 vertical profiles, equivalent to approximately 67 flying hours. To keep the mechanical wear even, each CopterSonde was flown on alternate days splitting the total flying hours into $\sim$33 hrs each. Quick visual inspections of the fragile parts were conducted every four flying hours, whereas complete inspections of the airframe and electronics were carried out every 8–10 flying hours. Thin layers of rust were detected on steel screws, which was expected given that flights took place under coastal weather conditions. However, flights were not compromised at any time. Oxidation was merely superficial and was easily cleared. Besides this, thin layers of dirt were found over the weather sensors inside the scoop, evidencing the high concentration of particles in the air.

Moreover, one CopterSonde reported erroneous relative humidity measurements from one of the sensors after passing 30 flying hours. It was believed that the air particles gradually degraded the capacitive film on the sensor until the reading offset became noticeable. Besides the above-mentioned minor problems, the CopterSonde-3D airframe, autopilot, propulsion system, and other vital components relevant to flight were found to be healthy and fully functional.

5.3 Chapter Summary

To conduct deployments and flight operations, the CopterSonde must first comply with policies issued by regulatory agencies, including the FAA, NOAA-OMAO, and OU. The proposed rules are primarily concerned with the safety of flights, crew risk management, and air traffic deconfliction. Therefore, the CopterSonde was modified and programmed to meet these requirements. Additionally, training programs were created to educate personnel on UAS operations and instruct them to strictly follow the provided CopterSonde checklists to abide by the rules. The CopterSonde crew is conformed of three human members: PIC, GSO, and VO. Each one has unique tasks during the operations, which complement each other with proper team communication.

Since the CopterSonde is continuously transmitting data to the ground station, data distribution software and cloud storage were implemented to allow for remote access to end users in almost real-time. Besides this, simple Python scripts were made to quickly process raw data and produce products like skew-T log-p plots, time-height evolution plots, hodographs, etc. This allows atmospheric scientists to understand PBL processes in frameworks they are already familiar with, like radiosondes and other ground-based remote instruments.

Multiple iterations of CopterSonde have been deployed in several measurement campaigns that have encompassed a wide range of meteorological conditions. Each deployment presented its own set of challenges that tested the capabilities of the platform. Remarkable achievements, improvements, and flaws of the CopterSonde during different field projects were discussed. The result of each field campaign led to new design ideas that shaped and streamlined the CopterSonde until its current version. The CopterSonde also achieved important recognition from NOAA-OMAO that allowed it to operate in NOAA-related missions. After successfully completing PERiLS 2022, it was estimated that the CopterSonde falls in the RL 6 category based on NOAA's R&D maturity level standard.

To date, the CopterSonde-3D has accumulated numerous historical flight records under different weather conditions. This is evidence that the proposed platform is a durable weather instrument that can perform targeted weather sampling in a reliable way. Here, the word reliable refers to the capacity of the UAS to execute its mission safely. The CopterSonde-3D was programmed to always stay within its operating limits and not to compromise its structural integrity based on the parameters obtained in Section 3.6. Since the acquisition of the DroneLogBook fleet-management service in 2019, 11 different CopterSondes were used for a combined flight time of 129 hrs and 16 min and 1154 successful flights. The single most used CopterSonde did almost 36 flying hours without failures or mechanical degradation, hinting the lifespan of the platform is high enough to satisfy measurement needs from demanding field campaigns.

Chapter 6

Epilogue

6.1 Discussion and Conclusions

The main focus throughout this work was achieving targeted and reliable *in situ* UAS-based thermodynamic and kinematic measurements of the atmosphere as a means to solve the observational gap present in the PBL. The motivation and problem statement were formulated in Chapter 1, addressing the clear need to improve the understanding of the Earth's PBL. Nonetheless, commonly used conventional atmospheric instruments, such as radiosondes, Doppler lidars, satellites, and meteorological towers, are insufficient in providing adequate spatial and temporal resolution required to capture fast atmospheric processes due to the high complexity and variability of the structures in the PBL (see Section 1.2). With the increasing popularity of weather measurements collected using UAS technologies, a solution was proposed focusing particularly on the development of a UAS that maximizes the mitigation of platform errors for thermodynamic measurements and the implementation of wind field estimation using modern modeling techniques. All of these while exposing the WxUAS to different weather scenarios and refining the concept of operations. Besides this, an attempt to meet the desired meteorological measurement requirements (Table 3.1) was also pursued. However, strong concluding remarks on the latter could not be completely achieved, given the lack of measurement comparison against unquestionable ground-truth instruments. Despite this, the measurement intercomparison presented in Section 4.4 helped to visualize, in a qualitative way, where WxUAS may be standing with respect to conventional instruments. From these experiments, it was demonstrated the capacity of the CopterSonde-3D to fill in observational gaps where limitations from the conventional instruments interfered with the measurements.

Chapter 2 introduced basic concepts and definitions of the main elements of the instrumentation system presented in this work: UAS, PBL, and thermodynamic sensors. First, the UAS serves as the carrier to transport the payload to desired locations in space. There are several types of UAS with different flight characteristics, but the multicopter-type UAS was chosen for its simplicity and VTOL capability. Building blocks of the multicopter UAS were described and used for the design of the proposed WxUAS. Second, the PBL is the desired environmental domain for UAS flights and atmospheric measurements. Therefore, understanding the properties and dynamics of the PBL is paramount for the correct instrumentation design and validation. Since the multicopter UAS heavily modifies the surrounding air, these concepts helped to discern real atmospheric processes from platform-induced effects. Lastly, the thermo-hygrometers or weather sensors were provided without prior engineering selection process. However, their compact size and light weight made them suitable payloads for a small multicopter UAS. Mathematical models of iMet-XF bead thermistor and HYT-271 capacitive humidity sensors were introduced, which describe the flux dynamics inside the sensing element. These models were used for the measurement restoration technique presented in Chapter 4.

Design constraints on the proposed WxUAS were mainly imposed by the operating concept required for the 3D Mesonet project [26]. Besides this, the CopterSonde-3D is also compliant with policies and guidelines proposed by the FAA, NOAA-OMAO, and OU regarding flight safety and operational competence. The development of the CopterSonde platform's design and proof of concept was fully detailed in Chapter 3. It outlined the technical obstacles experienced from the idea of the UAV-based atmospheric measurements system to the present revision, as well as the choices made to continue enhancing the WxUAV system's critical components. The balance between autopilot software integration, airframe selection, and propulsion design had to be understood to construct a platform capable of achieving atmospheric measurement needs while adhering to prescribed safety norms and flight functionalities. After several iterations of the design, it is believed that the CopterSonde-3D achieved a highly holistic design. The localized weather sensor placement on the UAV, the proposed WVFM function, and the custom autopilot code to handle weather data are all intimately interconnected to the extent that the platform cannot be considered for general-purpose use anymore but solely for weather research and applications.

The proposed payload, or weather sensor compartment, was designed to be modular and, at the same time, blend in with the CopterSonde-3D's body for increased aerodynamic efficiency (see Section 3.5). Flow simulation studies of the CopterSonde-3D's CAD model showed a significant reduction of the heat footprint and turbulent wake behind the platform compared to a standard UAS design (i.e. CopterSonde-1). The simulation results were supported by real observations in the field using a meteorological tower for reference. As a result, a range of angles in which the thermodynamic measurements are unaffected by heat advection was determined and presented as evidence that the concept works as intended. Overall, it was shown that platform-induced errors close to the weather sensors were more manageable with the CopterSonde-3D design when assisted by the WVFM function. Based on results from Section 3.5.3, it is apparent that the localized sensor placement of the CopterSonde-3D combined with the WVFM is more successful than the distributed sensor layout of the CopterSonde-1 at mitigating effects from heat advection. However, a drawback in the design was identified when the ascent and descent thermodynamic profiles were found to differ significantly from each other. This is due to the UAV descending through its prop wash, creating temporary stagnant air around the platform. For flight stability reasons, it was opted not to modify the CopterSonde design further to account for the prop wash effects. Instead, priority was given to the optimization of weather sampling in the ascent leg over the descent leg. Design specifications of the CopterSonde-3D that define the flight envelope were presented in Section 3.6. Flight records from extreme events have been analyzed to establish safe operating restrictions. These parameters were used to create decision-making algorithms able to automatically trigger failsafe mechanisms. Safety was kept as a top priority, and generous energy reserves were made available to the CopterSonde-3D in case of unexpected events and still able to complete its mission.

Weather-specific algorithms for the CopterSonde-3D were introduced in Chapter 4. The IDMP was developed to demonstrate the capabilities of using thermodynamic measurement correction techniques suitable for weather sensors onboard the multicopter UAVs [2]. This lays the foundations for exploring methods to mitigate slow sensor dynamics. In particular for the CopterSonde hardware since the platform promises unique ways for minimizing thermodynamic measurement errors. Subsequently, the WVFM function was created with the intention of maintaining the CopterSonde-3D's heading into the oncoming wind based on real-time estimations of the tilt vector done internally by the autopilot [1]. This way, the sensor package stays downwind of the main body of the UAV, and, as a result, undisturbed air flows across the sensors inside the scoop. Given that linear and time-invariant causal filters were used in the WVFM method, the output is slightly delayed but within the desired angle range with respect to the wind vector, determined in Section 3.5.3. Lastly, the 3D wind estimation using an offline LESO technique with a modified Rayleigh equation was presented. The WVFM and the unique hardware design of the CopterSonde-3D made it possible to simplify the wind estimation calculations, besides enabling the estimation of vertical wind velocities.

In terms of kinematic measurements, the CopterSonde and DWL wind estimates had a good relationship with a correlation coefficient of 0.9 and a reasonable agreement with RMSE of 0.492 m s^{-1} for vertical wind and 1.025 m s^{-1} for horizontal wind. The LESO performed well at lower wind speeds below 8 m s^{-1}, but underperformed as wind speed increased. This is most likely caused by non-linearities in the aerodynamic drag and wind speed relationship, as well as extrapolation errors caused by the limited wind speed range employed for calibration. The findings are positive, although they fall short of the specified measurement standards in Table 3.1. Temperature profiles indicate excellent association and agreement when the CopterSonde-3D thermodynamic data are compared to the radiosonde, as evidenced by their correlation coefficient R=0.995 and RMSE=0.430 K. Simultaneously, the relative humidity sensor has an R=0.91 and an RMSE=2.548 %. Despite the fact that both platforms sampled distinct columns of air, the findings are quite similar to the absolute values presented in Table 3.1.

Although there are several subtleties and inherent limitations from each instrument that are unavoidable in practice, it was the best approach available. Despite these limitations, the temperature and humidity profiles between the CopterSonde-3D and radiosonde appear to be tracking consistently well in the first few hundred meters when the radiosonde is still close enough to the launch point (Figures 4.23 and 4.24). Even the statistical comparison shown in Table 4.4 is evidence that the measured profiles are relatively similar. The relative error is close to the absolute target values from Table 3.1 when considering the radiosonde specifications provided by the manufacturer (Table 4.3). However, a strong conclusion validating the CopterSonde-3D thermodynamic and kinematic results could not be made, given the lack of contrast against unquestionable ground-truth measurements. As future work, access to high-end wind tunnels and environmental chambers may allow for better characterization, calibration, and validation of the presented CopterSonde-3D techniques with a much higher certainty degree. Nonetheless, the thermodynamic analysis made in Section 3.5.3 shows great support that the CopterSonde-3D measurement technique effectively mitigates thermodynamic errors. If these results are assumed to be valid above the surface deeper into the PBL, then the difference in the thermodynamic measurements may be purely due to the spatial separation and sensor calibration. Like this, the WxUAS has the advantage of performing repeatable, targeted, and controlled vertical profiles but at a reduced maximum altitude compared to radiosonde. At this point, it would be up to the users to decide the most convenient platform that may fulfill their objectives, given the presented pros and cons of each instrument. The thermodynamic and kinematic statistical analysis, flow simulations, and CopterSonde flight performance results shown in this work, in addition to other similar studies done using the CopterSonde [1, 2, 20, 42, 110], are used as proof to show that the proposed platform works as intended meeting the proposed objectives listed in Chapter 1.

The CopterSonde has been deployed in several challenging field campaigns. Each of these field experiences tested the capabilities of the platform under different atmospheric conditions (see Chapter 5). Besides meeting the scientific goals of each project, design limits and flaws were identified that led to new design ideas to overcome the difficulties. This way, the CopterSonde was shaped and streamlined until its current version, driven by experience. To date, the CopterSonde has accumulated enough flight records that it can be considered a durable weather instrument able to perform targeted weather sampling in a reliable way. Here, the word reliable refers to the capacity of the UAS to execute its mission safely. The CopterSonde-3D was programmed to always stay within its operating limits and not to compromise its structural integrity based on the parameters obtained in Section 3.6. Since the acquisition of the DLB fleet management service in 2019, 11 different CopterSondes were used for a combined flight time of 129 hrs and 16 min and 1154 successful vertical profiles. The single most used CopterSonde did almost 36 flying hours without failures or mechanical degradation, hinting that the lifespan of the platform is sufficient to satisfy measurement needs from demanding field campaigns. Moreover, the CopterSonde also achieved important recognition from NOAA-OMAO that allowed it to operate in NOAA-related missions (see Appendix C). It was estimated that the CopterSonde falls in the RL 6 category, or successful demonstration of the prototype, based on NOAA's R&D maturity level standard. This is one stage behind RL 7: Prototype functionality, which would require the CopterSonde to be fully integrated into the weather modeling and forecast system. Advances toward this next step are underway, data distribution software and cloud storage were implemented to allow end users to remote access and process in almost real-time (see http://wxuas.com). Besides this, simple Python scripts were made to quickly process raw data and produce products like skew-T log-p plots, time-height evolution plots, hodographs, etc. This allows atmospheric scientists to understand PBL processes in frameworks they are already familiar with, like radiosondes and other ground-based remote instruments.

Altogether, it is believed that the proposed CopterSonde-3D concept is a platform that has the potential to be a unique weather instrument in meteorology research. This work showed engineering advances using emerging UAS technology that may define the path toward more holistic and integrated WxUAS for accurate and reliable atmospheric measurements. This new technology is not seen as a potential replacement for similar existing atmospheric instruments in the near future but more as a complement to cover current measurement limitations and gaps. In the long term, WxUAS may be able to replace its counterpart radiosonde once its full potential is demonstrated. As it was shown in Section 4.4, the WxUAS was able to fill in the missing kinematic observations of the DWL as well as perform a more targeted mission compared to the radiosonde. Given that WxUAS are reusable systems, this could enable sampling the PBL more frequently in a more cost-effective way compared to radiosondes which are usually single-use disposable instruments. As proposed in the 3D Mesonet project, the CopterSonde WxUAS can be deployed at Mesonet sites and act as an extension of the meteorological towers [26]. Effectively augmenting the sampling domain to a volume above the surface and filling in the observational gap [29].

6.2 Future Work

Admittedly, the presented work has only scratched the surface of what UAS is capable of contributing to the atmospheric research field. Since the CopterSonde is an experimental platform going through the early stages of development, there is plenty of room for improvements and future directions. The following discussion will be separated into what may be improved in each chapter of this dissertation, considering the information collected during this study.

A formal design guideline and hardware requirements for multicopter WxUAS were presented in Chapter 3. From a conceptual idea backed with simulation studies to the evaluation of measurement errors in the field. However, the flow simulation studies did not cover the effects of solar radiation, while it was assumed that the scoop design was enough to protect the sensors. Given the little time invested in studying solar radiation's effects, a future direction is to evaluate other scoop design candidates aimed at mitigating these errors while still producing adequate aspiration across the sensors. Material selection of the shell is another topic that was not thoroughly investigated. This study was limited to the use of 3D printers with just one type of PLA plastic. Therefore, it is necessary to thoroughly study the CopterSonde design using lighter materials with lower heat transfer coefficients to help to minimize heat sources. The prop wash was found to be a large inconvenience to the point that the descent-leg measurements were discarded, the amount of collected data can be easily doubled if this issue is properly addressed. A way to solve it is by extending the scoop intake outside the turbulent air wrapping around the CopterSonde, but it must be done in a way that flight stability is not compromised. In general, there is a need for deeper flow simulation analyses and in-field observation to tackle the presented issues. Although in-field observations are important for measurement validation, they cannot always be fully trusted because of several uncontrollable and unpredictable factors in the environment. Therefore, it is strongly suggested to perform studies in controlled environments, such as wind tunnels and environmental chambers, to produce accurate physical interpretations and results. The airflow around UAS exhibits a very complex behavior [146]. Therefore, airflow studies around the UAV are extremely important to reduce the degree of uncertainty as much as possible.

Chapter 4 introduced techniques that exploited the CopterSonde-3D design to improve thermodynamic measurements and estimate wind without relying on external wind sensors. The IDMP was an excellent method for restoring thermodynamic measurement signals according to simple simulations backed with acceptable results from field observations. However, the IDMP is currently not in a position to be fully integrated into the CopterSonde system. The engineering selection process for thermodynamic sensors was not conducted for this study, and therefore, it is strongly suggested to investigate other alternatives. Subsequently, the selected sensors must be thoroughly characterized, similar to the method presented in Section 4.1.1. The problem with the presented characterization method is that it did not cover a wide range of temperature and humidity conditions. This limitation restricted this study to just a particular case, and thus, a more comprehensive characterization is required for the IDMP to become fully operational. The WVFM was considered an innovative solution to orient the CopterSonde-3D in a convenient way that improves weather sampling. Not many problems were identified with this method other than the delay in the wind estimation. However, the delay is an intrinsic characteristic of causal filters, and hence, finding solutions may not be worth pursuing. Lastly, a 3D wind estimation method using the LESO technique was demonstrated to be suitable for the CopterSonde-3D. This method uses a complex UAV model tailored to the CopterSonde-3D and simplified thanks to the introduction of the WVFM (see Section 4.3.1). Nonetheless, the aerodynamics of the platform can still be highly nonlinear, as was evidenced by the underestimation trend at high wind speeds in Section 4.4. A way to solve this is to make a shell using materials with less surface roughness and shaped such that increases aerodynamic performance and minimizes turbulent wake. Also, the characterization of the propeller and calibration of the aerodynamic drag model can be substantially improved using a more controlled environment, like in a wind tunnel. The presented calibration method requires performing vertical profiles of the PBL alongside DWLs where measurements are not truly co-located. Moreover, a vertical profile may not capture a wide enough range of wind speeds to fit a representative curve for the Rayleigh equation (Equation 4.19). In summary, the continuation of these studies can be the evaluation of the presented methods with the addition of wind tunnels and environmental chambers.

As outlined in Chapter 5, it was shown that the CopterSonde was able to withstand a variety of weather conditions during field campaigns where several design enhancements were successfully deployed and tested (see Section 5.2). However, there is still much to be done to deliver a fully autonomous prototype system. For example, flight operations still require human presence in the field to perform flight preparation and monitoring tasks while also complying with regulations. Unattended operations require the development of a suitable autonomous charging station that could replace the manual work of the crew, like battery swapping and visual inspections. The CopterSonde would also need a precision landing system to ensure accurate landings on the charging station [26]. Another critical consideration for the station is system software integration to allow for safe and reliable unattended operations. This would require considerable development and testing of automatic decision-making algorithms capable of assessing surface weather conditions, system self-diagnosing, reporting problems, and distributing data. In addition to these, there are regulatory hurdles to overcome before this kind of concept of operation can be implemented. Altogether, these future developments will remove the human factor and allow for extensive operations without interruptions by human limitations. Additionally, it would significantly help to advance the maturity level of the CopterSonde to become a fully integrated system that can be used routinely.

Finally, if most of the aforementioned suggestions are addressed in the near future, a reliable and robust UAS-based weather-sampling platform may be envisioned as a standalone solution for any desired atmospheric application within the PBL. Moreover, the 3D Mesonet project expands the idea even further by proposing a network of CopterSonde systems distributed over a desired region. The collected observations may be assimilated into NWP models to improve model forecasts with an emphasis on severe and high-impact weather [1, 26, 29].

References

[1] A. R. Segales *et al.*, “The CopterSonde: An insight into the development of a smart unmanned aircraft system for atmospheric boundary layer research,” *Atmospheric Measurement Techniques*, vol. 13, no. 5, pp. 2833–2848, 2020. DOI: 10.5194/amt-13-2833-2020.

[2] A. R. Segales, P. B. Chilson, and J. L. Salazar-Cerreño, “Considerations for improving data quality of thermo-hygrometer sensors on board unmanned aerial systems for planetary boundary layer research,” *Atmospheric Measurement Techniques*, vol. 15, no. 8, pp. 2607–2621, 2022. DOI: 10.5194/amt-15-2607-2022.

[3] H. Shakhatreh *et al.*, “Unmanned aerial vehicles (UAVs): A survey on civil applications and key research challenges,” *IEEE Access*, vol. 7, pp. 48 572–48 634, 2019. DOI: 10.1109/ACCESS.2019.2909530.

[4] J. K. Lazo, M. Lawson, P. H. Larsen, and D. M. Waldman, “U.S. economic sensitivity to weather variability,” *Bulletin of the American Meteorological Society*, vol. 92, no. 6, pp. 709–720, 2011. DOI: 10.1175/2011BAMS2928.1.

[5] I. Goklany, “Deaths and death rates from extreme weather events: 1900-2008,” *Journal of American Physicians and Surgeons*, vol. 14, pp. 102–109, Jan. 2009.

[6] P. J. Webster, “Improve weather forecasts for the developing world,” *Nature*, vol. 493, no. 7430, pp. 17–19, Jan. 2013. DOI: 10.1038/493017a.

[7] C. Liu, “Severe weather in a warming climate,” *Nature*, vol. 544, no. 7651, pp. 422–423, Apr. 2017. DOI: 10.1038/544422a.

[8] D. J. Frame *et al.*, “Climate change attribution and the economic costs of extreme weather events: A study on damages from extreme rainfall and drought,” *Climatic Change*, vol. 162, no. 2, pp. 781–797, Sep. 2020. DOI: 10.1007/s10584-020-02729-y.

[9] B. R. Scheffers and G. Pecl, “Persecuting, protecting or ignoring biodiversity under climate change,” *Nature Climate Change*, vol. 9, no. 8, pp. 581–586, Aug. 2019. DOI: 10.1038/s41558-019-0526-5.

[10] C. Rosenzweig, A. Iglesias, X. B. Yang, P. R. Epstein, and E. Chivian, “Climate change and extreme weather events; implications for food production, plant diseases, and pests,” *Global Change and Human Health*, vol. 2, no. 2, pp. 90–104, Dec. 2001. DOI: 10.1023/A:1015086831467.

[11] P. J. Gregory, J. S. I. Ingram, and M. Brklacich, “Climate change and food security,” *Philosophical Transactions of the Royal Society B: Biological Sciences*, vol. 360, no. 1463, pp. 2139–2148, Nov. 2005. DOI: 10.1098/rstb.2005.1745.

[12] S. A. Markolf, C. Hoehne, A. Fraser, M. V. Chester, and B. S. Underwood, “Transportation resilience to climate change and extreme weather events – beyond risk and robustness,” *Transport Policy*, vol. 74, pp. 174–186, Feb. 2019.

[13] S. Curtis, A. Fair, J. Wistow, D. V. Val, and K. Oven, “Impact of extreme weather events and climate change for health and social care systems,” *Environmental Health*, vol. 16, no. 1, p. 128, Dec. 2017. DOI: 10.1186/s12940-017-0324-3.

[14] M. M. Q. Mirza, “Climate change and extreme weather events: Can developing countries adapt?” *Climate Policy*, vol. 3, no. 3, pp. 233–248, Jan. 2003. DOI: 10.3763/cpol.2003.0330.

[15] B. Geerts *et al.*, “Recommendations for in situ and remote sensing capabilities in atmospheric convection and turbulence,” *Bulletin of the American Meteorological Society*, vol. 99, no. 12, pp. 2463–2470, 2018. DOI: 10.1175/BAMS-D-17-0310.1.

[16] G. de Boer *et al.*, “Advancing unmanned aerial capabilities for atmospheric research,” English, *Bulletin of the American Meteorological Society*, vol. 100, no. 3, ES105–ES108, Mar. 2019. DOI: 10.1175/BAMS-D-18-0254.1.

[17] NWS. “Building a weather-ready nation. 2019-2022 stratigic plan.” (2019), [Online]. Available: https://www.weather.gov/media/wrn/NWS_Weather-Ready-Nation_Strategic_Plan_2019-2022.pdf.

[18] National Severe Storm Laboratory (NSSL). “MRMS: Multiple Radar/Multiple Sensor.” en. (2015), [Online]. Available: https://www.nssl.noaa.gov/news/factsheets/MRMS_2015.March.16.pdf (visited on 11/08/2022).

[19] J. Zhang *et al.*, “Multi-Radar Multi-Sensor (MRMS) quantitative precipitation estimation: Initial operating capabilities,” *Bulletin of the American Meteorolog-*

ical Society, vol. 97, no. 4, pp. 621–638, 2016. DOI: 10.1175/BAMS-D-14-00174.1.

[20] L. Barbieri *et al.*, "Intercomparison of small unmanned aircraft system (sUAS) measurements for atmospheric science during the LAPSE-RATE campaign," *Sensors*, vol. 19, no. 9, 2019. DOI: 10.3390/s19092179.

[21] S. E. Koch *et al.*, "On the use of unmanned aircraft for sampling mesoscale phenomena in the preconvective boundary layer," *J. Atmos. Ocean. Tech.*, vol. 35, pp. 2265–2288, 2018. DOI: 10.1175/JTECH-D-18-0101.1.

[22] S. Kral *et al.*, "Innovative strategies for observations in the arctic atmospheric boundary layer (ISOBAR)—the Hailuoto 2017 campaign," *Atmosphere*, vol. 9, no. 7, p. 268, Jul. 2018. DOI: 10.3390/atmos9070268.

[23] J. D. Jacob, P. B. Chilson, A. L. Houston, and S. W. Smith, "Considerations for atmospheric measurements with small unmanned aircraft systems," *Atmosphere*, vol. 9, no. 7, 2018. DOI: 10.3390/atmos9070252.

[24] N. Wildmann, M. Hofsäß, F. Weimer, A. Joos, and J. Bange, "MASC – a small remotely piloted aircraft (RPA) for wind energy research," *Adv. Sci. Res.*, vol. 11, no. 1, pp. 55–61, 2014. DOI: 10.5194/asr-11-55-2014.

[25] J. Reuder, P. Brisset, M. Jonassen, M. Müller, and S. Mayer, "The small unmanned meteorological observer SUMO: A new tool for atmospheric boundary layer research," *Meteorol. Z.*, vol. 18, no. 2, pp. 141–147, 2009.

[26] P. B. Chilson *et al.*, "Moving towards a network of autonomous UAS atmospheric profiling stations for observations in the Earth's lower atmosphere: The 3D mesonet concept," *Sensors*, vol. 19, no. 12, 2019. DOI: 10.3390/s19122720.

[27] G. de Boer *et al.*, "Development of community, capabilities, and understanding through unmanned aircraft-based atmospheric research: The LAPSE-RATE campaign," *Bulletin of the American Meteorological Society*, vol. 101, no. 5, E684–E699, 2020. DOI: 10.1175/BAMS-D-19-0050.1.

[28] G. M. McFarquhar *et al.*, "Current and future uses of UAS for improved forecasts/warnings and scientific studies," *Bulletin of the American Meteorological Society*, vol. 101, no. 8, E1322–E1328, 2020. DOI: 10.1175/BAMS-D-20-0015.1.

[29] J. O. Pinto *et al.*, "The status and future of small uncrewed aircraft systems (UAS) in operational meteorology," *Bulletin of the American Meteorological Society*, vol. 102, no. 11, E2121–E2136, 2021. DOI: 10.1175/BAMS-D-20-0138.1.

[30] A. A. Jensen *et al.*, "Assimilation of a coordinated fleet of uncrewed aircraft system observations in complex terrain: EnKF system design and preliminary assessment," *Monthly Weather Review*, vol. 149, no. 5, pp. 1459–1480, 2021. DOI: 10.1175/MWR-D-20-0359.1.

[31] WMO. "Plan for a global demonstration project on uncrewed aircraft vehicles (UAVs) use in operational meteorology." (2021), [Online]. Available: https://community.wmo.int/uas-demonstration (visited on 07/17/2022).

[32] FAA. "FAA aerospace forecast: Unmanned aircraft systems." (2019), [Online]. Available: https://www.faa.gov/data_research/aviation/aerospace_forecasts/media/Unmanned_Aircraft_Systems.pdf.

[33] N. A. of Sciences Engineering and Medicine, *The Future of Atmospheric Boundary Layer Observing, Understanding, and Modeling: Proceedings of a Workshop*, L. Everett, Ed. Washington, DC: The National Academies Press, 2018. DOI: 10.17226/25138.

[34] N. A. of Sciences, Engineering and Medicine, *Thriving on Our Changing Planet: A Decadal Strategy for Earth Observation from Space*. Washington, DC: The National Academies Press, 2018. DOI: 10.17226/24938.

[35] N. R. Council, *Observing Weather and Climate from the Ground Up: A Nationwide Network of Networks*. Washington, D.C.: Natl. Acad. Press, 2009. DOI: 10.17226/12540.

[36] NOAA. "Precipitation prediction grand challenge strategic plan." (2020), [Online]. Available: https://www.noaa.gov/sites/default/files/2022-01/PPGC-Strategy_FINAL_2020-1030.pdf.

[37] B. Geerts *et al.*, "Community workshop on developing requirements for in situ and remote sensing capabilities in convective and turbulent environments (C-RITE)," UCAR/NCAR Earth Observing Laboratory, Tech. Rep., 2017.

[38] T. M. Weckwerth and D. B. Parsons, "A review of convection initiation and motivation for IHOP_2002," *Monthly Weather Review*, vol. 134, no. 1, pp. 5–22, 2006. DOI: 10.1175/MWR3067.1.

[39] V. Wulfmeyer *et al.*, “A review of the remote sensing of lower tropospheric thermodynamic profiles and its indispensable role for the understanding and the simulation of water and energy cycles,” *Reviews of Geophysics*, vol. 53, no. 3, pp. 819–895, 2015. DOI: https://doi.org/10.1002/2014RG000476.

[40] R. M. Hardesty and R. M. Hoff, “Thermodynamic profiling technologies workshop report to the national science foundation and the national weather service,” National Center for Atmospheric Research, Tech. Rep. NCAR/TN-488+STR, 2012. DOI: 10.5065/D6SQ8XCF.

[41] W. F. Dabberdt *et al.*, “Multifunctional mesoscale observing networks,” *Bulletin of the American Meteorological Society*, vol. 86, no. 7, pp. 961–982, 2005. DOI: 10.1175/BAMS-86-7-961.

[42] B. R. Greene, A. R. Segales, T. M. Bell, E. A. Pillar-Little, and P. B. Chilson, “Environmental and sensor integration influences on temperature measurements by rotary-wing unmanned aircraft systems,” *Sensors*, vol. 19, no. 6, 2019. DOI: 10.3390/s19061470.

[43] N. Tesla, “Method of and apparatus for controlling mechanism of moving vessels or vehicles,” US613809A, Nov. 1898.

[44] T. G. Konrad, M. L. Hill, J. H. Meyer, and J. R. Rowland, “A small, radio-controlled aircraft as a platform for meteorological sensors,” *Applied Physics Lab Technical Digest*, vol. 10, pp. 11–19, 1970.

[45] H. Farahani, R. Wagiran, and M. N. Hamidon, “Humidity sensors principle, mechanism, and fabrication technologies: A comprehensive review,” *Sensors*, vol. 14, no. 5, pp. 7881–7939, 2014. DOI: 10.3390/s140507881.

[46] G. J. Holland, T. McGeer, and H. Youngren, “Autonomous aerosondes for economical atmospheric soundings anywhere on the globe,” *Bulletin of the American Meteorological Society*, vol. 73, no. 12, pp. 1987–1998, 1992. DOI: 10.1175/1520-0477(1992)073⟨1987:AAFEAS⟩2.0.CO;2.

[47] G. J. Holland *et al.*, “The aerosonde robotic aircraft: A new paradigm for environmental observations,” *Bulletin of the American Meteorological Society*, vol. 82, no. 5, pp. 889–902, 2001. DOI: 10.1175/1520-0477(2001)082⟨0889:TARAAN⟩2.3.CO;2.

[48] M. Shuqing, C. Hongbin, W. Gai, P. Yi, and L. Qiang, “A miniature robotic plane meteorological sounding system,” *Adv. Atmos. Sci.*, vol. 21, no. 6, pp. 890–896, 2004. DOI: 10.1007/BF02915591.

[49] T. Spiess, J. Bange, M. Buschmann, and P. Vörsmann, “First application of the meteorological mini-UAV ’M2AV’,” *Meteorologische Zeitschrift*, vol. 16, pp. 159–169, Apr. 2007. DOI: 10.1127/0941-2948/2007/0195.

[50] C. E. Wainwright, T. A. Bonin, P. B. Chilson, J. A. Gibbs, E. Fedorovich, and R. D. Palmer, “Methods for evaluating the temperature structure-function parameter using unmanned aerial systems and large-eddy simulation,” *Boundary-Layer Meteorology*, vol. 155, no. 2, pp. 189–208, Jan. 2015. DOI: 10.1007/s10546-014-0001-9.

[51] T. A. Bonin, D. Goines, A. Scott, C. Wainwright, P. B. Chilson, and J. Gibbs, “Measuring structure function parameters with a small unmanned aerial system,” *Bound-Lay. Meteorol.*, 2015.

[52] C.-C. Chang, C.-Y. Chang, J.-L. Wang, X.-X. Pan, Y.-C. Chen, and Y.-J. Ho, “An optimized multicopter UAV sounding technique (MUST) for probing comprehensive atmospheric variables,” *Chemosphere*, vol. 254, p. 126 867, 2020. DOI: https://doi.org/10.1016/j.chemosphere.2020.126867.

[53] A. Islam, A. Houston, A. Shankar, and C. Detweiler, “Design and evaluation of sensor housing for boundary layer profiling using multirotors,” *Sensors (Basel)*, vol. 19, no. 11, p. 2481, 2019. DOI: 10.3390/s19112481.

[54] G. de Boer *et al.*, “Measurements from the University of Colorado RAAVEN uncrewed aircraft system during ATOMIC,” *Earth System Science Data*, vol. 14, no. 1, pp. 19–31, 2022. DOI: 10.5194/essd-14-19-2022.

[55] M. Fengler, “How Meteodrones contribute to weather forecasting,” Meteomatics AG, St. Gallen, Switzerland, Tech. Rep., Mar. 2020, p. 13.

[56] S. T. Kral *et al.*, “The innovative strategies for observations in the arctic atmospheric boundary layer project (ISOBAR): Unique finescale observations under stable and very stable conditions,” *Bulletin of the American Meteorological Society*, vol. 102, no. 2, E218–E243, 2021. DOI: 10.1175/BAMS-D-19-0212.1.

[57] E. W. Frew *et al.*, “Field observation of tornadic supercells by multiple autonomous fixed-wing unmanned aircraft,” *Journal of Field Robotics*, vol. 37, no. 6, pp. 1077–1093, 2020. DOI: https://doi.org/10.1002/rob.21947.

[58] A. R. Segales, B. Greene, W. Doyle, J. Martin, and P. Chilson, "An innovative unmanned aircraft system design for optimal temperature, humidity, wind speed, and direction measurements," en, *Poster presentation at the 99th Annual Meeting American Meteorological Society*, Jan. 2019, https://ams.confex.com/ams/2019Annual/webprogram/Paper354013.html (visited on 12/07/2022).

[59] A. R. Segales, B. Greene, W. Doyle, J. Martin, and P. Chilson, "The CopterSonde: An insight into the development of a smart tool for atmospheric boundary layer research," en, *Oral presentation at the International Society for Atmospheric Research using Remotely Piloted Aircraft (ISARRA) meeting*, Jul. 2019, https://www.isarra.org/wp-content/uploads/2019/08/ISARRA_2019_Thur_Segales.pdf (visited on 12/07/2022).

[60] A. R. Segales, B. Greene, T. Bell, W. Doyle, J. Martin, and P. Chilson, "Toward the optimization of atmospheric sampling using unmanned aerial systems: A review of the latest coptersonde design improvements," en, *Poster presentation at the 100th Annual Meeting American Meteorological Society*, Jan. 2020, https://ams.confex.com/ams/2020Annual/meetingapp.cgi/Paper/370305 (visited on 12/07/2022).

[61] P. Chilson *et al.*, "Smartsonde: A small UAS platform to support radar research," in *34th Conf. on Radar Meteorology*, ser. Amer. Meteor. Soc. 12B.6, Williamsburg, VA, Jan. 2009.

[62] Office of the Federal Register, National Archives and Records Administration, *Small unmanned aircraft systems*, 14 CFR 107, US Goverment, Dec. 2016.

[63] "Modeling and simulation of miniature aerial vehicles," in *Aircraft Control and Simulation: Dynamics, Controls Design, and Autonomous Systems*. John Wiley & Sons, Ltd, 2015, ch. 8, pp. 623–663. DOI: https://doi.org/10.1002/9781119174882.ch8.

[64] Quan, Quan, *Introduction to Multicopter Design and Control*, en, 1st ed. Singapore, Singapore: Springer, Jul. 2017.

[65] R. B. Stull, *Meteorology for scientists and engineers: Technical companion book to C. Donald Aherns' "Meteorology today"*, en, 2nd ed. Florence, KY: Brooks/Cole, Jan. 2000.

[66] J. Wallace and P. Hobbs, *Atmospheric Science: An Introductory Survey* (International Geophysics Series). Elsevier Academic Press, 2006, vol. 92.

[67] P. C. Banacos and D. M. Schultz, "The use of moisture flux convergence in forecasting convective initiation: Historical and operational perspectives," *Weather and Forecasting*, vol. 20, no. 3, pp. 351–366, 2005. DOI: 10.1175/WAF858.1.

[68] G. Petty, *A First Course in Atmospheric Thermodynamics*, 1st ed. Wisconsin, USA: Sundog Publishing, 2008.

[69] P. Davidson, *Turbulence An Introduction for Scientists and Engineers*, 2nd ed. New York, USA: Oxford University Press, 2015.

[70] A. N. Kolmogorov, "The local structure of turbulence in incompressible viscous fluid for very large Reynolds numbers," *Proc. R. Soc. Lond. A*, vol. 434, no. 1890, pp. 9–13, 1941.

[71] S. G. Saddoughi and S. V. Veeravalli, “Local isotropy in turbulent boundary layers at high reynolds number,” *Journal of Fluid Mechanics*, vol. 268, pp. 333–372, 1994. DOI: 10.1017/S0022112094001370.

[72] V. I. Tatarskiy, *Wave propagation in locally isotropic turbulent medium with smoothly changing characteristics*, eng, Washington, DC, 1988.

[73] Z. Sorbjan, *Structure of the Atmospheric Boundary Layer*, 2nd ed. New Jersey, USA: Prentice Hall, 2012.

[74] J. A. Gibbs, E. Fedorovich, B. Maronga, C. Wainwright, and M. Dröse, “Comparison of direct and spectral methods for evaluation of the temperature structure parameter in numerically simulated convective boundary layer flows,” *Monthly Weather Review*, vol. 144, no. 6, pp. 2205–2214, 2016. DOI: 10.1175/MWR-D-15-0390.1.

[75] J. C. Kaimal *et al.*, “Turbulence structure in the convective boundary layer,” *Journal of the Atmospheric Sciences*, vol. 33, pp. 2152–2169, Nov. 1976.

[76] W. Kohsiek, “Measuring CT2, CQ2, and CTQ in the unstable surface layer, and relations to the vertical fluxes of heat and moisture,” *Boundary-Layer Meteorology*, vol. 24, pp. 89–107, Sep. 1982. DOI: 10.1007/BF00121802.

[77] J. A. Dantzig, “Improved transient response of thermocouple sensors,” *Review of Scientific Instruments*, vol. 56, no. 5, pp. 723–725, 1985. DOI: 10.1063/1.1138214.

[78] H. Fatoorehchi, M. Alidadi, R. Rach, and A. Shojaeian, "Theoretical and experimental investigation of thermal dynamics of steinhart–hart negative temperature coefficient thermistors," *Journal of Heat Transfer*, vol. 141, no. 7, May 2019, 072003. DOI: 10.1115/1.4043676.

[79] J. S. Steinhart and S. R. Hart, "Calibration curves for thermistors," *Deep Sea Research and Oceanographic Abstracts*, vol. 15, no. 4, pp. 497–503, 1968. DOI: https://doi.org/10.1016/0011-7471(68)90057-0.

[80] InterMet Systems. "iMet-XF UAV sensor." en. (Nov. 2022), [Online]. Available: https://www.intermetsystems.com/products/imet-xf-uav-sensor/ (visited on 11/09/2022).

[81] Innovative Sensor Technology. "Humidity module HYT 271 with pluggable sil contacts." en. (Nov. 2022), [Online]. Available: https://www.ist-ag.com/en/products/humidity-module-hyt-271-pluggable-sil-contacts (visited on 11/09/2022).

[82] AMSYS GmbH & Co. "MS5611 – high resolution barometric sensor 10 – 1200 mbar." en. (2020), [Online]. Available: https://www.amsys-sensor.com/products/pressure-sensor/ms5611-high-resolution-barometric-sensor-10-1200-mbar/ (visited on 11/11/2022).

[83] R. Pletcher, D. Anderson, J. Tannehill, R. Munipalli, and V. Shankar, *Computational Fluid Mechanics and Heat Transfer*, Third, C. Press, Ed. CRC Press, 2013. DOI: https://doi.org/10.1201/9781351124027.

[84] N. Wildmann, F. Kaufmann, and J. Bange, "An inverse-modelling approach for frequency response correction of capacitive humidity sensors in abl research with small remotely piloted aircraft (RPA)," *Atmospheric Measurement Techniques*, vol. 7, no. 9, pp. 3059–3069, 2014. DOI: 10.5194/amt-7-3059-2014.

[85] O. D. Momoh, M. N. Sadiku, and S. M. Musa, "Finite difference analysis of time-dependent spherical problems," in *2013 Proceedings of IEEE Southeastcon*, Apr. 2013, pp. 1–4. DOI: 10.1109/SECON.2013.6567468.

[86] G. J. McRae, "A simple procedure for calculating atmospheric water vapor concentration," *Journal of the Air Pollution Control Association*, vol. 30, no. 4, pp. 394–394, 1980. DOI: 10.1080/00022470.1980.10464362.

[87] A. Moore, "Observation system simulation experiment studies on the use of small UAV for boundary-layer sampling," M.S. thesis, University of Oklahoma, Norman, Oklahoma, 2018.

[88] A. L. Houston and J. M. Keeler, "The impact of sensor response and airspeed on the representation of the convective boundary layer and airmass boundaries by small unmanned aircraft systems," *Journal of Atmospheric and Oceanic Technology*, vol. 35, no. 8, pp. 1687–1699, 2018. DOI: 10.1175/JTECH-D-18-0019.1.

[89] B. R. Greene, A. R. Segales, S. Waugh, S. Duthoit, and P. B. Chilson, "Considerations for temperature sensor placement on rotary-wing unmanned aircraft systems," *Atmos. Meas. Tech.*, vol. 11, no. 10, pp. 5519–5530, 2018. DOI: 10.5194/amt-11-5519-2018.

[90] "Cubepilot: Aerospace company." (Jul. 2022), [Online]. Available: https://www.cubepilot.com/ (visited on 07/10/2022).

[91] "ArduPilot: Trusted, versatile, and open-source autopilot system." (Jul. 2022), [Online]. Available: https://ardupilot.org/ (visited on 07/10/2022).

[92] A. R. Segales *et al.*, *oucass/CASS-ardupilot: BLISSv1.6.6-Copter-4.1.5*, version BLISSv1.6.6-Copter-4.1.5, Mar. 2022. DOI: 10.5281/zenodo.3494656.

[93] "Lynxmotion HQuad500 airframe kit." (Jul. 2022), [Online]. Available: http://www.lynxmotion.com/c-188-mes-hquad500-kits.aspx (visited on 07/10/2022).

[94] "Ecalc: Reliable electric drive simulations." (Aug. 2022), [Online]. Available: https://www.ecalc.ch/ (visited on 08/15/2022).

[95] "APC propeller performance data." (Aug. 2022), [Online]. Available: https://www.apcprop.com/technical-information/performance-data/ (visited on 08/15/2022).

[96] "Thunder Scientific Model 2500 - Humidity Generation and Calibration Equipment." (Oct. 2022), [Online]. Available: https://www.thunderscientific.com/humidity_equipment/model_2500.html (visited on 10/15/2022).

[97] R. A. McPherson *et al.*, "Statewide monitoring of the mesoscale environment: A technical update on the Oklahoma Mesonet," English, *Journal of Atmospheric and Oceanic Technology*, vol. 24, no. 3, pp. 301–321, Mar. 2007. DOI: 10.1175/JTECH1976.1.

[98] “HUMICAP Humidity and Temperature Probe HMP155.” en. (Oct. 2022), [Online]. Available: https://www.vaisala.com/en/products/weather-environmental-sensors/humicap-humidity-temperature-probe-hmp155 (visited on 10/15/2022).

[99] G. Britto Hupsel de Azevedo, B. Doyle, C. A. Fiebrich, and D. Schvartzman, “Low-complexity methods to mitigate the impact of environmental variables on low-cost UAS-based atmospheric carbon dioxide measurements,” *Atmospheric Measurement Techniques*, vol. 15, no. 19, pp. 5599–5618, 2022. DOI: 10.5194/amt-15-5599-2022.

[100] “University of Oklahoma UAS guidelines.” en. (Oct. 2022), [Online]. Available: https://www.ou.edu/content/dam/campussafety/docs/uas-policy.pdf (visited on 10/20/2022).

[101] W. Thielicke, W. Hübert, U. Müller, M. Eggert, and P. Wilhelm, “Towards accurate and practical drone-based wind measurements with an ultrasonic anemometer,” *Atmospheric Measurement Techniques*, vol. 14, no. 2, pp. 1303–1318, 2021. DOI: 10.5194/amt-14-1303-2021.

[102] Y. Li, Z. Zhang, X. Hao, and W. Yin, “A measurement system for time constant of thermocouple sensor based on high temperature furnace,” *Applied Sciences*, vol. 8, no. 12, 2018. DOI: 10.3390/app8122585.

[103] S. M. Waugh, “The “U-Tube”: An improved aspirated temperature system for mobile meteorological observations, especially in severe weather,” English, *Journal of Atmospheric and Oceanic Technology*, vol. 38, no. 9, pp. 1477–1489, Sep. 2021. DOI: 10.1175/JTECH-D-21-0008.1.

[104] S. Das and P. Suganthan, “Differential evolution: A survey of the state-of-the-art.,” *IEEE Trans. Evolutionary Computation*, vol. 15, pp. 4–31, Jan. 2011.

[105] P. Tsilingiris, “Thermophysical and transport properties of humid air at temperature range between 0 and 100°C,” *Energy Conversion and Management*, vol. 49, no. 5, pp. 1098–1110, 2008. DOI: https://doi.org/10.1016/j.enconman.2007.09.015.

[106] A. V. Oppenheim and R. W. Schafer, “Transform analysis of linear time-invariant systems,” in *Discrete-Time Signal Processing*, 3rd ed. USA: Prentice Hall Press, 2009, ch. 5, pp. 311–318.

[107] B. L. Stevens, F. L. Lewis, and E. N. Johnson, “The kinematics and dynamics of aircraft motion,” in *Aircraft Control and Simulation: Dynamics, Controls Design, and Autonomous Systems*. John Wiley & Sons, Ltd, 2015, ch. 1, pp. 1–62. DOI: https://doi.org/10.1002/9781119174882.ch1.

[108] P. P. Neumann and M. Bartholmai, “Real-time wind estimation on a micro unmanned aerial vehicle using its inertial measurement unit,” *Sensor Actuat. A-Phys.*, vol. 235, pp. 300–310, 2015. DOI: 10.1016/j.sna.2015.09.036.

[109] B. R. Greene, “Boundary layer profiling using rotary-wing unmanned aircraft systems: Filling the atmospheric data gap,” M.S. thesis, The University of Oklahoma, 2018.

[110] T. M. Bell, B. R. Greene, P. M. Klein, M. Carney, and P. B. Chilson, “Confronting the boundary layer data gap: Evaluating new and existing methodolo-

gies of probing the lower atmosphere," *Atmospheric Measurement Techniques*, vol. 13, no. 7, pp. 3855–3872, 2020. DOI: 10.5194/amt-13-3855-2020.

[111] J. González-Rocha, S. F. J. De Wekker, S. D. Ross, and C. A. Woolsey, "Wind profiling in the lower atmosphere from wind-induced perturbations to multirotor UAS," *Sensors*, vol. 20, no. 5, 2020. DOI: 10.3390/s20051341.

[112] J. Gonzalez-Rocha, C. A. Woolsey, C. Sultan, and S. F. De Wekker, "Model-based wind profiling in the lower atmosphere with multirotor UAS," in (AIAA SciTech Forum), AIAA SciTech Forum. American Institute of Aeronautics and Astronautics, Jan. 2019, 0. DOI: 10.2514/6.2019-1598.

[113] J.-Y. Wang, B. Luo, M. Zeng, and Q.-H. Meng, "A wind estimation method with an unmanned rotorcraft for environmental monitoring tasks," *Sensors*, vol. 18, no. 12, 2018. DOI: 10.3390/s18124504.

[114] T. Wetz, N. Wildmann, and F. Beyrich, "Distributed wind measurements with multiple quadrotor unmanned aerial vehicles in the atmospheric boundary layer," *Atmospheric Measurement Techniques*, vol. 14, no. 5, pp. 3795–3814, 2021. DOI: 10.5194/amt-14-3795-2021.

[115] N. Wildmann and T. Wetz, "Towards vertical wind and turbulent flux estimation with multicopter UAS," *EGUsphere*, vol. 2022, pp. 1–20, 2022. DOI: 10.5194/egusphere-2022-110.

[116] J. Han, "From PID to active disturbance rejection control," *IEEE Transactions on Industrial Electronics*, vol. 56, no. 3, pp. 900–906, 2009. DOI: 10.1109/TIE.2008.2011621.

[117] G. Herbst, "A simulative study on active disturbance rejection control (ADRC) as a control tool for practitioners," *Electronics*, vol. 2, no. 3, pp. 246–279, 2013. DOI: 10.3390/electronics2030246.

[118] R. Gill and R. D'Andrea, "Propeller thrust and drag in forward flight," in *2017 IEEE Conference on Control Technology and Applications (CCTA)*, 2017, pp. 73–79. DOI: 10.1109/CCTA.2017.8062443.

[119] R. Gill and R. D'Andrea, "Computationally efficient force and moment models for propellers in UAV forward flight applications," *Drones*, vol. 3, no. 4, 2019. DOI: 10.3390/drones3040077.

[120] B. L. Stevens, F. L. Lewis, and E. N. Johnson, "Robustness and multivariable frequency-domain techniques," in *Aircraft Control and Simulation: Dynamics, Controls Design, and Autonomous Systems*. John Wiley & Sons, Ltd, 2015, ch. 6, pp. 500–583. DOI: https://doi.org/10.1002/9781119174882.ch6.

[121] S. Li, J. Yang, W.-H. Chen, and X. Chen, "Generalized extended state observer based control for systems with mismatched uncertainties," *IEEE Transactions on Industrial Electronics*, vol. 59, no. 12, pp. 4792–4802, 2012.

[122] Z. Gao, "Scaling and bandwidth-parameterization based controller tuning," in *Proceedings of the 2003 American Control Conference, 2003.*, vol. 6, 2003, pp. 4989–4996. DOI: 10.1109/ACC.2003.1242516.

[123] T. Wetz and N. Wildmann, "Spatially distributed and simultaneous wind measurements with a fleet of small quadrotor UAS," *Journal of Physics: Confer-*

ence Series, vol. 2265, no. 2, p. 022 086, May 2022. DOI: 10.1088/1742-6596/2265/2/022086.

[124] J. M. Straka, E. N. Rasmussen, and S. E. Fredrickson, "A mobile mesonet for finescale meteorological observations," English, *Journal of Atmospheric and Oceanic Technology*, vol. 13, no. 5, pp. 921–936, Oct. 1996. DOI: 10.1175/1520-0426(1996)013⟨0921:AMMFFM⟩2.0.CO;2.

[125] G. Pearson, F. Davies, and C. Collier, "An analysis of the performance of the UFAM pulsed doppler lidar for observing the boundary layer," English, *Journal of Atmospheric and Oceanic Technology*, vol. 26, no. 2, pp. 240–250, Feb. 2009. DOI: 10.1175/2008JTECHA1128.1.

[126] T. J. Wagner, P. M. Klein, and D. D. Turner, "A new generation of ground-based mobile platforms for active and passive profiling of the boundary layer," English, *Bulletin of the American Meteorological Society*, vol. 100, no. 1, pp. 137–153, Jan. 2019. DOI: 10.1175/BAMS-D-17-0165.1.

[127] "Vaisala radiosonde RS41-SGP datasheet." (Sep. 2022), [Online]. Available: https://www.vaisala.com/sites/default/files/documents/WEA-MET-RS41SGP-Datasheet-B211444EN.pdf (visited on 09/29/2022).

[128] J. Steinheuer, C. Detring, F. Beyrich, U. Löhnert, P. Friederichs, and S. Fiedler, "A new scanning scheme and flexible retrieval for mean winds and gusts from Doppler lidar measurements," *Atmospheric Measurement Techniques*, vol. 15, no. 10, pp. 3243–3260, 2022. DOI: 10.5194/amt-15-3243-2022.

[129] DroneLogbook. "Drone Operations Compliance & Fleet Management Made Easy." en. (Oct. 2022), [Online]. Available: https://www.dronelogbook.com (visited on 10/24/2022).

[130] S. van der Walt, S. C. Colbert, and G. Varoquaux, "The NumPy array: A structure for efficient numerical computation," *Comput. Sci. Eng.*, vol. 13, no. 2, pp. 22–30, Mar. 2011. DOI: 10.1109/MCSE.2011.37.

[131] J. D. Hunter, "Matplotlib: A 2D graphics environment," *Comput. Sci. Eng.*, vol. 9, no. 3, pp. 90–95, 2007. DOI: 10.1109/MCSE.2007.55.

[132] R. M. May *et al.*, *Metpy: A Python package for meteorological data*, version 0.11.1, Boulder, Colorado: Unidata, 2019. DOI: 10.5065/D6WW7G29.

[133] P. Virtanen *et al.*, "SciPy 1.0–Fundamental Algorithms for Scientific Computing in Python," *arXiv e-prints*, arXiv:1907.10121, arXiv:1907.10121, Jul. 2019.

[134] P. Wessel, W. H. F. Smith, R. Scharroo, J. Luis, and F. Wobbe, "Generic mapping tools: Improved version released," *EOS T. Am. Geophys. Un.*, vol. 94, no. 45, pp. 409–410, 2013. DOI: 10.1002/2013EO450001.

[135] "ISOBAR – 2018 field campaign." en. (Feb. 2018), [Online]. Available: https://isobar2018campaign.w.uib.no/ (visited on 10/25/2022).

[136] B. R. Greene *et al.*, *University of Oklahoma CopterSonde Files from LAPSE-RATE*, version v1, Zenodo, Apr. 2020. DOI: 10.5281/zenodo.3737087.

[137] G. de Boer, D. Lawrence, and A. Doddi, *Datahawk2 files from LAPSE-RATE*, version 2.0, Funding supported by the US National Science Foundation (AGS

1807199) and the US Department of Energy (DE-SC0018985)., Zenodo, Mar. 2020. DOI: 10.5281/zenodo.3891620.

[138] S. C. C. Bailey *et al.*, "University of Kentucky measurements of wind, temperature, pressure and humidity in support of LAPSE-RATE using multisite fixed-wing and rotorcraft unmanned aerial systems," *Earth System Science Data*, vol. 12, no. 3, pp. 1759–1773, 2020. DOI: 10.5194/essd-12-1759-2020.

[139] E. A. Pillar-Little *et al.*, "Observations of the thermodynamic and kinematic state of the atmospheric boundary layer over the San Luis Valley, CO, using the Coptersonde 2 remotely piloted aircraft system in support of the LAPSE-RATE field campaign," *Earth System Science Data*, vol. 13, no. 2, pp. 269–280, 2021. DOI: 10.5194/essd-13-269-2021.

[140] P. B. Chilson, K. Williams, T. M. Bell, B. R. Greene, and D. Tripp. "Anticipating the impact of wind on UAS-based atmospheric profiling in the lower atmosphere." en. (Jan. 2020), [Online]. Available: https://ams.confex.com/ams/2020Annual/meetingapp.cgi/Paper/367374 (visited on 10/28/2022).

[141] NOAA National Severe Storm Laboratory. "PERiLS: Propagation, evolution, and rotation in linear storms." en. (2021), [Online]. Available: https://www.nssl.noaa.gov/projects/perils/ (visited on 10/30/2022).

[142] NOAA-OMAO. "Unmanned aircraft systems (UAS) operations." en. (Dec. 2019), [Online]. Available: https://www.omao.noaa.gov/find/media/documents/policy-220-1-5-unmanned-aircraft-systems-uas-operations (visited on 10/30/2022).

[143] NOAA-OMAO. “Uncrewed aircraft systems handbook.” en. (Jun. 2022), [Online]. Available: https://www.omao.noaa.gov/find/media/documents/noaa-uncrewed-aircraft-systems-handbook-june-2022 (visited on 10/30/2022).

[144] NOAA. “NAO 216-105B: Policy on research and development transitions.” en. (Feb. 2019), [Online]. Available: https://www.noaa.gov/organization/administration/nao-216-105b-policy-on-research-and-development-transitions (visited on 10/30/2022).

[145] Atmospheric Radiation Measurement (ARM) User Facility. “Tracking aerosol convection interactions experiment (TRACER).” en. (2021), [Online]. Available: https://www.arm.gov/research/campaigns/amf2021tracer (visited on 10/31/2022).

[146] Z. Barbeau, J. Feight, K. G., and J. Jacob. “V0098: Quadrotor flow field visualization.” en. (2015), [Online]. Available: https://gfm.aps.org/meetings/dfd-2015/55f8c4a7b8ac311c710000aa (visited on 12/07/2022).

Appendix A

Acronyms

CASS Center for Autonomous Sensing and Sampling

ARRC Advanced Radar Research Center

OU The University of Oklahoma

KAEFS Kessler Atmospheric and Ecological Field Station

NOAA National Oceanic and Atmospheric Administration

NWS National Weather Service

NSSL National Severe Storms Laboratory

OAMO Office of Marine and Aviation Operations

FAA Federal Aviation Administration

COA Certificate of Authorization

PBL Planetary Boundary Layer

CBL Convective Boundary Layer

FTI Frontal and Thermal Inversions

KTS Kolmogorov Turbulence Spectra

ISR Inertial Subrange

NWP Numerical Weather Predictions

UAS Unmanned Aerial System

UAV Unmanned Aerial Vehicle

WxUAS Weather Unmanned Aerial System

WxUAV Weather Unmanned Aerial Vehicle

GNSS Global Navigation Satellite System

ESC Electronic Speed Controller

PIC Pilot in Command

GSO Ground Station Operator

VO Visual Observer

GCS Ground Control Station

AGL Above Ground Level

AMSL Above Mean Sea Level

IDMP Inverse Dynamical Model Processing

ADRC Active Disturbance Rejection Control

LESO Linear Extended State Observer

WVFM Wind Vane Flight Mode

SITL Software in the Loop

CLAMPS Collaborative Lower Atmospheric Mobile Profiling System

DWL Doppler Wind Lidar

DLFP Doppler Lidar Fixed Point

AVAD Advance Velocity Azimuth Display

Appendix B

UAS Regulations

B.1 Part 107 rules

The FAA established federal rules regarding UAVs weighing less than 55 lbs which are proposed in chapter 14 of the Code of Federal Regulation (14 CFR Part 107) [62]. This covers a broad spectrum of commercial and government uses, including those from institutions involved in research and academia. The following is an excerpt from the summary of the Part 107 rules for UAS with additional details related to UAS operations for scientific research in accordance with the guidelines of the University of Oklahoma.

B.1.1 Exclusions

- Model aircraft that satisfy all of the criteria specified by 49 U.S.C. § 44809.
- Public and government aircraft.
- Aircraft operating under 49 U.S.C. § 44807.
- Air carrier operations. This includes package delivery using UAS.

B.1.2 Operational Limitations

- The UAV must weigh less than 25 kg (55 lbs).
- The UAS must remain close enough to the remote pilot in command (RPIC) and the person manipulating the flight controls of the UAV at all times. This must be done by people capable of seeing the UAV with vision unaided by any device other than prescribed corrective lenses.
- The UAS may not operate over any persons that are not directly participating in the operation.
- Night operations may be conducted with appropriate anti-collision lighting.
- Must yield right of way to other aircraft.
- May use a visual observer (VO) or spotter but not required.
- First person view (FPV) type UAS cannot satisfy “see-and-avoid” requirement and, therefore, a VO is required to be present.
- Maximum groundspeed of 44.7 m s^{-1} (87 knots).
- Maximum altitude of 121.9 m (400 ft) above ground level (AGL) or structure.
- Minimum weather visibility of 4828 m (3 miles) from the ground control station.
- Operations in Class B, C, D, and E airspace are allowed with required Air Traffic Control (ATC) permission.
- Operations in Class G airspace are allowed without ATC permission.
- No person may act as RPIC or VO for more than one UAS operation at one time.

- No operations from a moving aircraft.
- No operations from a moving vehicle unless the operation is over sparsely populated area.
- No careless of reckless operations.
- No carriage of hazardous materials.
- Requires pre-flight inspection by the RPIC.
- A person may not operate a UAS if they know or have reason to know of any physical or mental condition that would interfere with the safe operation of UAS.
- Foreign-registered UAS are allowed to operate under Part 107 if they satisfy the requirements of Part 375.
- External load operations are allowed if the object being carried by the UAS is securely attached without affecting the performance of the UAS.
- Transportation of property for compensation or hire allowed provided that:
    - The aircraft, including payload, weigh less than 25 kg (55 lbs) total.
    - The flight is conducted within visual line of sight and not from a moving vehicle or aircraft.
    - The flight occurs wholly within the bounds of the United States and does not involve transport between (1) Hawaii and other place in Hawaii through airspace outside of Hawaii; (2) the District of Columbia and another place in the District of Columbia; or (3) a territory or possession of the United States and another place in the same territory or possession.

- Most of the restrictions listed above are waivable if the applicant demonstrates that their operation can safely be conducted under the terms of a certificate of waiver.

B.1.3 RPIC Certification and Responsibilities

- Establishes a RPIC position.
- The person operating the UAS must either hold a remote pilot airman certificate (Part 107 license) or be under direct supervision of a person who does hold it.
- To qualify for a remote pilot certificate, a person must:
  - Demonstrate aeronautical knowledge by either:
    - Passing an initial aeronautical knowledge test at an FAA-approved testing center.
    - Hold a part 61 pilot certificate other than student pilot, complete a flight review within the previous 24 months, and complete a UAS online training course provided by the FAA.
  - Be vetted by the Transportation of Security Administration.
  - Be at least 16 years old.
- Part 61 pilot certificate holders may obtain a temporary remote pilot certificate immediately upon submission of their application for a permanent certificate.
- Until international standards are developed, foreign-certificated UAS pilots will be required to obtain an FAA-issued remote pilot certificate with a UAS rating.

Other required tasks of the RPIC while on duty are:

- Make available to the FAA, upon request, the UAS for inspection or testing, and any associated documents/records required to be kept under the rule.
- Report to the FAA within 10 days of any operation that results in at least serious injury, loss of consciousness, or property damage of at least $500.
- Conduct a preflight inspection, including specific aircraft and control station systems checks, to ensure the UAS is in a condition for safe operation.
- Ensure that the small unmanned aircraft complies with the existing registration requirements specified in § 91.203(a)(2).
- A remote pilot in command may deviate from the requirements of this rule in response to an in-flight emergency.

B.1.4 Part 107 Aircraft Requirements

The FAA airworthiness certification for the UAS is not required. However, the remote pilot in command must conduct a pre-flight check of the UAS to ensure that it is in a condition for safe operation.

B.2 Certificate of Authorization

For any of the operations listed below, a drone operator cannot fly purely under the FAA's Part 107 operating rules but would need to be authorized via a waiver, known as Certificate of Authorization (COA). The Air Traffic Organization may issue a COA to a public operator for a certain UAS operation. Following the submission of a full application, the FAA performs a thorough operational and technical evaluation. Provisions or constraints may be imposed as part of the approval if required to ensure the UAS can operate safely alongside other airspace users. In most situations, the FAA will send an official response within 60 days of receiving a completed application.

- Flying with reduced visibility.
- Flying within 152.4 m (500 ft) of the base of the clouds.
- Beyond visual line of sight.
- Fly a UAS heavier than 25 kg (55 lbs).
- A RPIC flying more than 1 UAS at a time.
- Fly higher than 121.9 m (400ft).
- Fly with ground speeds over 44.7 m s^{-1} (87 knots).
- Operations form moving vehicles in non-sparsely populated areas.

B.3 OU Guidelines for UAS Operations

In addition to the above rules, the University of Oklahoma's Risk Management department has its own well-established guidelines for UAS operations, managed by a UAS Review Committee [100]. The purpose of the UAS Review Committee is to review applications for proposed UAS operations that further the University's mission and, if appropriate, approve the proposed operation. The UAS Review committee is also tasked with establishing and periodically reviewing UAS operations guidelines designed to reduce safety risks to people and property on campus. Any UAS flights that will be operated for research purposes must apply through the Office of the Vice President for Research. For brevity, only those non-overlapping rules relevant to this work are listed below.

B.3.1 Guidelines for Air Safety

- All UAS operations must comply with current federal and state laws regarding UAS, including FAA regulations.
- UAS operating under the University's authority must meet University's operating requirements for aircraft maintenance and pre-flight and post-flight inspections.
- University's Norman Campus is located almost entirely within 5 miles of Max Westheimer Airport. The RPIC must obtain approval through the Low Altitude Authorization and Notification Capability (LAANC) system.

B.3.2 Guidelines for Safety to People and Property

- Applicants must submit evidence of the RPIC's proficiency with the make/model of the UAS proposed to be used. For this, the RPIC must have logged evidence of a minimum of 5 hours of flight time using the said make/model of UAS, and have logged at least 3 takeoffs and landings.
- UAS operations are prohibited on home football game days and special event days.
- UAS operations should be scheduled, when possible, at times when the risk of nonparticipating persons coming within range of the UAS is minimized.

B.3.3 Student Flight Applications

- FAA allows the use of UAS for educational purposes to be operated under the rules for recreational flyers.

- A student must have a Part-107 Pilot's license for validating proficiency purposes for the University.
- A student must have liability insurance. Who pays for the insurance does not matter as long as the coverage is for the student pilot.

B.3.4 Insurance and Reporting Requirements

UAS operated by third-party vendors must provide a certificate of insurance identifying the University of Oklahoma as a certificate holder and evidencing sufficient liability insurance limits as determined by Enterprise Risk Management department.

UAS operators must comply with FAA reporting requirements for reporting incidents resulting in injury to a person or damage to property. In addition, UAS operators must immediately report any incident resulting in injury to a person or damage to property to OU Enterprise Risk Management. As always, in an emergency, UAS operators should contact 911 for immediate assistance.

Appendix C

NOAA Airworthiness Certification

The following document is an official airworthiness release for the CopterSonde-3D UAS issued by NOAA-OMAO in November 2021.

UNITED STATES DEPARTMENT OF COMMERCE
National Oceanic and Atmospheric Administration
OFFICE OF MARINE AND AVIATION OPERATIONS
Uncrewed Systems Operations Center-UAS Division
3450 Flightline Drive
Lakeland, Florida 33811

29 November 2021

MEMORANDUM FOR: The Record

FROM: Commander Paul S. Hemmick, NOAA
Chief, Uncrewed Aircraft Systems Division (UASD)

SUBJECT: Airworthiness Release (AWR) of Coptersonde Uncrewed Aircraft System (AWR NOAACoptersonde2021R0)

Airworthiness Statement

This document constitutes an Airworthiness Release (AWR) for the Coptersonde Uncrewed Aircraft System (UAS) as described in the Technical Manual. The UASD finds the Coptersonde UAS to be airworthy In Accordance With (IAW) the UASD application of MIL-HDBK-516C. This aircraft is capable of operating in compliance with applicable requirements in 14 CFR Part 91 when operated IAW this document. The Coptersonde UAS is categorized as a developmental aircraft (USN Category 3, see NAVAIRINST 13034.1D) for which compliance to accepted engineering data cannot be determined. This release is valid as of November 2021 and will remain valid unless there are changes in configuration of the subject equipment.

Operating Conditions

Per MIL-HDBK-516C (Airworthiness Certification Criteria), Par. 1.2 Applicability, the Coptersonde UAS is considered expendable. This aircraft shall be operated under the conditions specified in this document, AOC UAS Policy 220-1-5, Original Equipment Manufacturer (OEM) instructions, Coptersonde Operating Procedures, FAA Certificate of Authorization (COA) if applicable, the appropriate Project Instructions, and the applicable Operational Risk Management (ORM) document. NOAA accepts that the UAS may be lost during operations and has determined that the associated risks are acceptable. The Pilot in Command (PIC) shall ensure that the following items are addressed prior to any operations and are followed during each operation. They shall be addressed in writing and may be contained in any of the above referenced documents. These requirements can only be waived by the Chief, UASD.

- Operations limited to ensure UAS maintains proper separation from crewed aircraft.
- Operations limited to a specific weather envelope for which the UAS have been tested.
- Ground Test prior to each flight.
- Routine maintenance checks before and after each flight.
- Replacement and charging of batteries as needed.

- Review of flight data from Ground Control Station after each flight as necessary to ensure safe operation for subsequent flights.
- PIC to maintain safe flight or terminate flight if unable.

Additional Restrictions and Warnings

The following restrictions and warnings are mandatory unless adequately mitigated or accounted for in the above referenced documentation and approved in writing by the Chief, UAS Division.

WARNING

The air vehicle is susceptible to radiated emissions. Loss of link, loss of GPS, loss of video, and possible loss of vehicle control are likely in proximity to emitters. Operators shall avoid known high intensity Electromagnetic Interference (EMI) areas.

WARNING

The Coptersonde UAS has not completed full airworthiness qualification. All flight operations shall be conducted in a manner to minimize exposure to crewed aircraft, watercraft, personnel, vehicles, populated ground areas, and other obstructions or hazards.

WARNING

The Coptersonde UAS does not have a sense and avoid system. Mid-air collision is a risk. All flight operations shall be conducted to ensure that crewed and uncrewed aircraft shall maintain proper separation.

WARNING

Accidental operation of the Coptersonde UAS outside of approved airspace shall be immediately reported to Air Traffic Control (ATC)/Range Control as applicable. The operator shall make immediate actions to correct the flight path and/or follow ATC / Range Control direction(s).

WARNING

The Coptersonde UAS has not undergone Safety of Flight (SOF) Explosive Atmosphere testing. A serious fire or explosion may result if the aircraft is powered while flammable vapors are present during ground or flight operations. Do not operate the system in the presence of flammable vapors. At a minimum, system operations must be at least 50 feet from flammable vapor sources.

NOTE

1. The aircraft operating instructions, procedures, and limitations shall be in accordance with the Technical Procedures referenced above and this AWR. In the event of conflict between these documents, the information in this AWR shall prevail.
2. Emergency procedures: IAW the operator's manual.
3. The Home waypoint shall be over an approved auto land point.
4. Flight over populated areas shall be avoided.
5. Launch of the Coptersonde UAS shall be directed away from ground personnel.

6. Ground personnel shall avoid being near the flight path of the UAS during launch and recovery.
7. The Coptersonde UAS has not completed the full airworthiness qualification process. This AWR has been granted through a Category 3A Airworthiness evaluation (developmental). A Category 3A AWR establishes a minimum level of safety for UAS operations. Strict adherence to the Operator's Manual, local Standard Operating Procedures for UAS, and this AWR is required to reduce the risk of loss of the aircraft, property damage and personal injury.
8. Coordination of channel selection with other systems operating in the area is critical to reducing accident rates.
9. The Coptersonde UAS software components have not undergone software safety verification testing. Software errors resulting in system anomalies may result in loss of the aircraft. The PIC shall ensure that the flight software is updated to the current OEM release(s).
10. The Coptersonde shipboard operations have not been verified by the UASD. Shipboard operations are to be approved on a case-by-case basis until verified by UASD personnel. Future changes to Coptersonde shipboard operations status will be reflected within the specific Operational Risk Management plan and/or changes to airworthiness documentation.